Alma Mater Studiorum · University of Bologna

School of Science
Department of Physics and Astronomy
Master Degree in Physics

Charge accumulation and transport in degenerately doped semiconducting polymers with mixed ionic and electronic conductivity

Supervisor:
Prof. Tobias Cramer

Co-supervisor:
Dr. Francesco Decataldo

Submitted by:
Filippo Bonafè

Academic Year 2019/2020

Abstract

This thesis is part of the fields of Material Physics and Organic Electronics and aims to determine the charge carrier density and mobility in the hydrated conducting polymer–polyelectrolyte blend PEDOT:PSS. This kind of material combines electronic semiconductor functionality with selective ionic transport, biocompatibility and electrochemical stability in water. This advantageous material properties combination makes PEDOT:PSS a unique material to build organic electrochemical transistors (OECTs), which have relevant application as amplifying transducers for bioelectronic and biochemical signals.

In order to measure charge carrier density and mobility, an innovative 4-wire, contact-independent characterization technique was introduced, the electrolyte-gated van der Pauw (EgVDP) method, which was combined with electrochemical impedance spectroscopy (EIS). The technique was applied to macroscopic thin film samples and micro-structured PEDOT:PSS thin film devices fabricated using photolithography. The EgVDP method revealed to be effective for the measurements of holes' mobility in hydrated PEDOT:PSS thin films, which resulted to be $\langle\mu_p\rangle = (0.67\pm0.02)\ cm^2V^{-1}s^{-1}$. By comparing this result with 2-point-probe measurements, we found that contact resistance effects led to a mobility overestimation in the latter. Ion accumulation at the drain contact creates a gate-dependent potential barrier and is discussed as a probable reason for the overestimation in 2-point-probe measurements.

The measured charge transport properties of PEDOT:PSS were analyzed in the framework of an extended drift-diffusion model. The extended model fits well also to the non-linear response in the transport characterization and results suggest a Gaussian DOS for PEDOT:PSS in the carrier density range of experiments (10^{18} -10^{20} cm^{-3}). The PEDOT:PSS-electrolyte interface capacitance resulted to be voltage-independent, confirming the hypothesis of its morphological origin, related to the separation between the electronic (PEDOT) and ionic (PSS) phases in the blend.

Index

CHAPTER 1: INTRODUCTION

1.1 Introduction

Heavily doped conjugated polymers (CPs), often in the form of conjugated polymer–polyelectrolyte blends, combine and couple electronic semiconductor functionality with selective ionic transport [1]. Among this class of materials, poly(3,4-ethylenedioxythiophene) doped with polystyrene sulfonate (PEDOT:PSS) is the most widely employed because of its optical transparency at visible range, tunable electrical conductivity, chemical stability and simple processing properties [2]. PEDOT:PSS is a conducting polymer composited by the semiconducting polymer PEDOT and the polyelectrolyte (PE) PSS. PSS acts as a dopant, compensating positive holes on the PEDOT by fixed anionic acceptors (SO^{3-}) on the PSS. After synthesis and processing into thin films, the PEDOT:PSS phase separates into PEDOT-rich regions of tens of nanometers in size, containing many 1- to 2-nm large crystallites, and a surrounding PSS-rich phase [3].

Recently, there has been a significant interest in using and exploring CP-PE blends in aqueous applications for organic biosensors and bioelectronics. These applications use electrolytes or operate under elevated hygroscopic conditions, which render the counterions mobile and thus make the coupling of the electronic and ionic transport crucial [4]. In particular, organic electrochemical transistors (OECTs) make effective use of ion injection to modulate the bulk conductivity of an organic semiconductor channel. PEDOT:PSS-based OECTs show multiple advantages, such as high transconductance, mixed ionic-electronic conductivity and high biocompatibility when compared to other electrolyte gated transistor structures. [5] Optimization of OECTs and their translation into high-performance bioelectronic devices requires the study and understanding of the fundamental properties.

This Thesis is part of the field of Organic Bioelectronics and Material Physics, and aims to study charge accumulation and transport processes in PEDOT:PSS.

The charge carrier mobility is a key performance criteria for organic semiconductors. High-mobility values allow fast device operation as needed in many applications. Mobility is conveniently extracted from thin film transistor (TFT) characterization. However, the presence of contact effects complicates the interpretation of TFT characteristic curves, and can lead to serious mobility overestimations [6]. For this reason, a 4-wire contact-independent characterization technique is introduced in this work, the electrolyte-gated van der Pauw (EgVDP) method, which was combined with electrochemical impedance spectroscopy (EIS) to measure charge carrier density and mobility in PEDOT:PSS. Specifically designed micro-structured PEDOT:PSS thin film devices were fabricated with photolithography for the experimental characterization.

Measurement results were analyzed to investigate the origin of the volumetric capacitance of CP-PE blends and the fundamental transport properties of PEDOT:PSS, such as its density of states. EgVDP measurements were compared with 2 point-probe characterizations of a miniaturized OECT, to examinate the influence of the contact resistance on mobility extraction. Finally, experimental data were furtherly interpreted with an extended drift diffusion model, to understand the device physics and charge transport in PEDOT:PSS.

This work is divided into four chapters.

The first chapter introduces the main themes of this research. The first part presents the main properties of PEDOT:PSS, which make it an emerging material for many relevant bioelectronic applications. The second part deals with the theoretical modelling of charge transport in CP-PE blends. An extended drift-diffusion model (Tybrandt's model) is presented and applied in different PEDOT:PSS-based applications. The third part is about measuring the

holes' mobility in thin films of organic semiconductor. A contact-independent measurement technique is presented, the Rolin's gated van der Pauw's (gVDP) method [6]. Starting from this point, an innovative technique is developed, the electrolyte-gated van der Pauw (EgVDP) method, which combines the advantages of gVDP characterization with the coupled electronic-ionic conductivity of CP-PE blends.

The second chapter deals with the methods adopted in this research. The first part presents the design and the microfabrication process of micro-structured PEDOT:PSS thin film devices for EgVDP measurements. The second part discusses the characterization methods of the fabricated devices. The experimental setup and the measurement procedures and parameters are reported in detail.

The third chapter presents the main result obtained in this work. The first part introduces the fabricated PEDOT:PSS thin film devices. The second part is focused on the interaction between PEDOT and the oxygen dissolved in the electrolyte. In the third part, electrochemical impedance spectroscopies are analyzed to study charge accumulation in PEDOT:PSS. Then, the transport properties of organic electrochemical transistors are studied from the characterization of two-contacts devices. Finally, EgVDP measurements are examined both for millimeter-sized and miniaturized samples and a first analysis is applied to extract relevant material properties, such as the charge carrier mobility.

The fourth chapter discusses the results of this research and compare them with literature. In the first part, EgVDP and two-contacts measurements are compared to investigate the possible role of the contacts resistance during mobility extraction. The second part is focused on the analysis of charge accumulation in PEDOT:PSS. Measurement results from EIS are interpreted to investigate the origin of the large capacitance of hydrated PEDOT:PSS thin films. Finally, charge transport properties of PEDOT:PSS are examined: the PEDOT:PSS density of state is investigated, and EgVDP measurements are analyzed by applying Tybrandt's model.

1.2 PEDOT:PSS – an emerging material for Bioelectronics

Electrically conductive polymers are of great interest in the field of bioelectronics as materials that can improve the interface between electronics and biology. Among different conducting polymers, poly(3,4-ethylenedioxythiophene):poly(styrene sulfonate) (PEDOT:PSS) is the most promising due to its high conductivity, easy processing and commercial availability [7]. PEDOT:PSS is commercialized in the form of an aqueous dispersion which can be processed in the form of thin films by spin-coating and solvent-casting methods. PEDOT:PSS is widely used in the field of organic electronics as transparent conductive oxides (TCO), and as a hole-conducting layer or electrochromic layer in a variety of devices from organic light-emitting diodes (OLEDs) and organic photovoltaic devices (OPVs) to electrochromics. In recent years, PEDOT:PSS has also been widely applied in bioelectronic devices for applications as electrodes for electrophysiology, a variety of biosensors, organic electrochemical transistors (OECTs) and small bioelectrode coatings.
This section briefly illustrates the general advantages arising from the applications of organic conducting and semiconducting materials in the field of bioelectronics, where they show features unmatched by standard inorganic semiconductors. Then, starting from this general framework, the main properties of PEDOT:PSS will be discussed in detail.

1.2.1 Organic materials for Bioelectronics

The field of bioelectronics dates back to the work of Luigi Galvani in the 18th century. In the now famous experiment, he made the detached legs of a frog twitch by applying a small voltage. Today there are a variety of bioelectronic devices available that offer improved healthcare, offer environmental protection, and accelerate the pace of scientific progress. These include biosensors such as glucose monitors for diabetics, pacemakers/defibrillators, cochlear implants for restoration of lost or damaged physiological functions, and biomedical instruments that provide a deeper understanding of the how cells communicate with each other and with their environment. [8]
Bioelectronics is limited by the materials that transduce signals across the biotic/abiotic interface. The electronic devices surrounding us in our daily lives rely almost exclusively on electrons as the dominant charge carrier. In stark contrast, signals in biological systems, such as those regulating the physiology and defense mechanisms in animals, are typically represented by various molecular entities ranging in size from small cations and neurotransmitters to giant-sized macromolecules such as DNA and proteins [9]. Inside an organism, biological signals can be transported within the blood stream (the vasculature) and along neurons, where they pass from one neuron to the other via signaling across the synaptic cleft. In addition, signals may be transmitted between large clusters of cells that are tightly linked to each other. In this case, signals are transmitted via protein complexes forming so called gap junctions. [10] Proteins are common signal substances within the vasculature, where they induce a systemic response. This often involves large populations of different cells throughout the organism, such as the activation of the immune response to various infections. Ions, on the other hand, are common in neuronal signaling, and the strictly regulated perturbation of the ion homeostasis drives the signal along neurons to highly specific targets. Other signals known to affect the shape and function of cells can originate from the extracellular environment. [11] The interactions between cells and biological or artificial surfaces are mediated by endogenous protein complexes, such as cell adhesion molecules (e.g., integrins), intermediary filaments (e.g., F-actin bundles), and multi-adhesive matrix proteins (e.g., fibronectin). These signals, combined with intercellular signaling within the organ, and signals from other tissues, will affect the overall structure and morphology of a tissue, as the positioning of the cells contains much information about the structure and morphology of the

tissue. [12] Collectively, the examples provided here illustrate the complexity of signaling in biological systems, which utilize a variety of different signaling entities that are communicated inside and between cells and organs via a variety of pathways.

Motivated by a further understanding of biology, diagnostics, and therapy, various tools have been developed to map and selectively record and trigger some of these pathways. With tools such as molecular probes, recording electrodes, or inorganic-based semiconductor devices, one can translate the status and concentration of a biomolecule into optical or electronic singles, and vice versa. Thus, this enables us to translate information across the biology–technology gap. One of the greatest challenges with present "translation" technology is that it is typically neither compatible nor stable when interfaced with biological systems. Further, present inorganic semiconductor technology often also falls short to a great extent regarding biochemical selectivity and sensitivity.

In recent decades, conducting and semiconducting organic polymers have emerged as excellent tools for translating signals between these two realms, due to the unique combination of both electronic and ionic/molecular conductivity. [13] Organic electronic and optoelectronic materials can be synthesized to include various receptors or anchoring sites, as well as to express desired chemical characteristics, all of which can facilitate highly selective transduction. These materials can also be produced with geometries, morphologies, and mechanical properties that provide minimal invasiveness and biostability over long periods of time.

When considering new applications for a class of materials, a beneficial exercise is to analyze their identifying characteristics and to find how they match the requirements of these applications. In the case of organic bioelectronics, a comparison between organics and silicon, the champion material of electronics, is also instructive. **Figure 1.2.1** shows schematics of silicon and of a conjugated polymer film, such as poly(3,4-ethylenedioxythiophene) (PEDOT), in contact with an electrolyte solution. [14] Both materials are shown to be doped p-type, silicon with boron and PEDOT with poly(styrene sulfonate) (PSS). A solvated ion is shown in the electrolyte to define a relative scale. Silicon is held together by a network of covalent bonds, where each atom shares valence electrons with four neighbors. In contrast, the organic material consists of (macro-)molecular blocks within which atoms are covalently bonded to each other. However, these blocks are held together by means of weak van der Waals interactions and, in the case of doped materials, electrostatic interactions as well. The prevalence of van der Waals interactions in the "soft" organic material defines the key difference with the "hard" silicon. Stemming from this bonding arrangement are the identifying characteristics of organics: [7]

- **Oxide-free interfaces and ionic transport:**

The cleavage of a silicon crystal and its exposure to the atmosphere gives rise to the growth of an oxide layer (see **Figure 1.2.1**). In contrast, the surface of the organic contains no broken covalent bonds and is oxide-free. Therefore, organic materials allow exchange of ions between the biological solutions and the bulk of the electronic material. This means that the whole volume of the film, not just its surface, is involved in the interaction with the biological environment, a feature which can be exploited to yield powerful biosensors and bioactuators.

- **Facile processing and modification:**

Low temperature processing and facile chemical modification are the "classical" characteristics of organics, much exploited in organic light emitting diodes and solar cells to endow features such as low-cost fabrication through roll-to-roll processing techniques, as well as and tunable optical absorption/emission spectra. These properties are also applicable in bioelectronics. Low-temperature processing allows the fabrication of devices with novel form factors, such as transistors integrated on woven fibers. [15] Moreover, it allows to maintain the functionality of

biological moieties during device fabrication. This paves the way for a new paradigm in biosensor design, where the biological layer is not necessarily the last one to be deposited but can be placed at a particular location inside a device to maximize transduction. The ability to chemically modify the active materials also allows tuning of biodegradability, which can be engineered by inserting the appropriate units along the backbone of a conjugated polymer. [16]

- **Excitations couple strongly to the structure of the molecules:**

In organics, excitations couple strongly to the structure of the molecule, and by extension, of the film. In silicon, the presence of electronic charge does not modify the lattice appreciably, as atoms are bonded with each other in a 3D manner. In contrast, removing an electron from a thiophene chain causes part of the chain to revert from an aromatic to a quinoid structure (the one of PEDOT in **Figure 1.2.1**). When doping is performed in an electrolyte solution, the corresponding uptake/release of ions can cause large dimensional changes in the organic film. As a result, electrical doping not only affects the electrical properties of the film but has a dramatic influence across the board. Changes in optical and mechanical properties upon doping, have been used to great advantage for making electrochromic displays [17] and actuators for artificial muscles, [18] respectively.

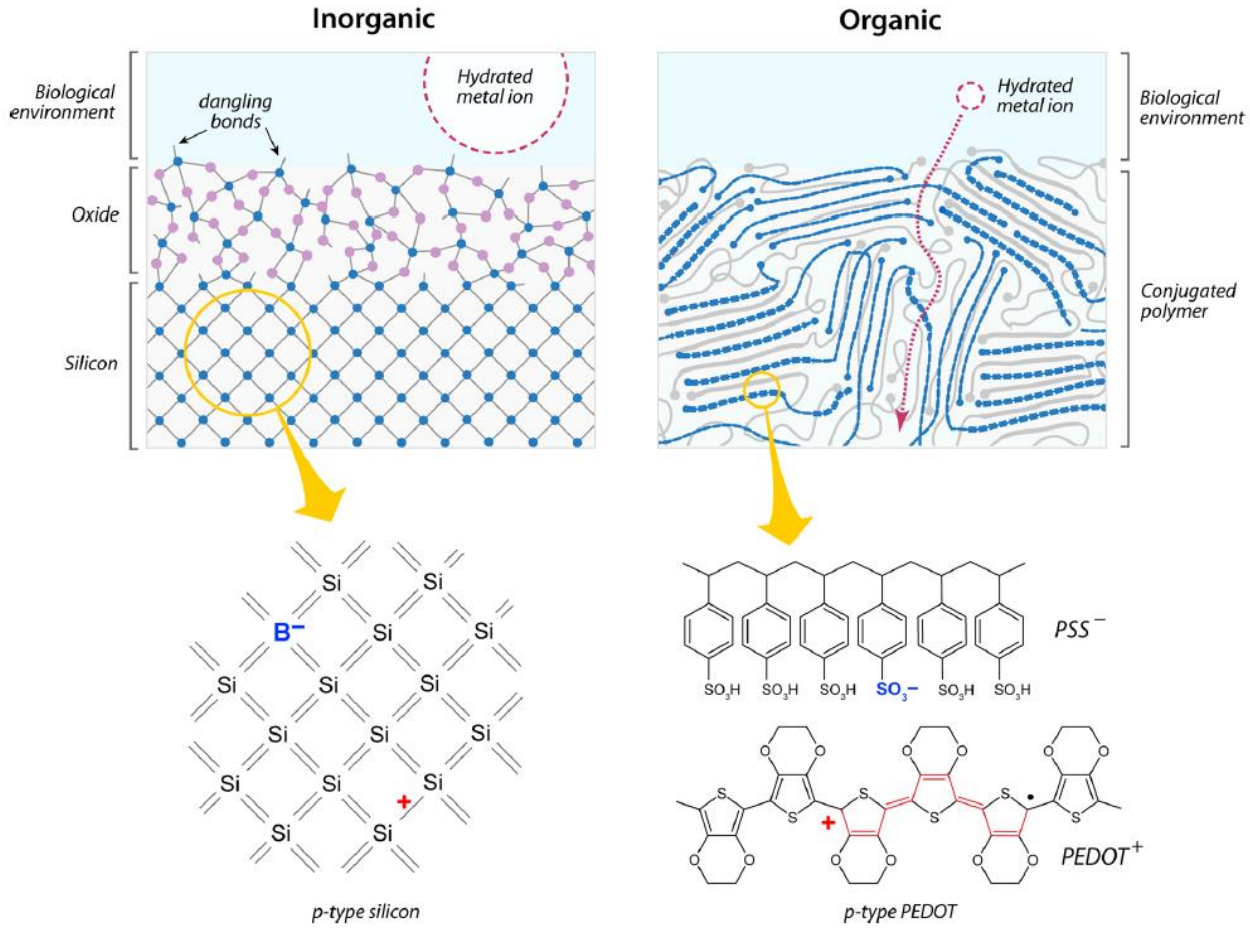

Figure 1.2.1: Schematics of an inorganic semiconductor, silicon, and an organic semiconductor, PEDOT, at the interface with an electrolyte. The hydrated ion is meant to be the same in both schematics, defining the relative scale. The insets show the action of p-type dopants, boron in silicon, and PSS in PEDOT, respectively. [7]

1.2.2 Organic conducting and semiconducting polymers

IUPAC defines a polymer as "a molecule with relatively high molecular mass, whose structure is essentially given by a multiple repetition of units that derive from relatively low molecular mass compounds ". [19] The repetitive units that constitute the polymers are called monomers and bind to each other through covalent bonds, until they form the polymeric "backbone". The organic term implies the presence of a chain mainly composed of carbon atoms, while conductivity is a characteristic that appears only in conjugated polymers, and not in saturated polymers, which are insulators. In the latter, such as polyethylene, all valence electrons participate in σ-type covalent bonds, and consequently the energy gap between the valence band and the conduction band is very wide. In the former, such as polyalanine, some orbitals (typically the p_z orbitals of the carbon atoms) are not involved in the formation of σ bonds, and thus can form π bonding systems along the polymer chain, which originate electronic delocalization and therefore conductivity. A classic example for studying electrical conductivity in conjugated polymers is polyacetylene (PAc, with molecular formula [-CH] n), the simplest conjugated polymer, shown in **Figure 1.2.2.**

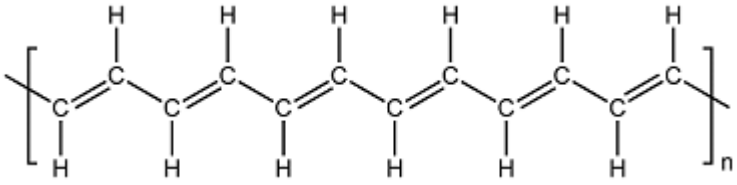

Figure 1.2.2: Polyacetylene

PAc molecule can be modeled with a linear chain, constituted by N atoms separated by distance d. The total length of the chain will be (N-1)·d, which can be approximated with N·d if N tends to infinite. In PAc, every single carbon atom (with four valence electrons) has a σ-type bond with two neighboring carbon atoms and one hydrogen atom, with one π electron per atom remaining. If we assume π electrons completely delocalized, we can apply the quantum-mechanical model for a free particle in a one-dimensional box (with zero potential inside the box, which corresponds to the polymeric backbone, and infinite outside). The wave functions correspond to a set of eigenvalues: [20]

$$E_n = \frac{n^2 h^2}{8m(Nd)^2} \qquad 1.2.1$$

where *h* is the Planck's constant, *m* the electron mass and *n* a quantum number (*n* = 1,2,3...). If every orbital is occupied by two electrons with opposite spin, the energies of the highest occupied molecular orbital (HOMO) and of the lowest unoccupied molecular orbital (LUMO) are:

$$E_{HOMO} = \frac{\left(\frac{N}{2}\right)^2 h^2}{8m(Nd)^2} \; ; \; E_{LUMO} = \frac{\left(\frac{N}{2}+1\right)^2 h^2}{8m(Nd)^2} \qquad 1.2.2$$

and the energy required to excite an electron from HOMO to LUMO is

$$\Delta E = E_{LUMO} - E_{HOMO} = \frac{(N+1)^2 h^2}{8m(Nd)^2} \approx \frac{h^2}{8mNd^2} \qquad 1.2.3$$

which tends to zero if N tends to infinite.
According to this model, macroscopic conjugated polymers should behave as conductors, but experimentally their bandgap does not decrease as in **Eq 1.2.3**. The discrepancy between theory and experiments was resolved in the 1930s by the Peierls' theorem, who claims that a one-dimensional and equally spaced chain is unstable. [21] This instability is solved through a chain distortion which reduces the system symmetry and consequently rearranges the levels of the orbitals. In the case of polyacetylene, the distortion of the lattice leads to a repeated unit with two carbon atoms closer together and two other carbon atoms more distant. Therefore, the repeated unit can be written as [–CH = CH–] instead of [–CH–]. For a chain with alternately long or short bonds, the electrons are not completely delocalized and the band energetic structure changes: an energy gap is formed between a completely full band π and a completely empty band π *. The energy difference between HOMO in the band π and LUMO in that π * is the energy gap (E_g). This alternating bond structure is common to all conjugated polymers.

1.2.3 Doping of semiconducting polymers

Since there are no partially full bands, pure conjugated polymers are typically semiconductors, with low conductivity (for example, polyacetylene has an intrinsic conductivity $<10^{-5}$ S cm^{-1}). As the energy gap depends on the molecular structure of the repeated unit, it is possible to control it during the synthesis phase through molecular level design. Beside this possibility, other methods are available to increase the conductivity of the conjugated polymer in a successive phase (but always before deposition), which are called doping methods and essentially represent a charge transfer reaction which involves the partial oxidation or reduction of the polymer.
The term doping can be deceptive within this context: in inorganic semiconductor physics, doping is used to describe the introduction of an external neutral atom (of a different element) in a host lattice to change its electronic structure, while for conductive polymers the process typically consists in a redox reaction. The insulating neutral polymer is converted into an ionic complex, consisting of a polymeric cation (p-type doping) and a counterion which is the reduced form of the oxidizing agent, or conversely, into a polymeric anion (n-type doping) and a counterion which is the oxidized form of the reducing agent. Consequently, doping in conjugated polymers is reversible in nature. Through doping the optical and electrical properties of conductive polymers can be controlled, in the range from insulators to conductors: for example, electrical conductivity can be increased up to 10-12 orders of magnitude, reaching 1000 S / cm. [22]
Different processes can lead to a reduction or oxidation of the polymer and therefore vary its oxidation state:

1) Chemical doping: this process allows p/n doping through the introduction of an anion/cation inside the polymer. Chemical doping is generally hardly controllable, because high-doping levels are achievable only on extremely pure materials and low-doping levels are generally unstable.

2) Electrochemical doping: this process was invented to overcome the problems of chemical doping. An electrode supplies to the polymer the charge for the redox reaction, while a flow of ions, coming from the surrounding electrolyte, diffuses inside (or outside) polymer to compensate the electronic charge (and maintain the neutrality of the polymer itself). The doping level is determined by the voltage applied between the conductive polymer and the counter electrode. Therefore, any doping level can be achieved by providing a fixed potential to the electrolytic cell and waiting for the achievement of the electrochemical equilibrium (which involves no current flowing in the cell).

3) Acid-base reaction doping: an acid-base reaction can initiate a redox process inside the polymer that leads to the variation of the spin of the electrons, without however varying number. This process leads to a metallic-like state, in which a positive charge is available in each repeating unit, associated with the relative counterion necessary for the redox reaction.

4) Photo-doping: photo-absorption in some materials leads to the generation of electron-hole pairs. In this process the generated charges act as free carriers that oxidize and reduce the polymer in which they have been produced.

5) Charge injection (interfacial doping): electrons and ions are injected into the polymer through a metallic contact, obtaining an oxidized or a reduced state. Unlike the chemical or electrochemical doping, no counterions are involved, and the charge injection is irreversible.

An overview on the doping processes in organic semiconductor and on their possible applications is reported in **Figure 1.2.3**

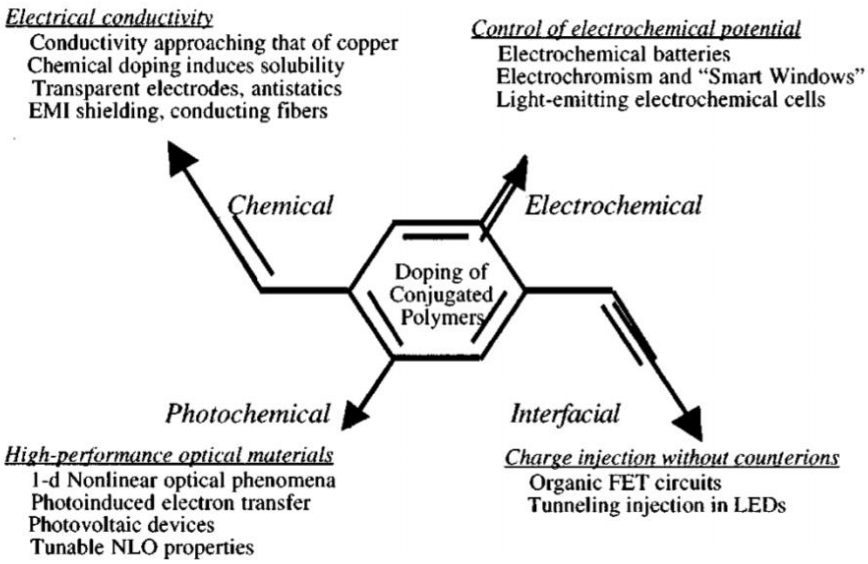

Figure 1.2.3: Doping processes and relative applications in organic semiconductors

1.2.4 PEDOT

After the discovery of electrically conducting polymers in 1977 by Professors Heeger, MacDiarmid, and Shirakawa (Nobel Prize in Chemistry 2000), and more than 30 years of worldwide intense research and huge efforts, PEDOT, or poly(3,4-ethylenedioxythiophene), sets various standards for the entire field. PEDOT, which was invented in 1988 by Bayer AG, Leverkusen, is probably the best conducting polymer available in terms of conductivity, processability, and stability. Furthermore, PEDOT is the only conducting polymer that is commercially produced on a large-scale (nowadays mainly by H.C. Starck Clevios GmbH, Leverkusen) and sold for many applications**.** [22]
PEDOT is an intrinsically conductive, insoluble polymer composed of a chain of monomers of 3,4-ethylenedioxythiophene (EDOT) (see **Figure 1.2.4**), which shows in particular high

conductivity and good stability in its doped state. The need to obtain a polymer with these characteristics arose from the fact that polythiophene, while showing good stability compared to other conductive polymers, had limited applications in the industrial field due to the decrease of its conductivity over a long period. The stability of polythiophene may be improved by decreasing its oxidizing potential. This can be realized by introducing an alkoxyl group (such as ether group), which has electron-donating character. Substituted thiophene can be polymerized at a considerably lower potential than thiophene and the resulting polymers are more stable in the anion-doped state especially when the side chain is not too long. Ether substituted thiophene mainly includes 3-alkoxy thiophenes, 3,4-alkoxy thiophenes and 3,4-(crown ether)thiophene. However, study of polythiophenes with long side chain substituents shows that the polymer chain is distorted thereby giving lower conductivities. Therefore, a shorter chain ether substitutented thiophene, 3,4-ethylenedioxythiophene, has attracted many scientists' attention and many results about PEDOT have been achieved and reported. [2]

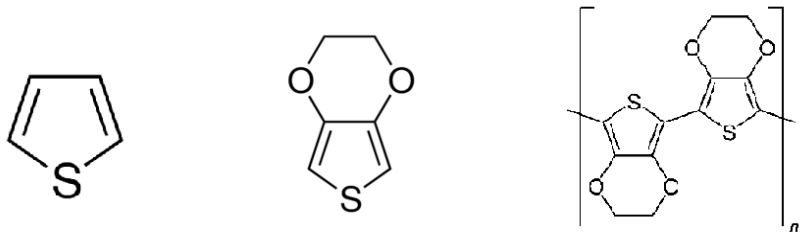

Figure 1.2.4: Thiophene, EDOT and PEDOT

Some of the main features of PEDOT are resumed in the following list: [14]

1) Reversible doping state:

PEDOT can be repeatedly doped and undoped. PEDOT is almost transparent and light blue in the oxidized state and can be easily changed into opaque and dark blue appearance in the neutral state. Thus, its color changes visibly when its doped state changes and may be suitable for optical applications, such as electrochromic displays. [3]

2) Excellent stability:

PEDOT has improved chemical and thermal stability. Thermal studies show that a continuous degradation occurs above 150 °C and complete decomposition above 390 °C. Electrical conducting properties appear to remain almost unaltered after aging in environmental conditions. Its high stability is attributed to favorable ring geometry and the electron-donating effect of the oxygen atoms at the 3,4-positions stabilizing the positive charge in the polymer backbone. [22]

3) Regular structure:

PEDOT has a very regular structure, due to the reduced length of the chains of the alkoxyl group (which, as seen above, are instead longer in the thiophene). Therefore, this polymer is expected to have fewer defects than similar thiophene-based polymers.

4) Low band-gap (High conductivity):

PEDOT has a low band gap of 1.5-1.6 eV. Experimental results show that after doping, PEDOT exhibits reduced absorption in the visible: the oscillator strength shifts from around 1.5 eV (lowest π-π* transition) to below 1 eV in the metallic state. [23] Thus, it shows a high electrical conductivity (up to 550 S/cm) in the doped state.

1.2.5: PEDOT:PSS dispersions

One of the reasons why poly(3,4-ethylenedioxythiophene) (PEDOT) has become a successful conductive polymer is the availability as a polymer dispersion. In combination with poly(styrenesulfonic acid) (PSS) as a counterion, a polyelectrolyte complex (PEC) can be prepared that forms a stable dispersion, which is producible on an industrial scale and can be used in many deposition techniques. [22] The chemical structure of PEDOT:PSS is reported in **Figure 1.2.5.**

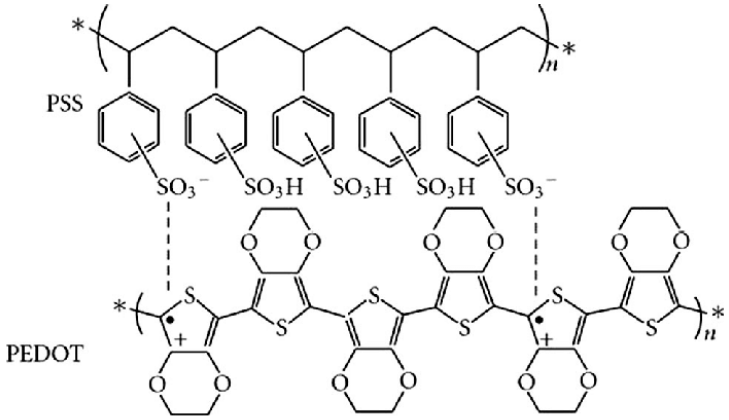

Figure 1.2.5: PEDOT:PSS

Polyelectrolyte complexes are typically formed by mixing aqueous solutions of polyanions and polycations. Poly(styrenesulfonic acid) (PSS) was the first polyelectrolyte used for a PEC with PEDOT in 1990 and has remained the industrial standard ever since. [7] PSS is commercially available in a large range of molecular weights with different polydispersities. Further to its commercial availability and its solubility in water, PSS forms durable films and shows no absorption in the visible range of light, resulting in transparent films.
On a molecular level, two arrangements of PECs have been discussed in literature. [24] The ladder type (**Figure 1.2.6**) shows a pairing of most of the polar groups from one macromolecule with those of the opposite charge of another macromolecule. The ladder type is found particularly in dilute solutions and in cases where the spacing of the charged groups along the chain is similar for both polyelectrolytes. Furthermore, the ladder type is found when polyelectrolytes with very different molecular weights are used. The so-called scrambled egg type is based on random interactions between polar groups of one macromolecule and various other polar groups of many other polymer chains with no order on the molecular or supermolecular level. Due to the delocalization of positive charges in PEDOT, the resulting weak polar groups and the different spacing of charges in PEDOT compared to PSS, it is reasonable to a assume that the

structure of PEDOT:PSS shows the form of a scrambled egg type. A pairing of charges as required in the ladder type is not possible.

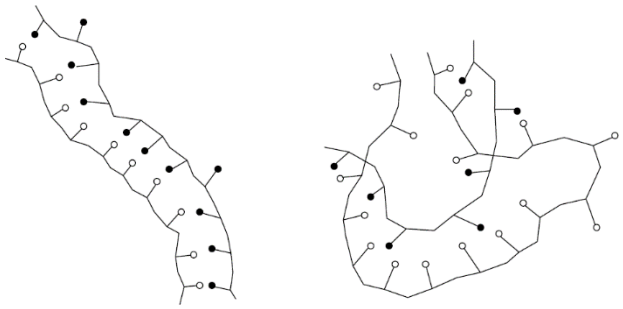

Figure 1.2.6: PEC arrangements: (left) ladder-type and (right) scrambled egg type.

Aqueous PEDOT:PSS dispersions are commercially available from H.C. Starck Clevios GmbH under the trade name Clevios ™. As reference **Figure 1.2.7** summarizes important properties of established Clevios dispersions.

Trade Name	Solids Content in Water (w/w) (%)	PEDOT:PSS Ratio (w/w)	Viscosity at 20°C (mPas)	Particle Size d_{50} (nm)	Conductivity (S/cm)
Clevios P	1.3	1:2.5	80	80	<10
Clevios PH	1.3	1:2.5	20	30	<10
Clevios P VP AI 4083	1.5	1:6	10	40	10^{-3}
Clevios P VP CH 8000	2.8	1:20	15	25	10^{-5}
Clevios PH 500	1.1	1:2.5	25	30	500
Clevios PH 750	1.1	1:2.5	25	30	750
Clevios PH 1000	1.1	1:2.5	30	30	1000

Figure 1.2.6: Commercial PEDOT:PSS Dispersions in water and their properties.

1.2.6: Deposition and properties of PEDOT:PSS thin films

PEDOT:PSS dispersed in water can be deposited in principle by all common techniques employed for the deposition of waterborne coatings. Common deposition techniques to obtain uniform coatings are slit coating, drop casting, bar coating, spin coating, electrospinning, and spraying. In case a structured deposition is required, other techniques are commonly employed such as screen printing, inkjet, nozzle printing, and various forms of contact printing (that is, relief, flexo, gravure, and offset printing). Other ways for structured deposition of PEDOT:PSS have been realized by modifying the wetting properties of the surface, that is by depositing water repellants or by introducing photo-lithographical techniques. [25]

The deposition of PEDOT:PSS dispersions by spin coating has proven to be an easily accessible technique to obtain uniform films in a thickness range of 0 to 300 nm. The typical spin coating operation involves the application of the dispersion to a substrate followed by acceleration of the substrate to a chosen rotational speed. Alternatively, the liquid solution may be applied while the substrate is spinning. The angular velocity of the substrate with the overlying solution

results in the ejection of most of the applied liquid where only a thin film is left on the substrate. The thickness, morphology, and surface topography of the final film obtained from a particular material in a given solvent at a given concentration is highly reproducible. In general, these three properties are known to depend highly on rotational speed, viscosity, volatility, diffusivity, molecular weight, and concentration of the solutes. Typical spin curves for two commercial grades of PEDOT:PSS (CLEVIOS P AI 4083, designed for hole injection in OLEDs and CLEVIOS PH 500, designed for transparent electrodes) are illustrated in **Figure 1.2.8.** The root-mean-square roughness of these films are in the order of 1 nm, making them attractive as cladding layer for thin film device applications.

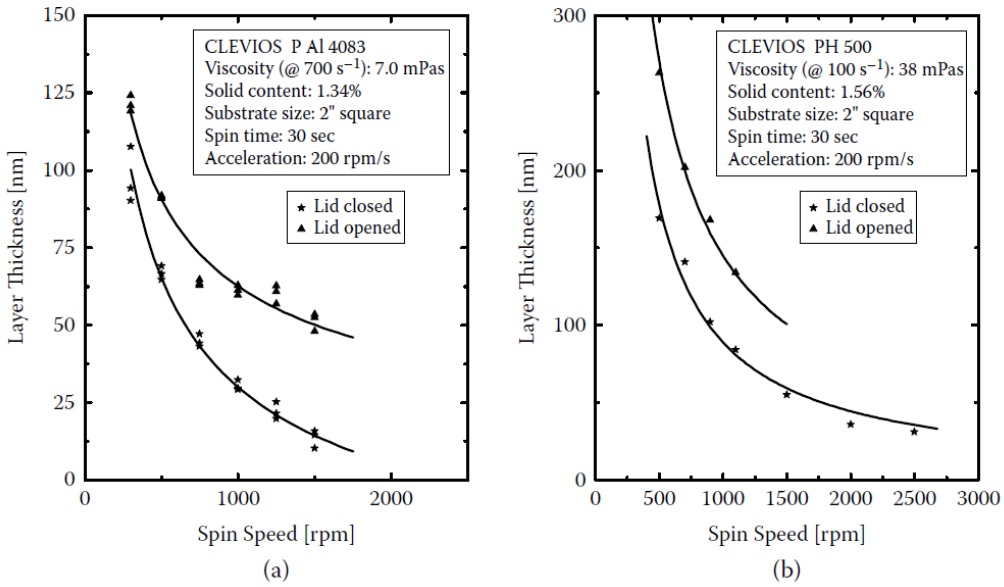

Figure 1.2.8: Spin curves of CLEVIOS P AI 4083 and CLEVIOS PH 500 taken on a Carl Suss RC8 spin coater, equipped with a rotating lid. Spin curves were obtained with the lid in opened and closed mode. The insets disclose parameter settings. [16]

PEDOT:PSS films have to be dried prior to further processing. The water is removed by baking the layers at elevated temperatures, under infrared (IR) radiation, or by applying a vacuum. These different drying processes are often also combined, for example, in a vacuum oven. Thin films are typically dry after leaving the coated substrates on a hot plate set to temperatures above 100° C for some seconds.
The main properties of PEDOT:PSS thin films are briefly resumed in the following list.

- **Thermal and UV stability:**

One major advantage of PEDOT:PSS films is their thermal stability. The thermal stability has been studied by thermo-gravimetrical analysis (TGA) of thick layers. **Figure 1.2.9 a** depicts the weight loss over time while the sample is heated at a constant rate in helium. Between 100°C and 200°C the weight loss is solely determined by evaporation of remaining water. Like other polymers containing sulfonic acid groups, PEDOT:PSS is strongly hygroscopic and will take up moisture when handled under ambient conditions. At about 250°C the sample weight decreases significantly. This is attributed to SO_2 ions and indicates the fragmentation of the PSS sulfonate group. At higher temperatures of T > 350°C other fragments due to carbon oxidation are detected. Following the analytical data obtained by TGA the material is considered to be thermally stable up to temperatures of T = 200°C.

In contrast to many other conjugated highly conductive polymers, PEDOT:PSS exhibits a very stable conductivity. However, like all carbon compounds, PEDOT-type polymers will be subject to degradation, especially when exposed to harsher conditions. The overall decay mechanism seems to be oxidation by oxygen enhanced by UV light. Attack to the sulfur atom of the thiophene ring will yield nonconducting sulfoxide and sulfone structures. To maintain the conductivity of PEDOT:PSS films over time, an ultraviolet (UV)-light exposure as well as elevated temperatures above 70° C in combination with the exposure to oxygen need to be avoided. One way to protect layers in devices is the hermetic encapsulation of the device, as shown in **Figure 1.2.9 b**.

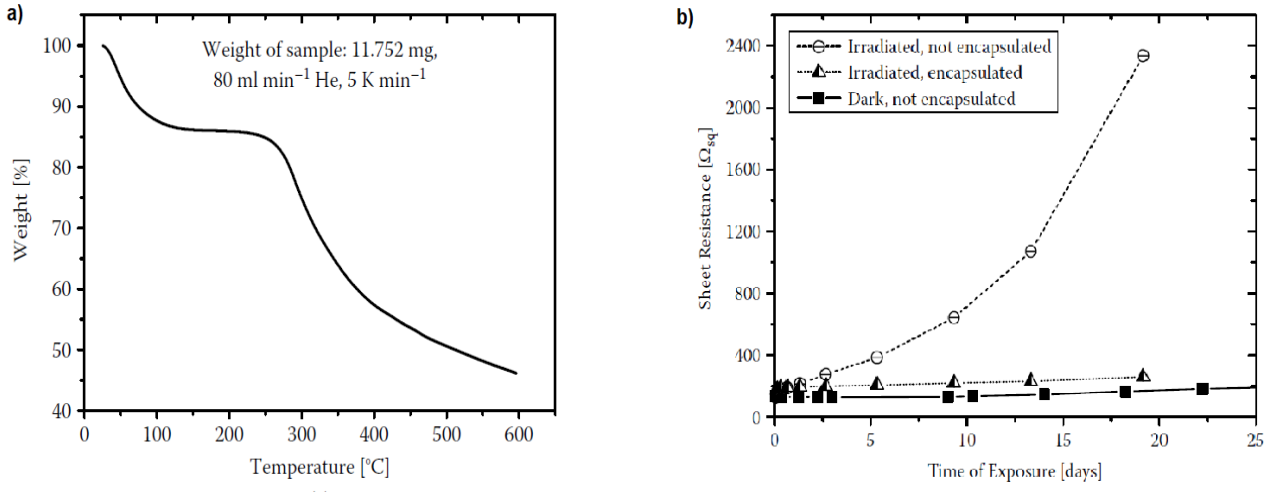

Figure 1.2.9: a) Thermogravimetric analysis (TGA) of PEDOT:PSS with a ratio of PEDOT to PSS as 1:20 by weight. The weight loss is monitored while heating the sample at a constant rate of 5 K/min. **b)** Sheet resistance of pristine PEDOT PSS-films (Clevios PH 500) were monitored over time while the samples were exposed to the radiation of a Xe lamp. When the films are encapsulated against ambient air by a glued-on glass cap the increase of resistivity is slowed down and resembles the change of a control sample being stored in the dark . [16]

- **Mechanical properties:**

For transparent conductive coatings on polymer foils, the flexibility of PEDOT:PSS films is considered to be a major advantage compared to inorganic materials like metal oxide films: in fact, PEDOT:PSS films do not crack upon bending. The mechanical properties of PEDOT:PSS have been investigated by tensile strength tests on free-standing PEDOT:PSS films. Young's modulus and tensile strength were found to be strongly depending on the relative humidity (rH) level during the tests. The polymer exhibits brittle fracture behavior at rH = 23% which changes to plastic fracture behavior at an intermediate rH = 55%. The Young's modulus of films increases from 0.9 GPa at 55% rH to 2.8 GPa at 23% rH. The ability to change film dimensions by altering the water content in the films has driven Okuzaki et al. to employ PEDOT:PSS as an electro-active polymer actuator. [26] Film contractions of 2.4% to 4.5 % depending on relative humidity were realized by applying an electrical bias and removing water from the films due to Joule heating.

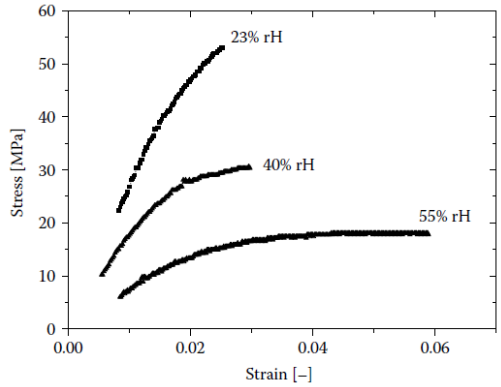

Figure 1.2.10: Stress-strain diagrams of PEDOT:PSS at different levels of relative humidity.

- **Electronic states and energy levels:**

The absorption spectrum of PEDOT:PSS is almost identical to the absorption of *in situ* chemically polymerized PEDOT without PSS. Thin films (<500nm) of PEDOT: PSS are highly transparent in the visible range (transmittance> 80%). Part of the absorption occurs in the region of red (600 -750 nm), which gives the films a light blue appearance. Gustafsson et al. have studied PEDOT:PSS films deposited on ITO as electrode in an electrochemical cell. [27] **Figure 1.2.11** depicts the optical absorption spectra as a function of photon energy at different bias. The peak at 2.2 eV (560 nm), the band gap of absorption, reduces as the applied bias is increased and two new peaks appear at lower energies. The partly neutralized polymer obtained at a bias of -1.5 V is strongly absorbing in the visible range, while PEDOT in its oxidized form at +0.5 V is almost transparent in this region. This behavior may be exploited in electrochromic applications, like displays and smart windows.

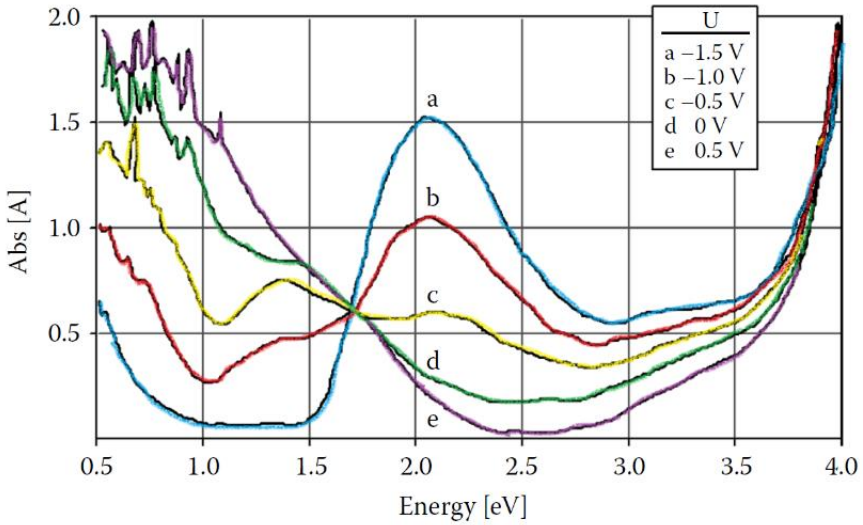

Figure 1.2.11: Optical absorption spectra of a PEDOT:PSS electrode in an electro chemical cell for different applied voltages: (a) –1.5 V, (b) –1.0 V, (c) –0.5 V , (d) 0 V, and (e) + 0.5 V. [16]

The two peaks at 0.5 eV and 1.4 eV in **Figure 1.2.11** indicate that the charge inserted electrochemically into the polymer electrode is stored as polarons or even bipolarons at high oxidation levels, creating new electronic states within the energy gap (see **Figure 1.2.12**). These new energy levels are broadened due to the amorphous nature of the film, the length

distribution of PEDOT segments, and interaction of charge carriers at high doping levels forming bands without detailed structure.

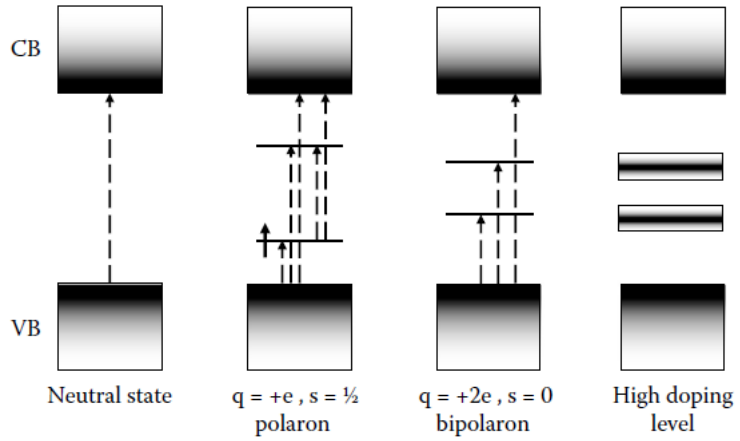

Figure 1.2.12: Energy level diagram of conductive polymers. Dashed arrows indicate possible electronic transitions caused by light absorption. The polaron state is formed by a localized hole gaining energy due to the coulombic relaxation of its vicinity. In case of high current densities new levels are created as bipolarons or even new bands within the energetic gap opening multiple possibilities for subband absorption.

- **Electrical conductivity:**

PEDOT:PSS is an intrinsically conducting polymer with metal-like properties. In contrast to solid ion conductors the charge transported here stems from free charge carriers. The thiophene rings form a conjugated π system being heavily p-doped. Owing to the oxidative polymerization reaction triggered by radicals one net free positive charge per three to four thiophene rings is created. PSS does not contribute to charge transport directly but acts as a template to keep PEDOT in the dispersed state and provides film-forming properties. The dissociated sulfonate groups balance the charges of the cationic PEDOT by forming a stable salt. The conductivity σ is defined by the product of elemental charge (e), charge carrier mobility (μ), and density of charge carriers (n). In case of ambipolar materials, both charge carrier species contribute according to

$$\sigma = e\mu_p n_p + e\mu_n n_n \qquad 1.2.4$$

In case of PEDOT:PSS, only holes contribute to the charge transport. Injected free electrons will immediately recombine at oxidized PEDOT sites, hence the transport of electrons does not contribute to the overall current.
The analysis of charge transport and accumulation in PEDOT:PSS is the main topic of this work, and physical models developed for this scope will be discussed in detail in **section 1.4**. These models will be focused on the interpretation of one of the most relevant aspect of PEDOT:PSS for applications, which is its double electronic and ionic conductivity.

1.2.7: Applications of PEDOT:PSS in organic electronics and bioelectronics

The properties briefly described in the previous paragraphs are some of the main reasons why PEDOT:PSS represents a workhorse of organic electronics. PEDOT:PSS is a polymeric mixed ion-electron conductor with a relatively high ionic conductivity and specific capacitance. The density of holes in PEDOT:PSS can be reversibly modulated over a wide range by the compensation with ions provided from an electrolyte. This makes PEDOT:PSS ideal as the electrode in ion-based energy storage devices, such as supercapacitors, and as the channel in electrochemical transistors and sensors. The swift and reversible modulation of the hole density is also accompanied with a switch in color between dark blue and transparent. PEDOT:PSS has therefore served as the pixel electrode in electrochromic displays. Moreover, PEDOT:PSS is a first choice as the signal translating device in various bioelectronics devices operating in physiological media, such as in biosensors, electrochemical transistors, electrodes interfacing with neuronal systems, and as the electrodes in organic electronic ion pumps. [28]

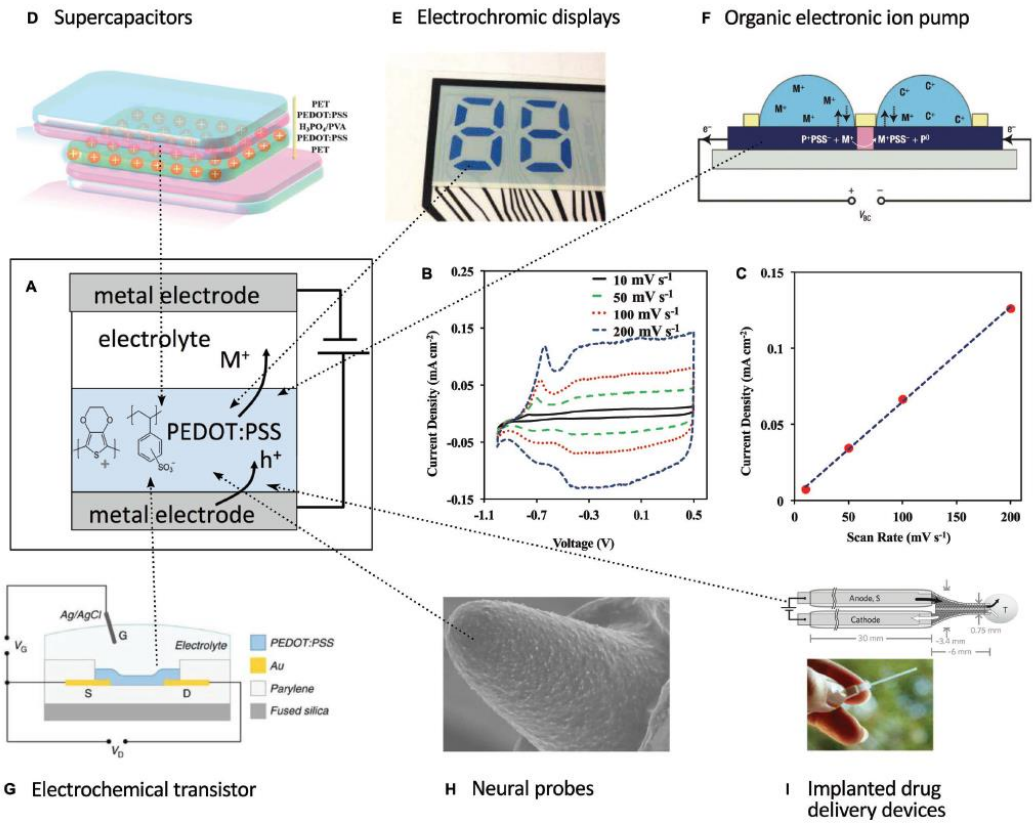

Figure 1.2.13: **a)** Schematic illustration of an experimental setup comprising PEDOT:PSS, an electrolyte layer and two metallic electrodes. **b)** Cyclic voltammogram of the setup, also including an Ag/AgCl reference electrode, at different scan rates in 0.1 m KCl. **c)** The current level, measured at 0 V versus the reference electrode, for various scan rates. **d–i)** Organic devices which utilize the volumetric capacitance and the electron-ion coupling in PEDOT:PSS. **d)** PEDOT:PSS supercapacitors can be used in flexible and printed electronics; they exhibit a specific capacitance $C^* \approx 50–100$ F/cm^3 that compares well to high-performing porous carbon supercapacitors. **e)** PEDOT:PSS electrochromic displays (ECD).Electrochromic materials change their color due to charge accumulation–depletion processes. **g)** Organic electrochemical transistors (OECT) and sensors based on PEDOT:PSS. The volumetric capacitance C is a key parameter for OECTs in that it determines the transconductance, **h)** Neural probes (NP).NP represents a biocompatible interface providing a signal transfer between electrodes and in vivo neural tissues. The performance of NP is related to their charge storage capacity and electrical impedance. **f)** PEDOT:PSS-based organic electronic ion pumps (OEIP) and **i)** implantable drug delivery devices (IDDD). OEIPs translate electronic signals into ion fluxes and IDDD can locally deliver biological molecules and neurotransmitters at high spatiotemporal resolution. PEDOT:PSS in OEIP and IDDD electrodes serves as ion-to-electron converters and hence the pumping/delivery rates are governed by the material capacitive response.

A global overview of the main applications of this promising material is provided in **Figure 1.2.13**. Some PEDOT:PSS-based realizations in the field of bioelectronics are introduced below.

- **Organic electrochemical transistors (OECTs) and biosensors:**

Organic electrochemical transistors (OECTs) make effective use of ion injection from an electrolyte to modulate the bulk conductivity of an organic semiconductor channel. OECTs can provide high currents as the whole film is contributing to the charge transport in the channel, in contrast to FETs where only a thin layer adjacent to the dielectric or aqueous system is contributing. As each polaron is compensated by an ion, a change in the doping level requires the transport of ions in and out of the polymer film (see **Figure 1.2.14**). The first OECTs were developed by the Wrighton group in the mid-1980s and were based on electrochemically polymerized polyaniline and poly(3-methylthiophene). Although the performance and stability were improved in the following years, the widespread use was hampered due to complicated electrochemical deposition methods used at that time to manufacture transistor channels. The introduction of chemically polymerized PEDOT:PSS as the active material for OECTs constituted a step forward in terms of processability and performance. [13]

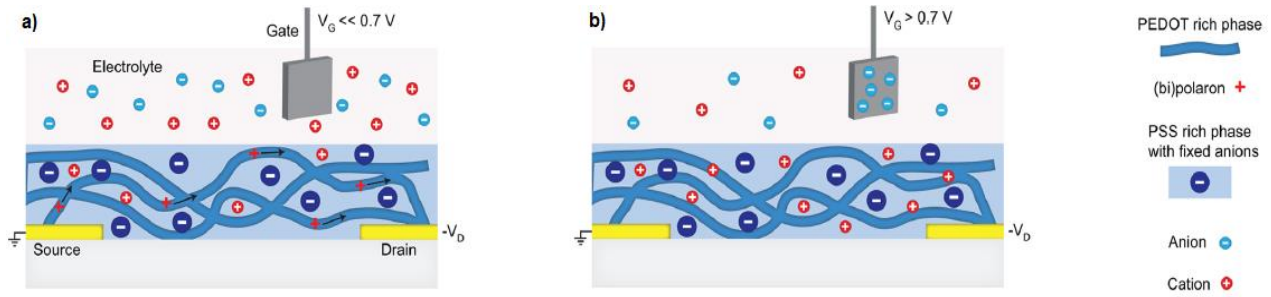

Figure 1.2.14: PEDOT:PSS-based OECTs. **a)** A conductive channel is formed for gate voltages that cause the PEDOT to be in the doped state. The application of a drain voltage generates a current from source to drain contacts **b)** By reversing the gate potential, the PEDOT can be undoped by replacing the polarons with ions from the electrolyte, rendering the channel nonconductive. The ionic transport in and out of the film is facilitated by the gate electrode, either by charging and discharging of the electric double layer of the electrode (shown) or by electrochemical reactions.

The PEDOT:PSS-based OECT is today widely used in the organic bioelectronics' community. Groups have used this device in combination with different receptor or selective membranes to detect and monitor, e.g., ascorbic acid, marine diatoms in the seawater medium, dopamine, acetylcholine, and glutamate. Further, recently PEDOT-OECTs were successfully utilized in combination with optical techniques to monitor the integrity and status of the tight junctions of formed tissues. [13]

- **Neural probes:**

The benefits of the electrical interface with nervous tissue are huge, as electrical stimulation is already in clinical use for treating diseases and disorders like Parkinson's, epilepsy, deafness, chronic pain, and blindness. Moreover, recording of neural signaling is an invaluable tool to understand and map the function of the brain, as well as for controlling artificial limbs. Conducting polymers have been widely used to improve the electrode–tissue interface, in terms of both electrical properties and biocompatibility. Recently, thin and flexible high-density multielectrode arrays for neural recording have been developed (NeuroGrid, **Figure 1.2.15**). In these devices chemically polymerized PEDOT:PSS was spin-coated and sequentially

patterned, an approach that deviates from earlier work. These multielectrode arrays have allowed scientists, for the first time, to record from and track individual neurons from the surface of the brain for extended periods of time. [29]

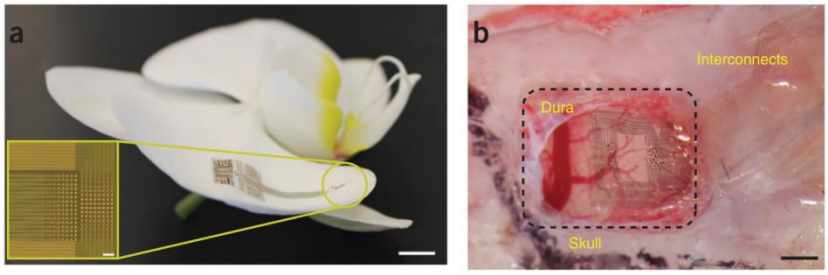

Figure 1.2.15: a) The NeuroGrid conforms to the surface of an orchid petal (scale bar, 5 mm). Inset, optical micrograph of a 256-electrode NeuroGrid (scale bar, 100 μm). Electrodes are 10 × 10 μm2 with 30-μm interelectrode spacing. **b)** The NeuroGrid conforms to the surface of the rat somatosensory cortex. The edge of the resected dura is visible at top left of the craniotomy (scale bar, 1 mm).

- **Implanted drug delivery devices:**

Many drugs provide their therapeutic action only at specific sites in the body but are administered in ways that cause the drug's spread throughout the organism. This can lead to serious side effects. Local delivery from an implanted device may avoid these issues, especially if the delivery rate can be tuned according to the need of the patient. For this scope, Jonsson et al. [30] demonstrated the efficacy of an implantable organic electronic delivery device for the treatment of neuropathic pain in an animal model. Researchers realized an organic electrochemical pump (OEIP- a device able to transduce electronic currents in ionic fluxes) based on a thin layer of PEDOT:PSS on a polyethylene terephthalate (PET) substrate, encapsulated by an ionic and electronic insulator (see **Figure 1.2.16**). Devices were implanted onto the spinal cord of rats, and 2 days after implantation, local delivery of the inhibitory neurotransmitter g-aminobutyric acid (GABA) was initiated. Highly localized delivery resulted in a significant decrease in pain response with low dosage and no observable side effects.

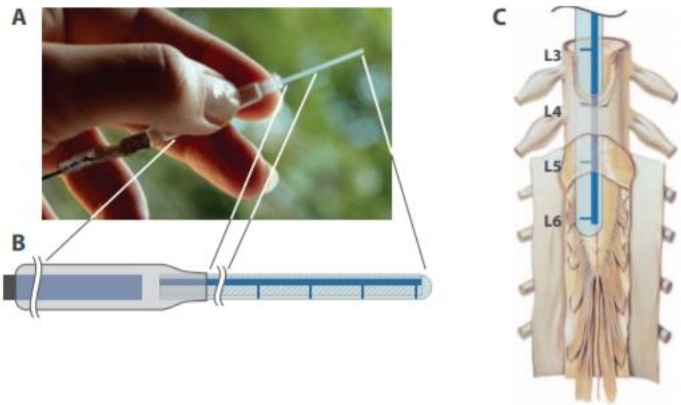

Figure 1.2.16: The implantable OEIP and its spinal target. **(A)** Photograph of the device. **(B)** Schematic illustration: electrical connection (left); reservoir with internal electrode (center); delivery channel and outlets (right). Total length 120 mm; reservoir diameter 6 mm, length 60 mm; delivery tip width 1.2 mm, length 40 mm, thickness about 0.2 mm. **(C)** Depiction of the four outlets aligned with the sites where the sciatic nerve bundles enter the spinal cord. The figure shows a human spinal cord, but the roots L3-L6 refer to the root levels of a rat spinal cord.

1.3 Modelling charge accumulation and transport in PEDOT:PSS

Conjugated polymer–polyelectrolyte blends combine and couple electronic semiconductor functionality with selective ionic transport, making them attractive as the active material for organic electronics and bioelectronics. These applications use electrolytes or operate under elevated hygroscopic conditions, which render the counterions mobile and thus make the coupling of the electronic and ionic transport crucial. Although extensively studied and explored, fundamental knowledge and accurate quantitative models of the coupled ion-electron functionality and transport are still a challenging field of research, essential for future developments and optimizations of devices based on this aspect.
This section aims to introduce for this scope an extended drift-diffusion model, able to reproduce a wide range of experimental charging and transport data and to provide a coherent theoretical framework for the system as well as local electrostatic potentials, energy levels, and charge carrier concentrations. [1]

1.3.1 A drift-diffusion model for charge transport in conjugated polymers

When a conjugated polymer is immersed in an electrolyte, there are three main mechanisms for charge transport: diffusion, drift (also called migration), and convection. [31] Diffusion occurs in the presence of concentration gradients. Diffusion is called Fickian when the probabilities for particle movement are equal in all directions, i.e., if the medium is isotropic. Drift is the movement of a particle under a driving force, such as the movement of a charged particle under an applied voltage. The existence of electric fields in the polymer must be considered. Since both ions and holes are charged species, one cannot a priori neglect their movement in electrical fields nor their electrostatic interactions. Lastly, convection is the movement of a particle carried in the flow of a fluid, like a boat in a current. This last mechanism can often be neglected in conjugated polymers. For ion transport, it is neglected because there are no significant fluid flows through the conjugated polymer (although solvent diffuses into the polymer independently of ion transport, this occurs at a slower time scale and does not carry ions). For hole transport, it is neglected because the polymer chains do not flow as a liquid does (although the chains do undergo local movements such as changes in conformation). In the electrolyte, convection is also neglected since the solution is unstirred.
A general model for charge transport in conjugated polymers was developed in 2009 by Wang et al. [31] The main goal of their work was to determine fundamental equations that would account for the dominant features of charge transport in conjugated polymers during electrochemical switching between fully oxidized and reduced states. Model development was informed only by experimental results obtained during electrochemical reduction (de-doping) of a polypyrrole doped with dodecylbenzenesulfonate (PPy(DBS)) film, covered by an ion barrier (see **Figure 1.3.1** for a sketch of the physical system), which constrains the charge compensating cations to enter the film only at the edge. In a cation-transporting polymer like PPy(DBS), as holes are extracted at the electrode, charge compensating cations enter from the electrolyte. The cation concentration determines the volume of the polymer and is also directly related to the oxidation level of the polymer, which in turn determines its color. During electrochemical reduction, the edge of the film lighten, and this light color travels as a front to the center of the film. At the same time, the height of the film increases when and where the color lightens, and the increase in height is directly proportional to the change in color intensity. In this way, it is possible to measure the dispersion and the velocity of a reduction front. [32]
Wang's model couples charge transport equations with Poisson's equation, and includes ion transport (in the polymer and in the electrolyte), hole transport (polarons, bipolarons), and the electric fields that drive transport (both those that are applied to the material and those

generated by the charges themselves). The equations used in that work are similar to the standard ones for describing charge transport in crystalline inorganic semiconductors like silicon, and therefore may be too simple to account for all the physics occurring in the conjugated polymer during redox, a process that has no inorganic analog. However, they provide a first approximation, a starting point in the model-building process. Since the equations are coupled and since they have nonlinear parameter dependencies, they cannot be solved analytically for any general case. Thus, they are solved numerically using finite element modeling. After solving for the initial conditions (the polymer is either fully oxidized or fully reduced before a switching potential is applied at the boundaries), the ion, hole, and potential profiles are allowed to evolve in response to each other, simulating the redox process.

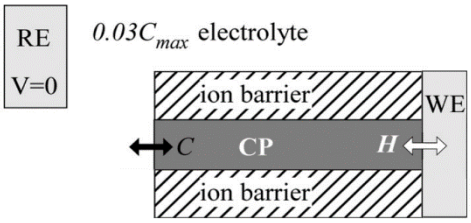

Figure 1.3.1: Schematic of the physical system, showing the potentials on the working (WE) and reference/counter (RE) electrodes during electrochemical reduction of a cation-transporting polymer covered by an ion barrier, the bulk concentration of cations in the electrolyte ($0.03C_{max}$, where C_{max} = 3M), and the interfaces that ions (C) and holes (H) can cross.

The first modeling equation (the continuity equation) expresses the conservation of species:

$$\frac{\partial C_i}{\partial t} = -\nabla \cdot \boldsymbol{J_i} \qquad 1.3.1$$

where C_i is the concentration of species i (mol/cm^3) and $\boldsymbol{J_i}$ is the particle flux (mol/(s·cm^2)). C_i is a dynamic variable that depends on space and time, so $C_i = C_i(x,y,z,t)$. This equation has no source/sink terms and thus holds in the absence of species generation (e.g., by light) or annihilation. The flux $\boldsymbol{J_i}$ must be expressed in terms of the physical conditions. As mentioned previously, we ignore convection but consider diffusion and drift: $\boldsymbol{J_i} = \boldsymbol{J_i}^{diff} + \boldsymbol{J_i}^{drift}$. Commonly used equations for each of these components in inorganic semiconductors are

$$\boldsymbol{J_i^{diff}} = -D_i \boldsymbol{\nabla} C_i \qquad 1.3.2$$

where D_i is the diffusion coefficient (cm^2/s) and

$$\boldsymbol{J_i^{drift}} = z_i \mu_i C_i \boldsymbol{E} \qquad 1.3.3$$

where z_i is the positive or negative charge per species molecule (ion or hole); μ_i is the mobility (cm^2/(V·s)); and $\boldsymbol{E}$ is the electric field, where $\boldsymbol{E} = -\boldsymbol{\nabla}\phi$ and ϕ is the electric potential. Substituting the flux equations into Eq. 1.3.1 results in a partial differential equation (PDE) for the rate of change of the concentration of species i (the cations or the holes) at any location inside the polymer

$$\frac{\partial C_i}{\partial t} = -\boldsymbol{\nabla} \cdot \boldsymbol{J_i} = -\boldsymbol{\nabla} \cdot (-D_i \boldsymbol{\nabla} C_i - z_i \mu_i C_i \boldsymbol{\nabla} \phi) \qquad 1.3.4$$

where D_i and μ_i are not constant, but functions of the oxidation level of the polymer. Moreover, electric fields can be modeled with Poisson's equation, which gives the potential in terms of the net charge density Q (C/cm^3):

$$\varepsilon_0 \nabla \cdot (\varepsilon \nabla \phi) = -Q = -\sum_{i=1}^{n} z_i C_i \qquad 1.3.4$$

Here ε_0 is the permittivity of a vacuum and ε is the dielectric constant of the material.
The electrolyte is added as a second material, as illustrated in **Figure 1.3.2**. Charge transport in the electrolyte is governed by the following PDEs. These are essentially identical to those used in polymer, but instead of holes, eq 1.3.6 accounts for the anions, and the net charge in eq 1.3.7 is simply given by the difference between the anion and cation concentrations at a given location.

$$\frac{\partial C_e}{\partial t} = -\nabla \cdot (-D_{Ce} \nabla C_i - \mu_{Ce} C_e \nabla \phi) \qquad 1.3.5$$

$$\frac{\partial A}{\partial t} = -\nabla \cdot (-D_A \nabla A + \mu_A A \nabla \phi) \qquad 1.3.6$$

$$\varepsilon_0 \nabla \cdot (\varepsilon \nabla \phi) = A - C_e \qquad 1.3.7$$

where C_e indicates the cation concentration and A the anion concentration in the electrolyte. In the electrolyte, the cations are assumed to have a 10× higher mobility than the anions since in Wang's experiments the Na^+ is much smaller than the DBS^-. The cation mobility in the electrolyte is assumed to be 1000 times higher than in the polymer, based on reported diffusivity values in the literature. [33] The Einstein relation was assumed to be valid, and the dielectric constant of the electrolyte was set to the same value as that for the polymer. The electrolyte was set to be 10× longer than the polymer, based on the experimental configuration.

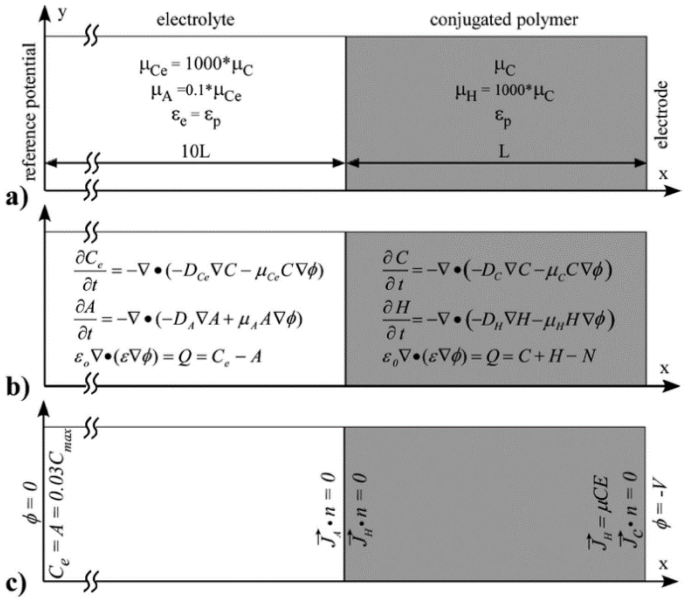

Figure 1.3.2: **(a)** Parameters, **(b)** PDEs, and **(c)** boundary conditions used during reduction of the PPy(DBS) film.

To solve the PDEs which describe the system, it is necessary to define boundary conditions (i.e., voltages, fluxes) and initial conditions. The boundary conditions (BCs) describe how the charges get in and out of the material, and they should correspond to the physical conditions imposed at the polymer/electrode and polymer/electrolyte interfaces. At the polymer/electrode boundary, there is no ion flux across the interface, as shown in **Figure 1.3.2** ($\boldsymbol{J_C} \cdot \hat{\boldsymbol{n}} = 0$, where is $\hat{\boldsymbol{n}}$ a unit vector oriented perpendicular to the boundary). Let us set x=0 corresponding to the polymer/electrolyte interface, and express lengths in units of the size of the experimental system (L = 150 μm). On the left-hand side of **Figure 1.3.2** ($x = -10$) we can assume a second electrode, equivalent to an experimental configuration in which the counter and reference electrodes are shorted. At this electrode/electrolyte boundary, the anion and cation concentrations were set equal to the salt concentration in the bulk of the electrolyte. Since researchers used a 0.1 M electrolyte concentration for the experiments, this was also used in the model system (equal to $0.033C_{\max}$, since $C_{\max}$ = 3 M was assumed to be the maximum concentration of holes/ions in the polymer). The potential at that boundary was zero during the reduction process. The interface between the electrolyte and the polymer ($x = 0$) had a no-flux condition for anions and holes, keeping them confined in the electrolyte and polymer, respectively. In the initial conditions for the simulation, anion and cation concentrations throughout the electrolyte are set equal to $0.033C_{\max}$. In the polymer, since the model describes a reduction process, we assume an initial fully-oxidized state ($H = H_{max}$ and $C = 0$). When the polymer is fully-oxidized, the current at the polymer-electrode interface depends on the number of available sites onto which a hole can potentially be placed, which is equal to the number of sites occupied by cations. Because ions cannot be injected in the electrode, the initial current value at the electrode/polymer interface can be assumed to be $\boldsymbol{J_h} = \mu_h C\boldsymbol{E}$. At time t = 0, the applied (over)potential to the working electrode (WE) is set to −1 V, which initiates the reduction of the film in contact with the electrolyte.

The main results of the Wang's model are reported in **Figure 1.3.3** [31]. The concentrations of the charged species are shown in when the reduction front has reached halfway into the polymer. In the electrolyte region, both anions and cations are depleted near the surface of the polymer, their concentrations returning to bulk values by x = −4. Just at the interface, though, the cation concentration rises steeply, forming a thin double-layer (more clearly seen in the inset of **Figure 1.3.3 a**). The electric field (**Figure 1.3.3 a**) creates a sharp build-up of cations in the electrolyte (C_e) at the electrolyte/polymer boundary, i.e., the cations form a double-layer. The reason for this is that the ion migration flux is the product of three terms: ion mobility, ion concentration, and electric field. The electric field is nearly zero in the bulk of the electrolyte (on the left), becomes high near the electrolyte/polymer boundary, drops to a low value in the reduced part of the polymer, and returns to almost zero in the conducting region. The ion concentration in the bulk of the electrolyte is ∼30 times lower than in the reduced polymer, but the mobility is 1000 times larger. Thus, the flux in the electrolyte near the polymer ($\mu_{Ce}C_eE$ = very high × low × very high) is far greater than in the reduced part of the polymer ($\mu_C CE$ = low × high × low). The faster arrival of cations at the boundary than they can be taken up by the polymer causes the pile-up of ions at the interface. Diffusion, which opposes such concentration gradients, limits the size of this double-layer.

The potential as a function of position is shown at three time-snapshots in **Figure 1.3.3 b**. Initially, when the polymer is in its conducting, oxidized state, all of the voltage is applied across the electrolyte. As the polymer is reduced, the potential across it rises, but even so, halfway through the reduction process approximately 70% of the potential drop is still across the electrolyte. The largest part of this drop occurs across the depletion and double layer regions. The profile does not change significantly thereafter: at the end of the process, only slightly more of the potential is dropped across the polymer. The front position moves and broadens as $t^{1/2}$ in the polymer and the effective front velocity is still linearly proportional to the applied

potential. These observations correctly reproduce the experimental results and confirm the capability of the model of reproducing the dominant behaviors.

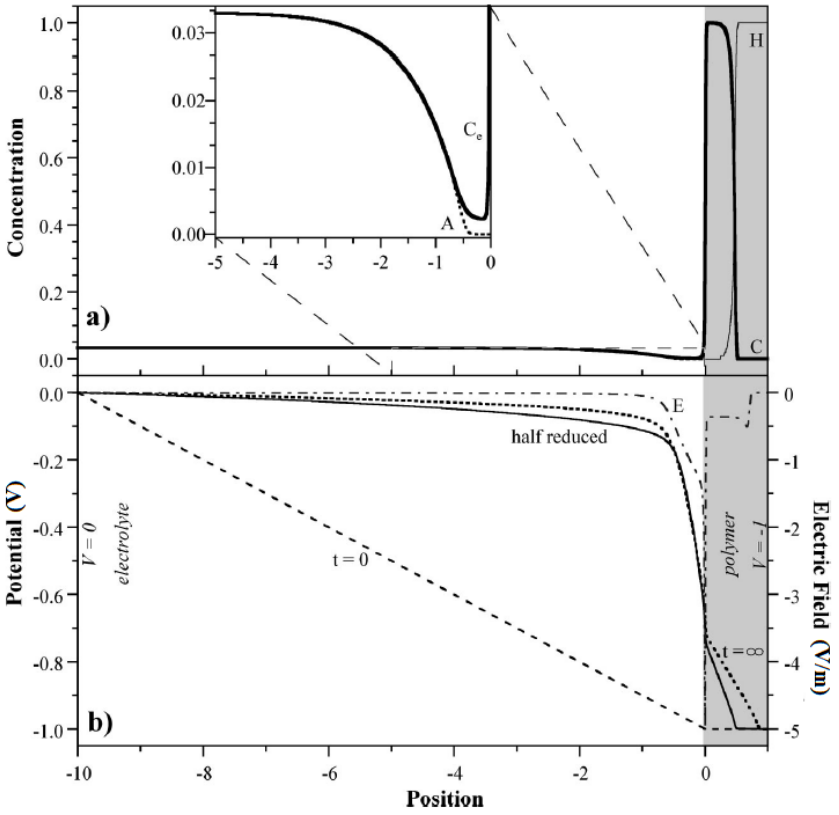

Figure 1.3.3: Simulation results of Wang's model. Position and concentration are expressed respectively in units of L and C_{max}. The gray on the right-hand side indicates the location of the polymer. **(a)** Anion, cation, and hole concentrations as a function of position. The inset shows a close-up of the electrolyte adjacent to the polymer. **(b)** The potential as a function of position at three different times and the electric field *E* (dot-dashed line) when the film is halfway reduced.

1.3.2 The volumetric capacitance of PEDOT:PSS

PEDOT:PSS is a polymeric mixed ion-electron conductor with a relatively high ionic conductivity and specific capacitance. This makes PEDOT:PSS ideal as the electrode in ion-based energy storage devices, such as supercapacitors. [28] Generally, charge storage in supercapacitors is due to electric double-layers formed along electrode/electrolyte interfaces or is related to electrochemical processes (commonly termed pseudo-capacitance). The latter involves redox reactions including charge transfer across the electrolyte–electrode interface. Mechanisms of supercapacitive behavior and electron-ion coupling in conductive polymers are experimentally studied using cyclic voltammetry. In the forward voltage scan, positive cations (M+) escape the PEDOT:PSS layer and are replaced by positive holes that are injected into the PEDOT from the electrode. This process is reversed in the backward scan and the hole density in the PEDOT is reduced. A typical voltammogram exhibits current peaks followed by the current plateaus, see **Figure 1.3.4**. The current peaks can be reproduced by the Butler–Volmer electrochemical model describing a faradaic current due to redox reactions, whereas the current plateaus can be described by a phenomenological term giving rise to the capacitive. As a result, it is commonly assumed that the supercapacitive voltammograms of conducting polymers is due to pseudocapacitive processes involving faradaic reactions. Note however that

the origin of the phenomenological capacitive current has never been properly explained from a theoretical point of view.

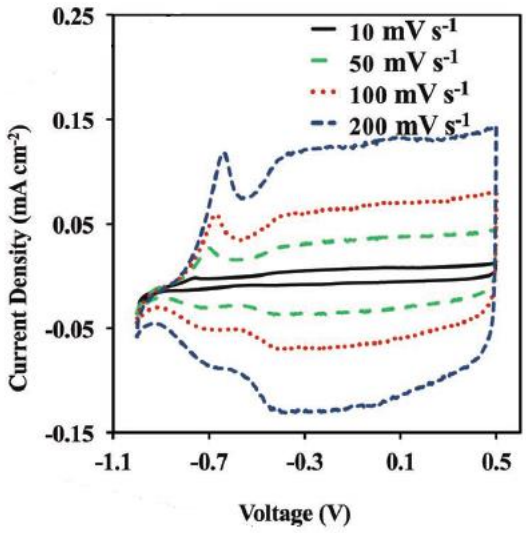

Figure 1.3.4: Cyclic voltammogram of PEDOT:PSS, also including an Ag/AgCl reference electrode, at different scan rates in 0.1 M KCl.

Besides cyclic voltammetry, the capacitive behavior and the ionic–electronic transport interplay in conductive polymers are also studied using other techniques. In "moving front" experiments the motion of the boundary between doped and undoped regions is monitored by dynamic color changes, as seen in section 1.3.1. Conductance and impedance spectroscopy studies have been applied to three-terminal electrochemical transistors based on PEDOT:PSS whose resistance is controlled via a gate by an ionic inflow from the electrolyte. Even though these electrode and device systems, and their underlying physics, are identical to those studied by the cyclic voltammetry, the interpretations made from the analysis of the results are strikingly different. In particular, the theoretical treatment of the experiments (such as Wang's model) do not typically assume any redox reactions and is solely based on the coupling between electronic and ionic motion as described by the drift-diffusion equation. Hence, even after decades of polymer research the most fundamental questions concerning the nature of capacitive behavior and the electron-ion coupling in these materials still remain unsolved and are highly controversial. Wang's model, despite its capability to simulate moving reduction front experiments, fails to give a fundamental interpretation of the volumetric capacitance of conjugated polymers (CPs)-polyelectrolyte (PE) blends, such as PEDOT:PSS.

Volkov et al. [34] demonstrated that the major contribution to the capacitance of the two-phase PEDOT:PSS originates from electrical double layers formed along the interfaces between nanoscaled PEDOT-rich and PSS-rich interconnected grains that comprises two phases of the bulk of PEDOT:PSS. In that work, scientists investigated the nanomorphology of PEDOT:PSS film with tapping-mode atomic force microscopy (AFM). **Figure 1.3.5 a** and **b** shows the phase and topography images of a 500 × 500 nm area of the PEDOT–PSS film. 10–20 nm wide grains composed of small elongated structures are observed in the phase image. The relatively strong contrast in the phase image (full scale equals 20°) is associated with a different chemical composition. For polymer systems, with phase images captured under moderate tapping conditions, bright areas (high phase signal) in the phase image can be assigned to a relatively hard phase attributed to the PEDOT rich phase. On the other hand, the lower phase signal (dark domains) is referred to the excess of PSS since PEDOT:PSS (PH1000) has a PSS/PEDOT ratio about 2.3/1. Surface areas rich in this hygroscopic polyelectrolyte are expected to swell and

soften due to ambient humidity, this also explained why the PSS region is slightly higher in the corresponding topography image. For these reasons, it's possible to guess that PEDOT:PSS is composed of a continuous amorphous PSS phase hosting many nanometer-sized PEDOT crystallites and dispersed individual PEDOT chains in the PSS matrix.

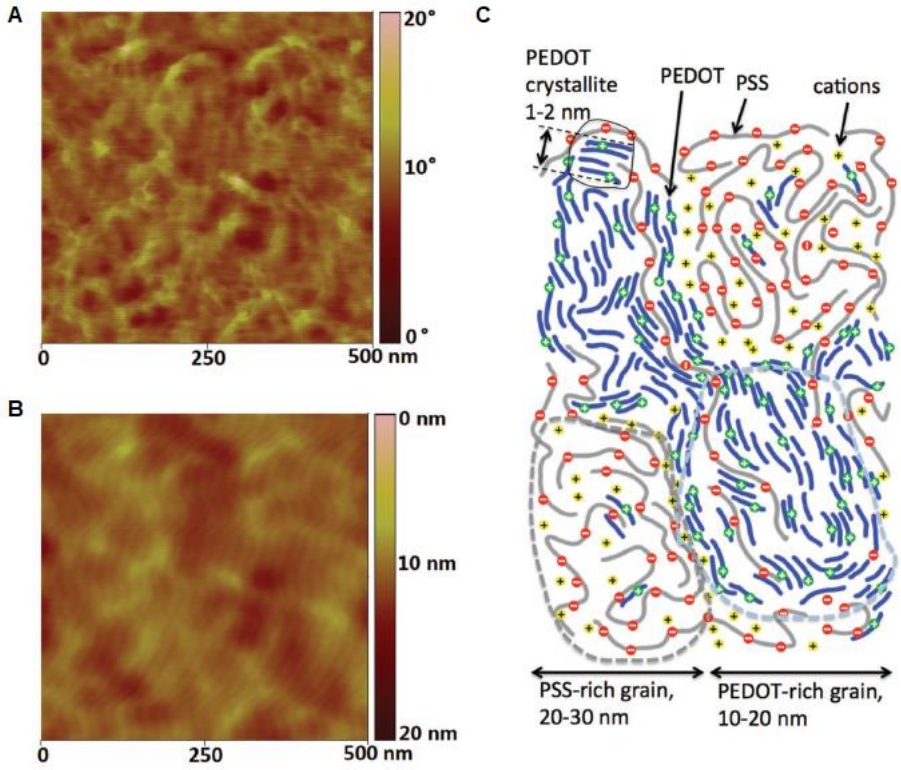

Figure 1.3.5: a) Phase images and **b)** topography of a PEDOT–PSS film obtained with tapping-mode AFM at a scale of 500 × 500 nm2. **c)** Schematic diagram of the morphology model.

The resulting morphology model is sketched in **Figure 1.3.5 c**. PEDOT:PSS represents a two phase-system consisting of PEDOT-rich and PSS-rich grains of the dimensions of about 10–30 nm. PEDOT-rich grains support primarily hole conductivity, whereas PSS-rich grains support the ion conductivity. The PEDOT-rich grains consist of PEDOT crystallite domains of 1–2 nm (composed of up to ≈5 chains) embedded in the amorphous PSS matrix. Because the system exhibits high conductivity in the oxidized state, the PEDOT crystallites and chains form a percolative network (presumably via π–π stacking) providing transport paths for the holes throughout the whole structure. Such the morphology invites to another mechanism for charge storage with electric double layers formed at the interface between the electronically conducting PEDOT rich phase and the ionically PSS rich phase. This mechanism resembles the one present in supercapacitors based on porous electrodes storing the charge by the formation of electric double layer. **Figure 1.3.6 a** shows a schematics of the two-phase 2D model representing a nanopore geometry. [34] An internal region with a width w_{PEDOT} = 10 nm is an electronically conductive phase (corresponding to PEDOT-rich grain), and the outer region with a width w_{PSS} = 20 nm is an ion conductive phase (corresponding to PSS-rich grain). Such a geometry can be exploited to simulate the capacitive behavior of a PEDOT:PSS film. We assume that fixed negative charges (residing on PSS chains) are homogeneously distributed in the ion conductive region (c_{fixed} (**r**) = 1 M) and only ions can enter this region. The high electrical conductivity of PEDOT:PSS in the oxidized state in the presence of solvent indicates that the PEDOT nanocrystallites are not disrupted by the presence of the counterions, which are not

inserted between the PEDOT chains forming the π–π stacking. Hence, we assume that there are no fixed charges inside the PEDOT-rich phase and ions cannot enter it.

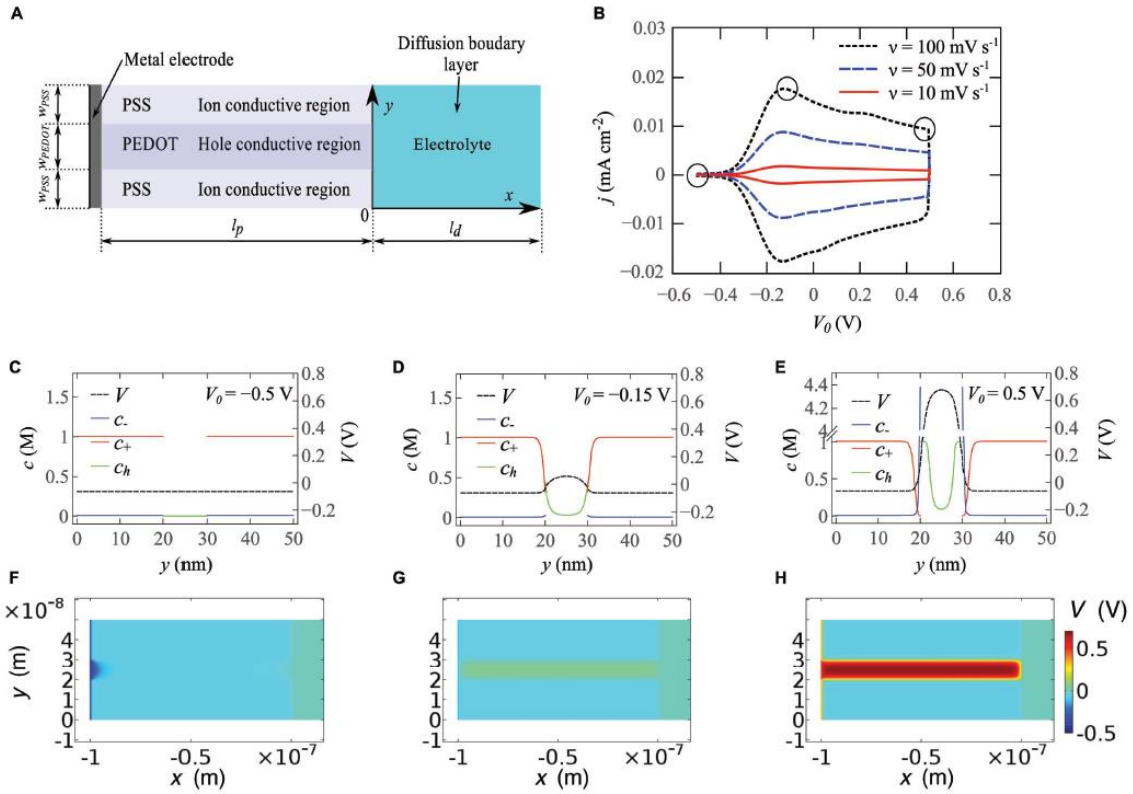

Figure 1.3.6: a) Schematics of the electrode system for two-phase model. **b)** Cyclic voltammograms calculated according to two-phase model for different scan rates. **c,d,e)** Concentrations and corresponding potential profiles at different applied voltages V_{app} for two-phase model. Profiles are shown along y-axis at x = 50 nm. c_-, c_+, and c_h correspond to the concentration of mobile anions, cations, and holes, respectively. **f,g,h)** 2D potential profiles at different applied voltages V for two-phase model.

Figure 1.3.6 b shows cyclic voltammograms calculated by applying this model. The current density is obtained by integration over the polymer film $j_{direct} = \frac{F}{W_p}\iint \frac{\partial c_h}{\partial t} ds$, where the width $w_p = 2w_{PSS} + w_{PEDOT}$, c_h is the hole concentration and F = 96485.33 C/mol the Faraday constant. When the applied potential V_{app} = −0.5 V the polymer film is fully reduced and $c_h \approx 0$ M (see. **Figure 1.3.6 c**). The potential drops only at the metal/polymer and polymer/solution interfaces while inside film has a constant value (see **Figure 1.3.6 c**, **f**). In particular, the potential in the both ion and hole conductive regions is ≈ − 0.06 V and corresponds to the Donnan potential

$$V_D \approx \frac{RT}{F} ln\left(\frac{c_+^{el}}{c_+^{p}}\right) \qquad 1.3.8$$

caused by a different concentration of cations in the polymer film and in the electrolyte. The forward increase of the applied voltage (V_{app} = − 0.15 V) leads to an injection of holes into the pore, see (see **Figure 1.3.6 d**). The injected holes attract negative ions from the ion conductive region, which leads to the formation of double layers at the pore interface (see **Figure 1.3.6 d, g**). Outside the double layers the ion concentrations remain unchanged during the whole cycle. As a result, the potential inside the ion conductive region also remains constant and is equal to

the Donnan potential. When the applied voltage increases the potential inside the pore increases because of the increase of the hole concentration. The current density reaches its peak value (manifested as the redox peaks in the voltammograms) when the concentration of holes near the interface of the pore reaches half of the concentration of the accessible sites c°_{h}. When the applied potential $V_{app} \approx 0.5$ V the concentration of holes at the pore interface is equal to c°_{h}. As a result, a given voltage increase leads to an increase of the width of the hole layer (see **Figure 1.3.6 e, h**). In agreement with the experiment the calculated current depends linearly on the scan rate. The volumetric specific capacitance C^* extracted from the calculated voltamogramms for the two-phase model is $C^* \approx 10$ F/cm^3. This value is somehow smaller than the measured capacitance $C^* = 34$ F/cm^3. It should be noted however that the model geometry represent the lowest estimate of the capacitance: the realistic 3D geometry of bulk PEDOT:PSS would correspond to larger interface area and therefore larger C^*.

1.3.3 Chemical potential-electric double layer coupling in PEDOT:PSS

In section 1.3.1 and 1.3.2, two different approaches have been discussed to model charge transport and accumulation in conjugated polymer-polyelectrolyte(CP-PE) blends. Wang's model, based on the drift-diffusion approach, reproduces some dynamic current characteristics of CP-PE blends, but fail to reproduce the experimentally observed volumetric capacitance of PEDOT:PSS (24), because the electronic and ionic charge carriers are treated as if they are existing in the same phase, with no electrostatic energy cost in charging the material, except from the contribution arising from diffusion gradients. Volkov's model provides a morphological interpretation of the volumetric capacitance, and simulates the capacitive behavior of PEDOT:PSS by explicit implementation of two-dimensional (2D) CP nanopores, but his approach is too computationally expensive to model realistic devices and does not consider fundamental electronic properties such as the chemical potential of holes.
A more advanced modeling of CP-PE blends, which combines the strengths of the previous approaches, has been developed by Tybrandt et al. [1] In that work, scientists proposed a two-phase model, which couples the chemical potential of the holes, in the conjugated polymer, with the electric double layer residing at the conjugated polymer–polyelectrolyte interface. The main idea of this approach is the introduction of two distinct electrostatic potentials for the electronic (CP) and ionic (PE) phases, implemented by Poisson's equation in a drift-diffusion approach.

- **The chemical potential of holes in PEDOT:PSS**

In amorphous or highly disordered semiconductors, such as PEDOT:PSS films, charge transport mainly occurs by hopping or tunneling among localized states. A theoretical description of these systems is provided by the Gaussian Disorder Model (GDM) [35]. According to this theory, the frontier orbitals different PEDOT molecules weakly overlap and form narrow bands (the overlap of HOMO levels generates the valence band, while the overlap of LUMO levels generates the conduction band) with a Gaussian density of states (gDOS):

$$g(E) = \frac{p_t}{\sqrt{2\pi}\sigma} exp\left[-\frac{(E - E_{DOS})^2}{2\sigma^2}\right] \qquad 1.3.8$$

p_t is the total number of hopping sites for holes, E_{DOS} the center of the gDOS (which can be approximated with the HOMO level of PEDOT) and σ the standard deviation of the gaussian, which is a measure of the energetic disorder. [36]

The hole concentration p is given by the integration of the density of occupied states (DOOS):

$$p = \int_{-\infty}^{+\infty} DOOS(E)\,\mathrm{d}E = \int_{-\infty}^{+\infty} \frac{g(E)}{1 + exp\left[\frac{(E-\mu_p)}{k_b T}\right]}\mathrm{d}E \qquad 1.3.9$$

where μ_p is the hole chemical potential (also called Fermi level in solid state physics), which can be evaluated as a function of p by solving eq. 1.3.9. Anyway, when the carrier concentration is small (with respect to p_t), μ_p can be expressed through the Boltzmann's approximation:

$$\mu_p = k_b T\, ln(p) - \frac{\sigma^2}{2k_b T} + E_{DOS} = k_b T\, ln(p)\ + eB \qquad 1.3.10$$

where e is the elementary charge and B a constant. **Figure 1.3.7** reports the Gaussian DOOS for different hole densities and shows the limit of applicability of eq. 1.3.10.

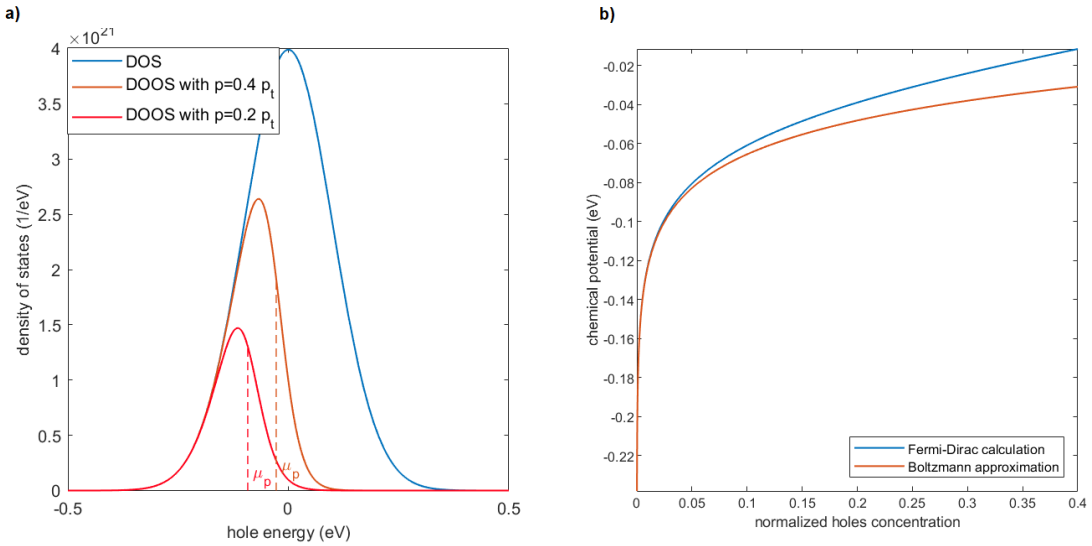

Figure 1.3.7: a) DOOS for different hole densities, by setting E_{DOS}=0, σ = 0.1eV and p_t = 1660 mol/m³. The chemical potential has been calculated by numerically solving eq. 1.4.9. **b)** Comparison between the Boltzmann approximation for the chemical potential and the value obtained by solving numerically the Fermi-Dirac integral in eq. 1.4.9.

➢ Tybrandt's model for PEDOT:PSS

The hole transport in CP-PE blends can be described by a modified drift-diffusion equation (eq. 1.3.11) [37], which includes the quasi-electric field arising from the shift in chemical potential due to changes in hole concentration. Although the Boltzmann approximation is only accurate for lower hole concentrations, it can also be used for higher concentrations because a capacitive term dominates the system in that regime, as discussed below. The ionic species ($c_\pm$) in the PE phase are described by the standard drift-diffusion equation (eq. 1.3.12), and the changes in concentrations are governed by the continuity equations (eq. 1.3.13 and eq. 1.3.14):

$$\boldsymbol{j_p} = -D_p\,[\boldsymbol{\nabla} p + \frac{F}{RT} p \boldsymbol{\nabla}(V_p + \mu_p/e)] \qquad 1.3.11$$

$$\boldsymbol{j_{c_\pm}} = -D_{c_\pm}\,(\boldsymbol{\nabla c_\pm} + \frac{F}{RT}\boldsymbol{c_\pm}\boldsymbol{\nabla} V_c) \qquad 1.3.12$$

$$\frac{\partial p}{\partial t} = -\nabla \cdot \boldsymbol{j_p} \qquad 1.3.13$$

$$\frac{\partial c_{\pm}}{\partial t} = -\nabla \cdot \boldsymbol{j}_{c_{\pm}} \qquad 1.3.14$$

where we assume isotropic diffusion and we apply Einstein's relation $D = uk_bT/e$ (being u the carrier mobility). It should be stressed that the electrostatic potential has two different distinct values within the electronic (V_p) and ionic (V_c) phases. This difference causes charging of the interface with holes and anions, thereby creating an electric double layer (EDL) with the voltage-independent volumetric capacitance (C_V) implemented through Poisson's equation

$$-\frac{\varepsilon}{e}\nabla^2 V_p = p - C_V\,(V_p - V_c) \qquad 1.3.15$$

Similarly, the PE phase is governed by Poisson's equation (eq. 1.3.16), with eqs. 1.3.15 and 1.3.16 coupling the charging and transport of the electronic and ionic charge carriers:

$$-\frac{\varepsilon}{e}\nabla^2 V_c = p + c_+ - c_- - c_{fix} \qquad 1.3.16$$

where c_{fix} indicates the fixed sulfonate acceptors on PSS. The hole concentration needs to be included in eq. 1.3.16, because a portion of the anionic charges are compensating for the holes in the EDL. **Figure 1.3.8** shows the energy diagrams for a PEDOT:PSS electrode immersed in an electrolyte [phosphate-buffered saline (PBS)] with a Ag/AgCl reference electrode. Two different voltages are applied: V_{app} = 0 (**a**) and V_{app}= −0.9 V (**b**) . The work function of the nonclean gold surface is set to W_{Au} = 4.5 eV and $W_{Ag/AgCl}$ = 4.7 eV. The vacuum level for the Ag/AgCl electrode is set to 0 eV as a reference.

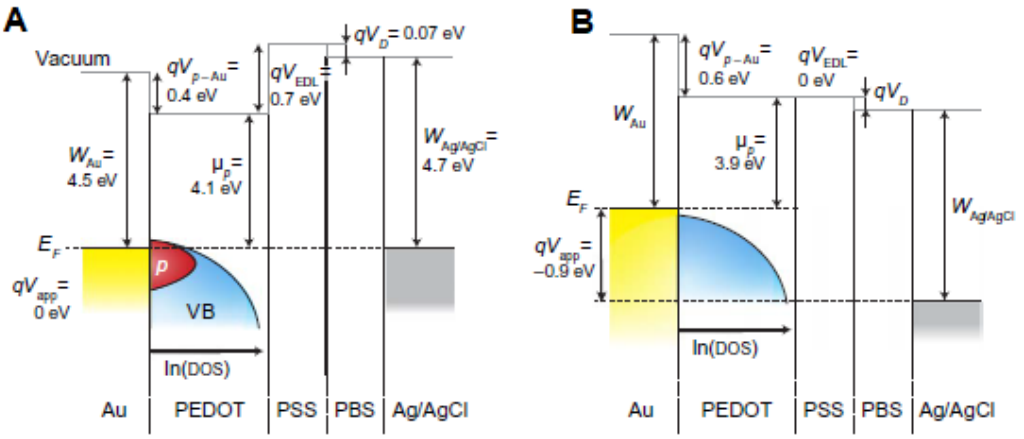

Figure 1.3.8: a) Energy diagram of a PEDOT:PSS electrode immersed in an electrolyte (PBS) with a Ag/AgCl reference electrode. VB, valence band; q, particle charge. The work function of pristine PEDOT is lower than that of gold, giving rise to an interface potential difference and heavy doping at V_{app} = 0 V. The charging of the PEDOT:PSS interface creates an EDL, where the potential difference is approximately proportional to the hole concentration. **b)** For V_{app} = −0.9 V, the PEDOT is essentially de-doped, which increases the potential at the gold-PEDOT interface while the EDL is discharged.

The system can be understood on the basis of three energy levels/potential differences, which depend on the doping level: the EDL potential difference, which causes the charging of the

interface and thereby doping of the semiconductor; the chemical potential of holes, which increases with doping level; and the gold-PEDOT interface potential difference, caused by differences in the work function for gold and PEDOT. From the energy diagram, the standard boundary conditions for highly doped semiconductor-metal contacts are used for the gold-PEDOT contact (x = 0) by equating the Fermi levels:

$$E_{F,Au} = W_{AgCl} + eV_{app} = E_{F,p}(0) = k_bT\ ln(p(0))\ + eB + eV_p(0) \qquad 1.3.17$$

and by requiring charge neutrality in eq. 1.3.15:

$$p(0) - (-k_bT\ ln(p(0))/e\ - B + W_{AgCl}/e + V_{app} - V_c(0))C_V = 0 \qquad 1.3.18$$

where we isolated $V_p(0)$ from eq. 1.3.17 and we replaced it in eq. 1.3.15.
At the steady state, the hole concentration is constant throughout the film, and V_C in eq. 1.3.18 can be replaced by the Donnan potential. In fact, the polyelectrolyte/electrolyte interface acts as a semi-permeable membrane, which can be penetrated by the mobile ions provided by the electrolyte solution but cannot be crossed by the SO_3^- fixed anions of the PSS. This behaviour resembles the Donnan equilibrium in semipermeable membranes, [38] and is expressed by:

$$V_D = -\frac{RT}{F} arcsinh\left(\frac{c_{fix}}{2c_{\pm}}\right) \qquad 1.3.19$$

This yields eq. 1.3.20, which relates the applied voltage to the steady-state hole concentration:

$$V_{app} = p/C_V + k_bT\ ln(p)/e\ + B - W_{AgCl}/e + V_D \qquad 1.3.20$$

Tybrandt determined the unknown constant parameters C_V and B by fitting eq. 1.3.18 to measurement data. Potential steps of −50 mV (0.3 to −0.85 V) were used to plot the extracted charge versus time for different applied voltages (**Figure 1.3.9 a**). Assuming that the faradaic current is kinetically limited and only depends on the applied voltage, it can be subtracted as a linear contribution from the curves. This was performed by fitting the function $Q(t) = Q_{EDL}\left[1 - exp\left(-\frac{t}{\tau}\right)\right] + I_f \cdot t$, where Q_{EDL} constitutes the charge in the PEDOT:PSS. From this data, $p(V_{app})$ was calculated, and Eq. 1.3.18 was fitted, giving C_V = 19 F/cm^3 and B = 4.0 V (**Fig. 1.3.9 b**)

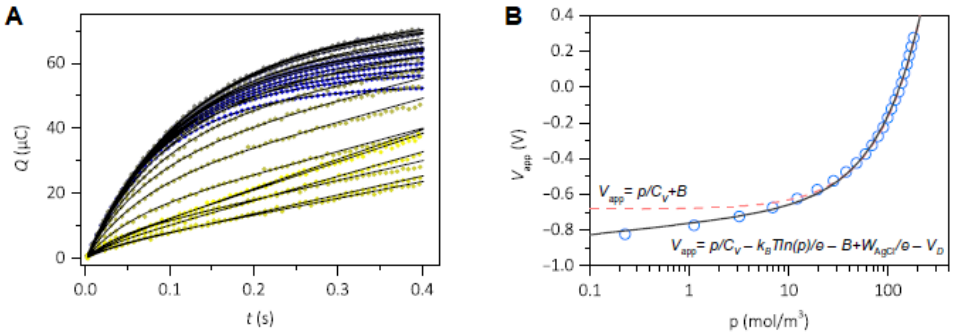

Figure 1.3.9: **a)** To measure the hole concentration dependence on the applied potential, Tybrandt stepped V_{app} from 0.3 V (blue circles) to −0.85 V (yellow circles) in 50-mV steps. **b)** The applied potential versus the measured hole concentration (○). Equation 1.4.18, which includes both the capacitive contribution of the EDL and the change in chemical potential, fits well (gray line). Purely capacitive model (red dashed line) deviates significantly at lower concentrations.

➢ **Modelling organic electrochemical transistors (OECTs):**

Tybrandt's drift-diffusion equations allow to model and simulate the behavior of organic electrochemical transistors (OECTs – see **sect. 1.2.7** and **fig. 1.2.14**). The typical OECT structure is reported in **Figure 1.3.10**. A conductive channel constituted by a PEDOT:PSS thin film is deposited between golden source and drain terminals. The source terminal is conventionally grounded. The Ag/AgCl gate electrode modulates the conductivity of PEDOT:PSS when a gate voltage (V_{gate}) is applied. The application of a drain voltage (V_{drain}) generates a current in the conductive channel.

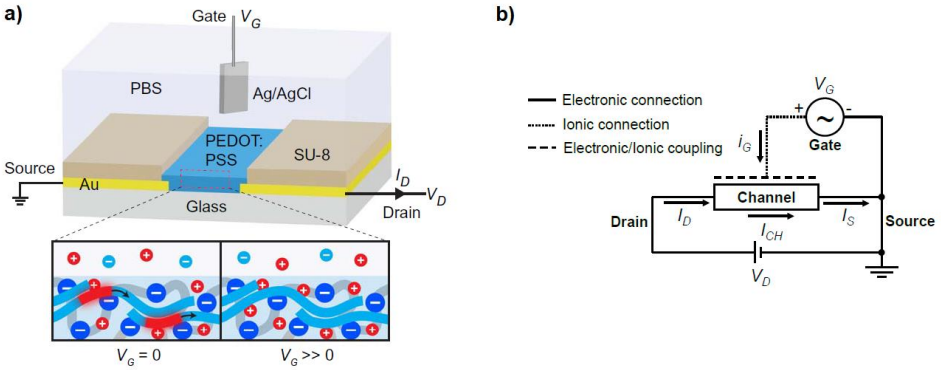

Figure 1.3.10: a) Structure of an organic electrochemical transistor (OECT) and **b)** equivalent circuit representation of the device

In static conditions, a net ionic current between the film and the electrolyte is absent ($I_{gate} = 0$). Consequently, the PEDOT phase is modelled by the drift-diffusion equations (1.3.11 and 1.3.13) and by Poisson's equation (1.3.13), which couples the charging of the PEDOT phase to the PSS phase by the electric double layer (EDL). For steady state, the potential in the PSS phase (V_C) can be approximated by the Donnan potential V_D. The full set of equation is expressed as

$$j_p = -D_p \left[\nabla p + \frac{F}{RT} p \nabla (V_p + \mu_p/e)\right] \qquad 1.3.21$$

$$\nabla \cdot j_p = 0 \qquad 1.3.22$$

$$-\frac{\varepsilon}{F}\nabla^2 V_p = p - C_V\,(V_p - V_D) \qquad 1.3.23$$

The boundary conditions at the source and drain terminals are derived from equating the electrochemical potentials on the two sides of the boundary and assuming zero space charge at the interface. By substituting the voltage applied on the transistor, eq. 1.3.18 for source contact can be written as

$$p(x_s) - (-k_b T\, ln(p(0))/e\ - B + W_{AgCl}/e - V_{gate} - V_D)C_V = 0 \qquad 1.3.24$$

and for drain contact as

$$p(x_d) - (-k_b T\, ln(p(0))/e\ - B + W_{AgCl}/e - V_{gate} + V_{drain} - V_D)C_V = 0 \qquad 1.3.25$$

The modeling equations are reported in the regions of the OECT where they are assumed to be valid in **Figure 1.3.11.**

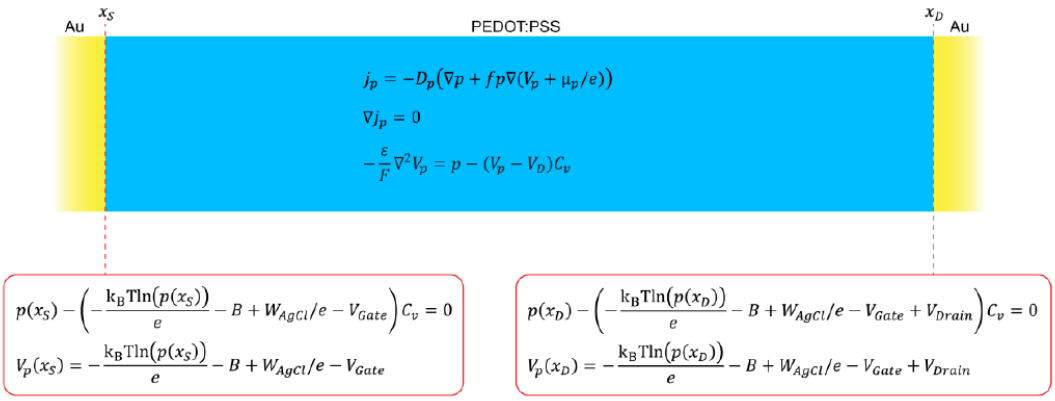

Figure 1.3.11: Drift-diffusion equations for charge transport in an OECT channel. In static conditions, there is no flux of charge between PEDOT:PSS and the electrolyte. Boundary conditions for the system are reported below.

Because the hole diffusion coefficient in CPs is known to increase with hole concentration, the first step is to determine the parameter $D_p(p)$ from measured small signal data, such as OECT transfer characteristics (drain current as a function of gate voltage, with fixed drain voltage). For small drain voltages, the drain current can be expressed as

$$I_{drain} = \frac{W}{L} t \cdot u_p \cdot p(x_{drain}) \cdot V_{drain} \qquad 1.3.26$$

where W, L and t are respectively length, width and thickness of the transistor channel, and u_p is the holes' mobility, which depends on D_p through Einstein's relation ($D_p = u_p k_b T/e$). The holes' concentration at drain contact can be calculated from boundary conditions in fig. 1.3.11, and eq. 1.3.26 can be numerically solved in u_p to obtain the corresponding mobility.

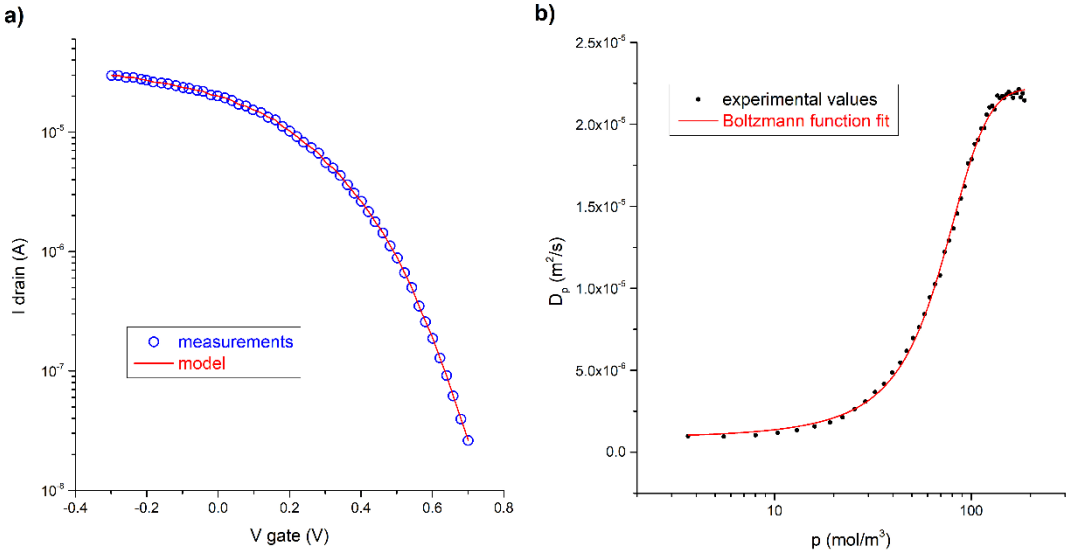

Figure 1.3.12: **a)** Eqs. in fig. 1.4.10 allow to reproduce OECT transfer curves (V_{drain} = -20 mV). Experimental data have been digitized from Tybrandt's article. **b)** Relation between hole diffusion coefficient and concentration.

The results of this analysis are reported in **fig. 1.3.12**, and reproduce the ones obtained in Tybrandt's work. The Boltzmann function resulted in a good fit for the $D_p(p)$ relation:

$$D_p(p) = D_{p,0}\left(1 - 1/\left(1 + exp\left(\frac{p - 69}{22}\right)\right)\right) \qquad 1.3.27$$

where $D_{p,0}$ = 2.3x10^{-5} m^2/s. This behavior is in agreement with theoretical and experimental studies [39] for organic materials with a Gaussian density of states.

➢ Modelling PEDOT:PSS electrodes:

By solving the full equation system (see **Figure 1.3.13 a**), the dynamics of PEDOT:PSS electrodes immersed in an electrolyte can be modeled. Tybrandt calculated static concentrations of the system for V_{app} = 0 and − 0.7 V (see **Figure 1.3.13 b**). The concentration of holes is strongly affected by the applied potential, whereas the relative change in ion concentrations is less pronounced, because the concentration of fixed counterions is much higher. In addition, the electrolyte/PSS potential is nearly identical in both cases.

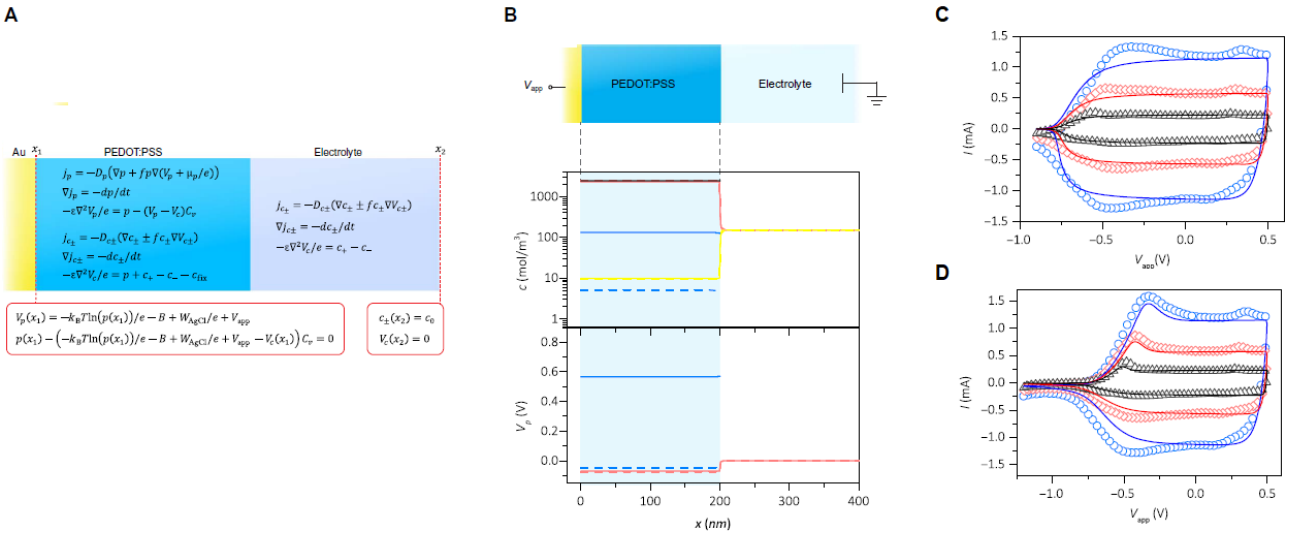

Figure 1.3.13: a) The drift-diffusion–Poisson's equations and boundary conditions for a CP-PE electrode. **b)**Potentials and concentrations for V_{app} = 0 V (solid lines) and −0.7 V (dashed lines). The hole concentration (blue lines) markedly changes with the applied voltage, whereas relative changes in the cation (red lines) and anion (yellow lines) concentrations are small due to the high concentration of fixed charges (black line). The electrostatic potential in the PEDOT phase (blue lines) changes a lot, whereas the potential in the PSS and electrolyte phases (red lines) is nearly constant. **c)** The main features of the measured cyclic voltammograms at different scan rates (○, 1.0 V/s; ◊, 0.5 V/s; and Δ, 0.2 V/s) are predicted by the model. **d)** By reducing the hole mobility, the commonly observed peaks in the forward scan direction can be reproduced.

In **fig. 1.3.13 c**, calculated and measured cyclic voltammograms at different scan rates for a 600-nm-thick PEDOT:PSS film are compared. The measured box-like shape with declining currents for negative potentials is reproduced, although there are some deviations for potentials <−0.5 V, probably due to faradaic side reactions. When the scan range is extended to −1.2 V, commonly observed peaks at −0.5 to −0.4 V in the forward scan direction emerge (**fig. 1.3.13 d**). Cyclic voltammograms of CP films are rich in features, that is, peaks and plateaus, which are typically difficult to decouple. The model offers explanations for three of these distinct features: (1) The box-like shape for higher potentials is due to the internal EDL within the material. (2) The gradual decrease in current for lower potentials is a consequence of changes in the chemical potential of the semiconductor. This is, in turn, caused by the tail of the gDOS. (3) The asymmetry of the backward and forward scans for low potentials is explained by slow hole transport (the mobility of holes is reduced by seven orders of magnitude). This manifests itself as a delay followed by a peak in the forward scan current. It seems that large negative potentials induce a permanent change, probably loss of conductivity, in the films.

Because this happens below the reduction potential of water, it might be caused by the generation of hydroxide ions, which are known to reduce the conductivity, although other mechanisms cannot be excluded.
Previous electrode characteristics implicitly probe the short-range vertical transport in the films. To explicitly probe the long-range lateral transport in the CP-PE blend, Tybrandt performed moving reduction front experiments. The device configuration is shown in **Figure 1.3.14 a.** At t = 0, a potential of −2 V is applied to the electrode. This creates an optically measurable electrochromic reduction front at the electrolyte side of the device. The model can be used to describe the behavior of the device as a function of time (0 to 45 s). The hole concentration starts to decrease at the electrolyte side and spreads with time into the film (**fig 1.3.14 b**). The electrostatic potential in the PEDOT phase initially goes from 0.57 to −1.33 V but does not change much from there on due to the low potential gradient necessary to transport the holes (Fig. 4C). However, the electrostatic potential in the ionic phase changes significantly throughout the process. One should notice that most of the potential drop occurs in the electrolyte in the close vicinity of the electrode. Because the ions are much slower than the holes, the reduction of PEDOT will start next to the electrolyte to minimize the length of the ion transport. Therefore, ion transport limits the rate of the process, and the electrolyte next to the CP-PE interface imposes a significant limitation on the current.

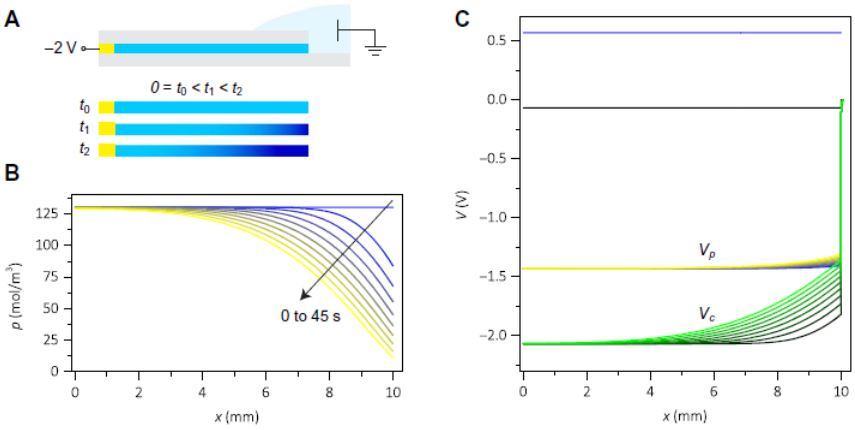

Figure 1.3.14: **a)** Moving front experiment setup: the encapsulated PEDOT:PSS film is electronically contacted to the left and ionically contacted to the right. At t = 0, the applied potential to the left is set to −2 V, which initiates the reduction of the film in contact with the electrolyte. The reduction front moves to the left with time and can be monitored optically. **b)** The calculated hole concentration versus time. **c)** The electrostatic potential in the PEDOT phase [V_p, 0 s (blue line) to 45 s (yellow line)] is quite flat due to the high mobility of the holes. The electrostatic potential in the PSS/electrolyte phase [V_c, 0 s (black line) to 45 s (green line)] varies more due to the slower ions. Most of the potential drop occurs in the electrolyte next to the film due to concentration polarization

1.4 Measuring mobility and charge carrier density in PEDOT:PSS

The charge transport characteristics of organic semiconductors are one of the key attributes that impacts the performance of organic electronic and optoelectronic devices in which they are utilized. For improved performance in organic photovoltaic cells, light-emitting diodes, and field-effect transistors (FETs), efficient transport of the charge carriers within the organic semiconductor is especially critical. Characterization of charge transport in these materials is important both from scientific and technological perspectives. [40] In particular, the charge carrier mobility is a key performance criteria. High-mobility values allow fast device operation as needed for low-cost electronics on large areas with performance meeting market demands. [6] Many techniques are known in literature for the characterization of charge transport in organic semiconductors, such as, space-charge-limited current (SCLC), time of flight (TOF), carrier extraction by linearly increasing voltage (CELIV), field effect transistors (FETs) measurements, and impedance spectroscopy (IS). Each technique has specific requirements about the nature of contacts for the injection/extraction of charge carriers . For example, SCLC requires one charge injection (ohmic) contact and one injection blocking contact. TOF and CELIV require both injection-blocking contacts, or one injection-blocking contact and one ohmic contact. FET requires both ohmic contacts. Generally, FETs are used to measure the charge carrier mobility in the film plane, whereas TOF, CELIV and IS are used to measure the charge carrier mobility perpendicular to the film plane. Not all these methods are suitable for a particular sample and the choice of the method depends on the details, such as sample thickness, nature of the electrodes, and the energy levels of the materials. [40]

In this work, a new method for the measurement of charge carrier mobility in PEDOT:PSS thin-films has been developed: the electrolyte-gated van der Pauw method (EgVDP). This technique is a 4-wire measurement, in which an opportunely shaped PEDOT:PSS thin film is immersed in an electrolyte and connected to the characterization setup through 4 contacts. A gate voltage controls the injection of ions from the electrolyte into film and modifies its conductivity. As in organic electrochemical transistor, when polarons extracted from the PEDOT phase are compensated by cations injected in the PSS phase, the carrier density in the conducting channel decreases. By analyzing the dependence between the film conductivity and the gate voltage, it is possible to extract the charge carrier mobility in PEDOT:PSS.
A detailed analysis of this method is provided in the following sections.

1.4.1 The Van der Pauw's method

Thin film transistors based on organic semiconductors are prone to contact problems that complicate the interpretation of their electrical characteristics and influence the extraction of important material parameters such as the charge carrier mobility. Mobility is conveniently extracted from thin film transistor (TFT) characteristics using the standard gradual channel approximation model [41]. Its value is directly representative of transistor operation and is a relevant parameter for device integration into circuits. In high-mobility organic semiconductors and in short channel devices, however, the relative importance of the contact resistance R_c can be such that the standard model is no longer appropriate for mobility extraction [42]. Proper parameter extraction is complicated by the fact that carrier injection from the contact into the semiconductor is often mediated by the gate voltage V_g. When this is not properly accounted, it leads to serious over-estimation of the mobility. Therefore, a more accurate, yet simple, method is highly desirable for the proper evaluation of μ_{tfsc}, the charge carrier mobility in thin films of organic semiconductors. In this definition, μ_{tfsc} characterizes the contact-independent translational motion of charge carriers across the thin film semiconductor material, over distances that may be larger than typical grain size. μ_{tfsc} encompasses extrinsic

barriers to transport such as grain boundaries, and therefore does not necessarily correspond to the intrinsic intra-grain charge carrier mobility of the monocrystalline semiconductor.

The van der Pauw (VDP) method is a geometry-independent four-contact electrical measurement widely used to characterize thin continuous films of semiconductor materials [43]. The four probes are placed around the perimeter of the sample, in contrast to the linear four point probe: this allows the van der Pauw method to provide an average resistivity of the sample, whereas a linear array provides the resistivity in the sensing direction [44]. As in four-point probe (FPP) measurements, the contacts that sense voltage are non-injecting, thereby limiting contact effects.
There are five conditions that must be satisfied to use this technique:

- The sample must have a flat shape of uniform thickness
- The sample must not have any isolated holes (its surface must be simply connected)
- The sample must be homogeneous and isotropic
- All four contacts must be located at the edges of the sample
- The area of contact of any individual contact should be at least an order of magnitude smaller than the area of the entire sample

From the measurements made, it is possible to calculate the sheet conductance σ_s of the material, its doping type, the sheet carrier density of the majority carrier (the number of majority carriers per unit area) and their mobility μ_{tfsc}.

The van der Pauw method is based on the van der Pauw's theorem [43]. Let us consider a flat sample of a conducting material of arbitrary shape (which fulfills the above-mentioned conditions) with successive contacts A, B, C and D fixed on arbitrary places along its perimeter. We define the resistance $R_{AB,CD} \equiv (V_D - V_C)/I_{AB}$. $R_{AB,CD}$ represents the potential difference $V_D - V_C$ between the contacts D and C when a unit current enters the sample through the contact A and leaves it through the contact B. Similarly, we define the resistance $R_{BC,DA}$. It is possible to demonstrate that the following relation holds:

$$exp\left(-\frac{\pi R_{AB,CD}}{R_S}\right) + exp\left(-\frac{\pi R_{BC,DA}}{R_S}\right) = 1 \qquad 1.4.1$$

where $R_S = 1/\sigma_s$ is the sheet resistance, defined as the ratio between the sample resistivity and its (uniform) thickness. R_S is typically measured in Ω/sq, which indicates that a square sheet with R_S = 1 Ω/sq has an actual resistance of 1 Ω, regardless of the size of the square.
Eq. 1.4.1 implies that for measuring the sheet resistance of a flat sample it suffices to make four small contacts along its circumference and to measure the two resistances $R_{AB,CD}$ and $R_{BC,DA}$. In order to facilitate the solution of R_S from Eq. 1.4.1, we write it in the form

$$R_S = \frac{\pi}{ln(2)} \frac{(R_{AB,CD} + R_{BC,DA})}{2} f\left(\frac{R_{AB,CD}}{R_{BC,DA}}\right) \qquad 1.4.2$$

where f is a function of the ratio between $R_{AB,CD}$ and $R_{BC,DA}$ only and satisfies

$$\frac{R_{AB,CD} - R_{BC,DA}}{R_{AB,CD} + R_{BC,DA}} = \frac{f}{ln2}\, arccosh\left[\frac{exp\,(ln2/f)}{2}\right] \qquad \text{X-2} \qquad 1.4.3$$

If $R_{AB,CD}$ and $R_{BC,DA}$ are almost equal, f can be approximated with

$$f \approx 1 - \left(\frac{R_{AB,CD} - R_{BC,DA}}{R_{AB,CD} + R_{BC,DA}}\right)^2 \frac{ln(2)}{2} - \left(\frac{R_{AB,CD} - R_{BC,DA}}{R_{AB,CD} + R_{BC,DA}}\right)^4 \left[\frac{(ln\ 2)^2}{4} - \frac{(ln\ 2)^3}{12}\right] \qquad 1.4.4$$

The function f used for determining the sheet resistance of the sample is plotted as a function of $R_{AB,CD}/R_{BC,DA}$ in **Figure 1.4.1**, where it is compared with its approximation given in eq. 1.4.4.

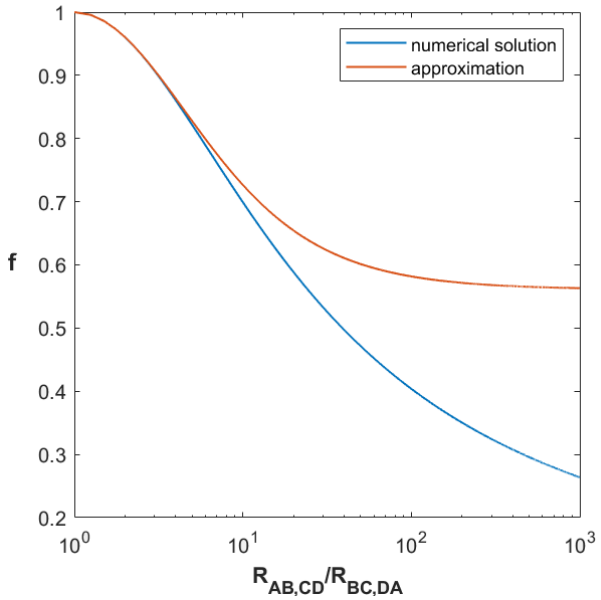

Figure 1.4.1: The function *f* used for determining the sheet resistance of the sample, plotted as a function of $R_{AB,CD}/R_{BC,DA}$. The graph has been obtained by numerically solving eq. 1.4.3. The result is compared with the approximation given in eq. 1.4.4.

If the contacts are of finite size and not at the edges of the sample, a placement error ΔR_S affects the sheet resistance measurements. Van der Pauw derived an approximated correction formula for circular disc shaped sample, with contacts spaced at angles of 90°. W. Koon [45] deepened this particular aspect and offered a more complete overview on the effect of the contact size and placement on the sample. Its main results are reported in **Table 1.4.1**.

Desired accuracy	circular shape (d/D)	circular cloverleaf shape (d/D)	square shape (d/D)
$\Delta R_S/R_S < 1\%$	0.059	0.26	0.19
$\Delta R_S/R_S < 0.1\%$	0.019	0.083	0.10

Table 1.4.2: Maximum permissible values for the displacement *d* of the four contacts for a square, a circle and a circular cloverleaf shaped sample. D indicates respectively the diameter of the circle (and of the circular cloverleaf) and the side of the square.

In a later work [46], Koon performed Van der Pauw resistivity measurements on samples of six different shapes: circle, square, two circular cloverleafs, and two square cloverleafs. The measurement error of the resistivity due to contact displacement was determined. The square

shapes gave contact placement errors typically 10–100 times smaller than the errors in the corresponding circular shapes. All cloverleafs gave smaller errors than the corresponding non-clovered shapes. Consequently, the square cloverleaf is the sample geometry on which the non-ideal contact positioning has the lower effect. An example of Koon's analysis is reported in **Figure 1.4.2**:

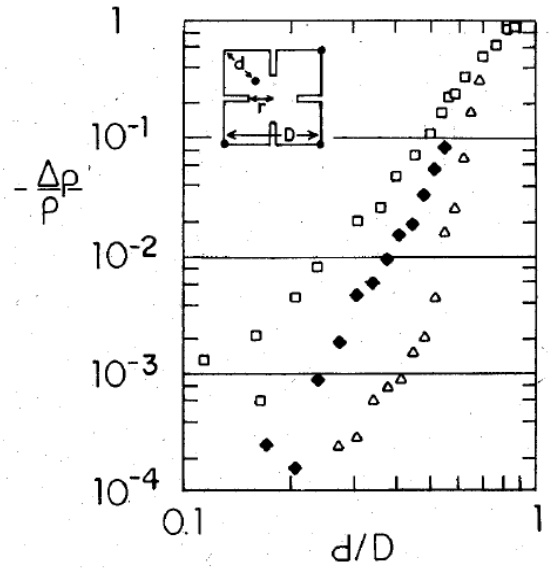

Figure 1.4.2*:* Relative measurement error in the resistivity for square (square symbol) and square cloverleafs with r = D/4 (diamonds) and r = D/8 (triangles), given a contact lead misplacement d from the edge. Dimensions of the samples and of the lead misplacement are shown in inset.

1.4.2 The gated van der Pauw's method for thin film characterization

In 2017, Rolin et al. [6] developed the gated van der Pauw (gVDP) method for the characterization of thin films of organic semiconductors. Scientists showed that a gate contact can be used to modulate the charge carrier density in a VDP device, and that a gated structure creates transport conditions similar to thin film transistor (TFT) operation. Moreover, they developed a simple model for the interpretation of gVDP characteristics, allowing for an extraction of mobility and threshold voltage V_t.

Rolin used a simple VDP device topology, as presented in **Figure 1.4.3 a**. [6] The thin conductive film is patterned as a square and four contacts are applied to its corners. As seen in the previous section, the size of the contacts must be negligible relative to the size of the square, but this condition is relaxed when using clover-leaf shaped films, which simplifies alignment of the patterned layers. For electrical measurement, a current I_1 is sourced in contact 1 and drained at contact 2, which is grounded and used as a reference. The potentials V_3 and V_4 in isolated contacts 3 and 4 are measured. The potential distribution and current density streamlines in a square VDP device are obtained from a two-dimensional finite element analysis solving Maxwell's equations with realistic σ_s = 1.5 μS per square and I_1 = 1 mA (**Figure 1.4.3 c**). The current density is highest along the edge 1–2 and decreases towards side 3–4 as the current path lengthens. The dashed equipotential lines V_3 and V_4 delimit the probed region where the voltage is sensed, away from the source and drain contacts 1 and 2.

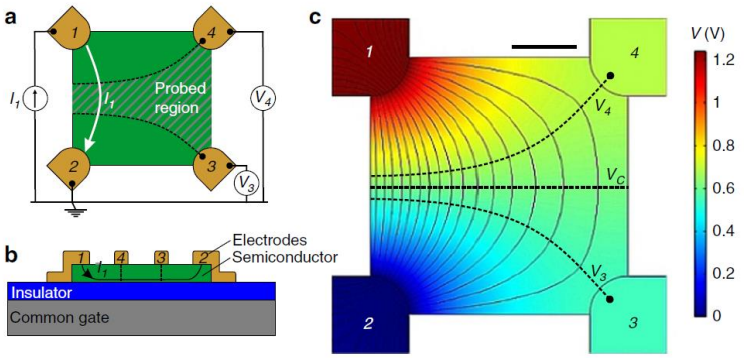

Figure 1.4.3: The gated van der Pauw method. **(a)** Top view of a van der Pauw device with square-shaped thin semiconductor film. **(b)** Pseudo-cross-section view of a van der Pauw device fabricated on a common gate and insulator. All contacts are projected on the same plane for convenience. **(c)** Potential map and current density streamlines in the van der Pauw device in linear regime. The scale bar is 0.5mm long. The simulation is parameterized with a current I_1 = 1 mA flowing through a film with sheet conductance σ_s = 1.5 μS/sq. The dashed lines are equipotential lines V_3,V_4 and $V_C = (V_3 + V_4)/2$.

The resistance in the probed region alongside contacts 1-2 ($R_{12,34} = |V_4 - V_3|/I_1$) is initially measured. The measurement of $R_{12,34}$ along the same side is obtained by reversing the direction of the current while grounding contact 1. Next, the resistances along the three other sides of the square are measured in a similar way, and the eight resistance values are averaged as <R>. Finally, Rolin calculated the sheet conductance of the film as

$$\sigma_S = \frac{ln(2)}{\pi\langle R\rangle} \qquad 1.4.5$$

Eq. 1.4.5 only approximates eq.1.4.1, and the two coincide only if $R_{AB,CD} \equiv R_{12,34}$ is equal to $R_{BC,DA} \equiv R_{23,41}$. In that case the value assumed by the *f* function in eq. 1.4.4 is simply 1. Such a condition is achieved only in perfectly homogeneous and isotropic samples. When eq. 1.4.5 is applied, we implicitly assume that we are characterizing an ideal device, but its resistance <R> is the result of the averaging on a real device. As a consequence, the entity of this approximation increases with the inhomogeneity of the sample.

It is possible to identify different strengths of the VDP method. As in four-point probe (FPP) measurements, the contacts that sense voltage are non-injecting, thereby limiting contact effects. Furthermore, contrarily to the FPP method, no geometrical dimension enters VDP data analysis: device imperfections and misalignments are averaged out by measuring all four sides in both directions.

Rolin introduced a common gate by fabricating the VDP device on a highly doped silicon wafer covered with a thin layer of SiO_2 as gate dielectric. A gVDP device cross-section is shown in **fig. 1.4.3 b**, where all contacts are projected on the same plane for convenience. Applying a potential V_g to the gate relative to the grounded contact 2 leads to the accumulation of charges at the semiconductor/insulator interface. This results in an increase of σ_s that promotes current flow. The relationship between σ_s and V_g is explained by a model derived from the TFT generic charge drift model given by: [47]

$$I_D \frac{L}{W} = \sigma_{tft}(V_D - V_s) = \mu_{tfsc} C_I \frac{(V_g - V_t - V_S)^{\gamma+2} - (V_g - V_t - V_d)^{\gamma+2}}{\gamma + 2} \qquad 1.4.6$$

Where σ_{tft} and I_D are the TFT conductivity and drain current, L and W are the channel length and width, V_s and V_d are the potential at the source and drain contacts, C_I is the gate insulator

capacitance per unit area and γ is the mobility enhancement factor. γ needs to be included when mobility depends on gate voltage, which is a consequence of trapping: trap states decrease the number of charge carriers collected by the gate voltage and available for conduction. [48] To model gVDP operation with equation 1, we can simply treat the probed region in the VDP device as a TFT with source and drain at potentials V_4 and V_3 respectively, and with geometrical dimensions L/W = ln(2)/π, as resulting from the approximation made in eq. 1.4.5 (being 1/<R> the TFT channel conductivity σ_{tft}). Assuming that μ_{tfsc} is unaffected by potential variation, that is γ=0, the generic TFT model is rewritten as:

$$I_D \frac{ln(2)}{\pi} = \sigma_S |V_4 - V_3| = \frac{\mu_{tfsc} C_I}{2} \left[\left(V_g - V_t - V_4\right)^2 - \left(V_g - V_t - V_3\right)^2 \right] \qquad 1.4.7$$

and, after simplification

$$\sigma_S = \mu_{tfsc} C_I |V_g - V_t - V_C| \qquad 1.4.8$$

with $V_C = |V3 + V4|/2$.
In the parallel plate capacitor formed by the gate/insulator/semiconductor stack, the charge density is $\delta = C_I |V_g - V_t - V_C|$, where V_C approximates the potential in the probed region of the gVDP device. Equation 1.4.8 is very similar to the gradual channel approximation model of a TFT in the linear regime, that is derived from equation 1.4.6 with V_S =0 and γ=0

$$\sigma_{tft} = \frac{I_D}{V_D} \cdot \frac{L}{W} \mu_{app} C_I \left| V_g - V_t - \frac{V_D}{2} \right| \qquad 1.4.9$$

Here, $V_D/2$ approximates the potential in the TFT channel and μ_{app} is the apparent mobility, which, in contrast to μ_{tfsc}, is affected by the contact resistance.

gVDP electrical characterization requires a current source to control I_1. The bias on contact 1, V_1, is automatically adjusted to keep a constant current, while sweeping the gate voltage V_g. Furthermore, the gVDP device is best measured when the grounded electrode 2 is also the contact that sinks charge carriers, as shown in **fig. 1.4.3a**. Therefore, for p-type (n-type) semiconductors, holes (electrons) are injected by the positively (negatively) biased contact 1, resulting in a positive (negative) current I_1 flowing from 1 to 2. **Figure 1.4.4 a** shows the evolution of V_1 as a function of V_g for a broad series of I_1, for the p-type organic semiconductor C10-DNTT (2,9-didecyl-dinaphtho-[2,3-b:20,30;-f]-thieno-[3,2-b]-thiophene) with gold contacts. [6] It is possible to distinguish two operating regimes from the shape of the V_1 curves. At high (positive) V_g, V_1 has a linear dependence with V_g with a slope equal to unity. At low (negative) V_g, $|V_1|$ is small and slowly decreases as $|V_g|$ increases. These regimes are respectively called saturation and linear regimes, as they correspond to the eponymous regimes observed in TFT operation. The two regimes are also apparent in **fig. 1.4.4 b**, where V_1, V_C and V_4–V_3 are detailed for I_1 =2 μA. In the saturation regime, V_C follows V_1 very closely, while V_4–V_3 takes a small constant value of 0.19 V. In saturation, the majority of the semiconductor film is subjected to a limited potential drop. Its average potential V_C is close to V_1. In this almost equipotential region, V_1 (hence V_C) automatically adjusts to a value substantially higher than V_g so that the charge density $\delta_{sat} = C_I |V_g - V_t - V_C|$ remains constant at a value allowing current flow. In contrast, the vicinity of grounded contact 2 is depleted of charge carriers. A potential drop through the semiconductor film, from ~V_C to V_2 =0 V, creates a lateral field sufficient to maintain current through this depletion zone. In the linear regime, **fig. 1.4.4 b** shows that V_C is exactly the half of the small V_1. In this case, as represented in the simulation of **fig. 1.4.3 c**, the potential linearly drops when current flows from contact 1 to 2. The transition between regimes

is most visible in the V_4–V_3 curve in **fig. 1.4.4 b**. It takes place at $V_g \sim V_t$ corresponding to the closure of the depletion zone around contact 2. Further V_g decrease into the linear region yields an increase in charge carrier density so that $\delta_{lin} > \delta_{sat} = \text{const}$. The increase of δ_{lin} is compensated by the progressive lowering of the lateral electric field (seen in the decrease of V_1 and V_4–V_3). This maintains a constant current I_1 throughout the linear regime.
After averaging the eight measurements with the procedure previously illustrated, Rolin extracted the sheet conductance of the semiconductor film σ_s using the VDP method for various V_g and I_1. Following equation 3, σ_s is plotted as a function of V_g–V_C in **fig. 1.4.4c**. With this choice of the x-axis, all characteristics fall along the same straight line. **Fig. 1.4.4c** has been linearly fitted using equation 1.4.8. Its slope and intercept with the x-axis give μ_{tfsc}=(6.5±0.1) $cm^2V^{-1}\ s^{-1}$ and V_t =(6.5±0.2) V, respectively. The straightness of the curve in **fig. 1.4.4c** confirms that μ_{tfsc} has negligible field dependence (γ = 0). Moreover, the small error bars in **fig. 1.4.4c**, and the limited standard errors in the extracted data show that the gVDP approach effectively reduces error and increases precision. Finally, the two regimes observed earlier, do not appear in the evolution of σ_s with V_g –V_C. Indeed, σ_s is extracted from the probed region between equipotentials V_3 and V4 drawn in **fig 1.4.3 a**. Since this region remains far from the depletion zone in the vicinity of grounded contact 2, it always experiences a linear current transport, even when the gVDP device is driven in saturation. In consequence, the extraction of σ_s is independent of the regime of operation and data can be collected across a broad V_g range.

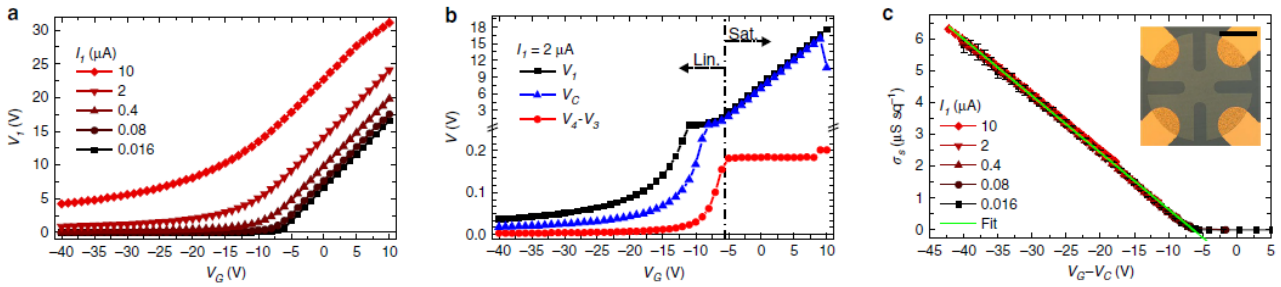

Figure 1.4.4: **(a)** Potential V_1 of the injecting contact 1 as a function of gate voltage V_g for different currents I_1. **(b)** Evolution with V_g of three characteristic potentials V_1, V_C and V_4–V_3. Data measured with I_1 = 2 μA. **(c)** Sheet conductance σ_s of the semiconductor film extracted using the gVDP method at different I_1. σ_s is plotted as a function of V_g–V_C. The error bars are computed by averaging over 8 measurements, 2 along each side of the gVDP structure. The line is linear fit. Inset: photograph of the gVDP device based on a thin film of C10-DNTT shaped as a clover-leaf. Scale bar is 0.5mm long.

TFTs with different L are plotted in Fig. 3a as a function of V_g-V_d/2, along with the σ_s obtained from the gVDP device. The TFT curves in **fig. 1.4.5 a** show a slight hysteresis with the back and forth sweep of V_g, especially for the short channel devices. gVDP devices usually display the same level of hysteresis as long channel TFTs. In the case of the C_{10}-DNTT gVDP device discussed so far, this hysteresis is negligible. The lines in **fig. 1.4.5 a** are linear fits using equation 1.4.9 that deliver the apparent mobility and threshold voltage of the TFTs. Rolin used this approach to extract μ_{app} and V_t of all 10 TFTs in the TLM structure. These are reported in **fig. 1.4.5 b** as a function of L. As L increases, the TFT sheet conductance curve in **fig. 1.4.5 a** shifts towards the gVDP curve. This progression also appears in **fig. 1.4.5 b**, where μ_{app} tends towards μ_{tfsc} with the increase of L. This can be formalized using the following relation: [49]

$$\mu_{app} = \frac{\mu_{tfsc}}{1 + \frac{L_{1/2}}{L}} \qquad 1.4.10$$

where $L_{1/2}$ is the channel length at which the contact resistance R_c is equal to the channel resistance R_{ch}.

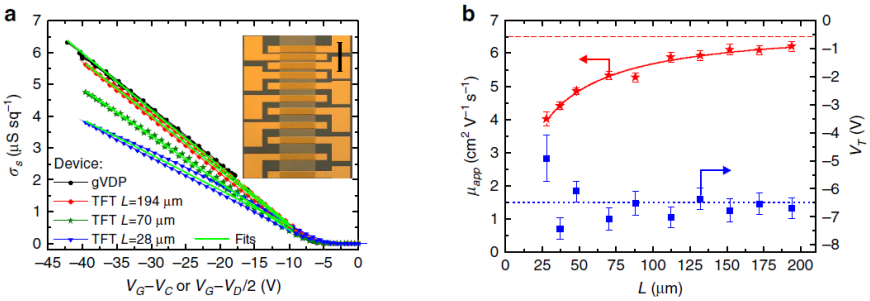

Figure 1.4.5: Comparison with TFT characteristics. **(a)** Sheet conductance σ_s of the semiconductor thin film measured from a gVDP device and three TFTs with different channel lengths taken from a TLM device. Lines are linear fits delivering the apparent mobility μ_{app} and the threshold voltage V_t of the TFTs. Inset: photograph of the TLM structure with a thin C_{10}-DNTT film and Au top contacts. Scale bar is 0.5mm. **(b)** Evolution of μ_{app} and V_t with TFT channel length. μ_{app}, Vt and the error bars are obtained from the linear regression on the σ_s versus V_g–$V_d/2$ characteristic of each TFT, as shown for three values of L in (a). The line is a fit to the μ_{app} data (with eq. 1.4.10). The dashed and dotted horizontal lines respectively represent the μ_{tfsc} and V_t from the corresponding gVDP device.

By applying the standard TLM analysis, the variation of the total device resistance R_{tot} with L can be expressed as: [49]

$$R_{tot}W = R_cW + \frac{L}{\mu_{tfsc}C_I|V_g - V_t|} \qquad 1.4.11$$

This procedure yields μ_{tfsc} from the slope of the fit and R_cW from its intercept with the y-axis. This μ_{tfsc} exactly matches the value obtained from the fitting of μ_{app} in **fig. 1.4.5 b**. It is also within the error of the μ_{tfsc} measured in the gVDP device. R_cW has a low value for organic TFTs that is characteristic of this material set. TFT characteristics are nevertheless still seriously impacted by R_c because of the high-mobility, hence low R_{ch}, of the C10-DNTT film. The gVDP device, on the other hand, shows an ideal behavior and its characteristic in **fig. 1.4.5 a** represents the optimum towards which TFTs tend as the effect of R_c abates.

1.4.3 Electrolyte-gated van der Pauw's method

The gated van der Pauw method discussed in the previous section combines the following advantages: (1) Device structure and fabrication constraints are the same as for thin film transistors, allowing easy device integration and comparison. (2) Independence from contact effects that are detrimental to transistor characteristics. (3) Straightforward data analysis using eq. 1.4.8 and precise parameter extraction thanks to the inherent averaging and independence from geometrical dimensions.

The electrolyte-gated van der Pauw's method (EgVDP) aims to combine the advantages of gVDP characterization with the coupled electronic-ionic conductivity of CP-PE blends to determine the charge carrier mobility in PEDOT:PSS thin films. As in gVDP measurements, a PEDOT:PSS thin film is patterned as a square and four contacts are applied to its corners. The size of the contacts must be negligible relative to the side of the square. The film is immersed into an electrolyte, and a gate voltage is applied between the electrolyte and the low-voltage sensing contact of the device (contact 3 in **fig. 1.4.3**). The gate voltage controls the injection of ions from the electrolyte into film and modifies its conductivity. As in organic electrochemical transistor, when polarons extracted from the PEDOT phase are compensated by cations injected in the PSS phase, the carrier density in the conducting channel decreases. By analyzing the dependence

between the film conductivity and the gate voltage, eq. 1.4.8 allows to extract the charge carrier mobility in PEDOT:PSS.

CHAPTER 2: METHODS

2.1 Fabrication methods for EgVDP characterization

The electrolyte-gated van der Pauw's characterization of PEDOT:PSS thin films requires specifically patterned samples. In this work, such devices have been realized with two different approaches. In the first fabrication run, millimeter-sized samples were patterned by manually scratching a spin coated PEDOT:PSS thin film. Experimental limitations resulting from the large electrical capacitance of the samples suggested us to fabricate miniaturized devices, with a smaller film area. Therefore, in the second fabrication run we realized EgVDP devices with microfabrication techniques.
The design and fabrication processes of both approaches are presented in this section.

2.1.1 Design of EgVDP devices

As discussed in section 1.4.1, choosing the opportune sample geometry for van der Pauw's characterization is crucial to minimize contacts displacement errors, which unavoidably affect non-ideal measurements. In particular, Koon's work [45] indicated the square and the square-cloverleaf shapes as the best geometries to reduce the impact of contact displacements. For this reason, in the first fabrication run we patterned the PEDOT:PSS thin film with a square-cloverleaf shape, and we designed four symmetric contacts with dimensions as small as possible. The devices' design is reported in **Figure 2.1.1**. Metallic contacts were realized by applying conductive silver paste directly on the film.

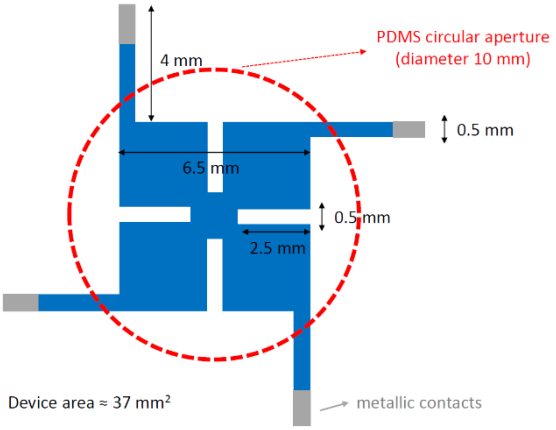

Figure 2.1.1: Design of millimeter-sized EgVDP devices, realized in the first fabrication run. The sample dimensions are indicated on the figure. PEDOT:PSS thin film is represented in blue, metallic contacts in grey. The red circle represents the sample's surface placed in direct contact with the electrolyte, corresponding to the area of the aperture of the covering PDMS film.

During EgVDP characterization, devices are immersed in an electrolyte. The direct contact between silver and the electrolyte introduces redox charge transfers, which must be avoided. For this reason, we covered each device with a PDMS film, cutting a small circular aperture in correspondence to the sample center, where the PEDOT:PSS film was patterned. Only a small portion of the sample surface was placed in direct contact with the solution, namely the inner part of the red circle in Fig. 2.1.1. The PDMS film limits the region where the ion exchange between PEDOT:PSS and the electrolyte occurs. Consequently, the intersections between the

circumference of the PDMS aperture and the PEDOT:PSS film can be considered as contacts for the ion injection (gating contacts), and their dimensions must be minimized. For this reason, metallic contacts are connected with the cloverleaf edges through thin PEDOT:PSS tracks (width 0.5 mm), where the intersection between PEDOT:PSS and PDMS films occur. In this way, the dimension of the gating contacts is limited by the (small) tracks' width.

Miniaturization has revealed to be a relevant aspect for EgVDP devices. In fact, the electrical capacitance of a PEDOT:PSS thin film depends on its volume and, consequently, on the film area. Large capacitance values increase the time constant of the circuit $\tau \approx C_{film} \cdot R_{ch}$, where R_{ch} is the channel resistance, i.e. the electrical resistance between two contacts on the thin film. For high gate voltages, the ion injection into the PEDOT:PSS film reduces its conductivity and, consequently, increases R_{ch} and τ. For large/high C_{film} value, the capacitive charging/discharging requires a long time, which is not compatible with a reasonable scan rate on the gate voltage. Devices with large film area can be used only at low gate voltages, when the concentration of holes in PEDOT is higher. Since this work aims to study low-concentration regimes of PEDOT:PSS films, we fabricated miniaturized devices.
The design of miniaturized EgVDP samples is reported in **Figure 2.1.2 a**. A 500 µm x 500 µm PEDOT:PSS square film is placed at the centre of each device. Samples are connected to the characterization setup throughout 4 gold contacts, made by thin tracks (width 50 µm) starting from the film edges and ending into large rectangular pads (1 mm x 3 mm each).

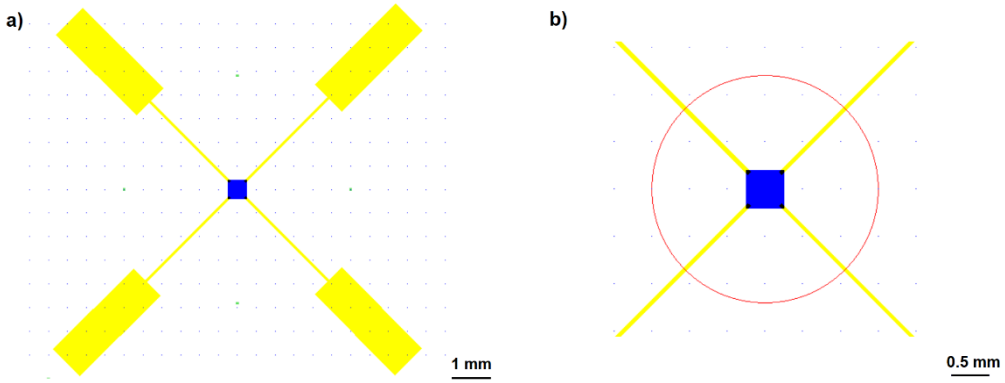

Figure 2.1.2: a) Design of miniaturized EgVDP devices. The scale bar is 1 mm. PEDOT:PSS thin film is represented in blue, metallic contacts in yellow. **b)** Focus on the sample centre. The red circle represents the sample's surface placed in direct contact with the electrolyte, corresponding to the area of the aperture of the covering PDMS film.

In miniaturized devices, the direct contact between gold and the electrolyte introduces an external parasitic capacitance, which should be minimized. The already-mentioned PDMS film was applied for this scope. Only a small portion of the sample surface was placed in direct contact with the solution, namely the inner part of the red circle in **Figure 2.1.2 b,** with diameter 3 mm. Smaller diameters were initially adopted in measurements, but these leaded to the formation of a water meniscus in correspondence to the aperture, whose upper part was filled only by air. The presence of an air bubble prevented the direct contact between the PEDOT:PSS film and the electrolyte, making ion injection impossible. Finally, no gating contacts were present in the miniaturized devices, because PEDOT:PSS film was completely immersed in the electrolyte.

In parallel with the fabrication of the EgVDP devices, miniaturized two-contact devices were realized to analyze the impact of contact resistance on measurements. Their design is reported in **Figure 2.1.3**. As in four contact samples, a 500 µm x 500 µm PEDOT:PSS square film is placed at the center of each device and contacted through 2 gold contacts, made by thin tracks (width 50 µm) and large rectangular pads (1 mm x 3 mm each).

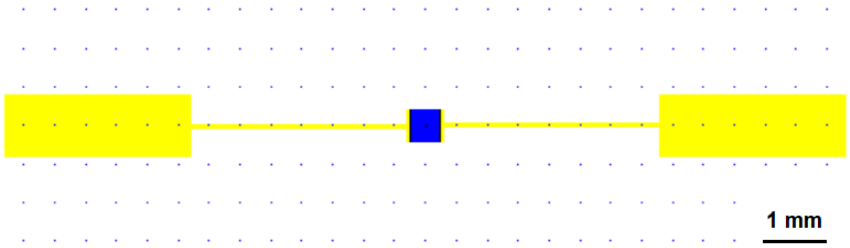

Figure 2.1.3: Design of 2-contacts miniaturized samples.

2.1.2 Fabrication of miniaturized EgVDP devices:

Fabrication of miniaturized EgVDP samples is divided in different steps, which are reported in the following list. A general overview of the process is presented in **Figure 2.1.4**.

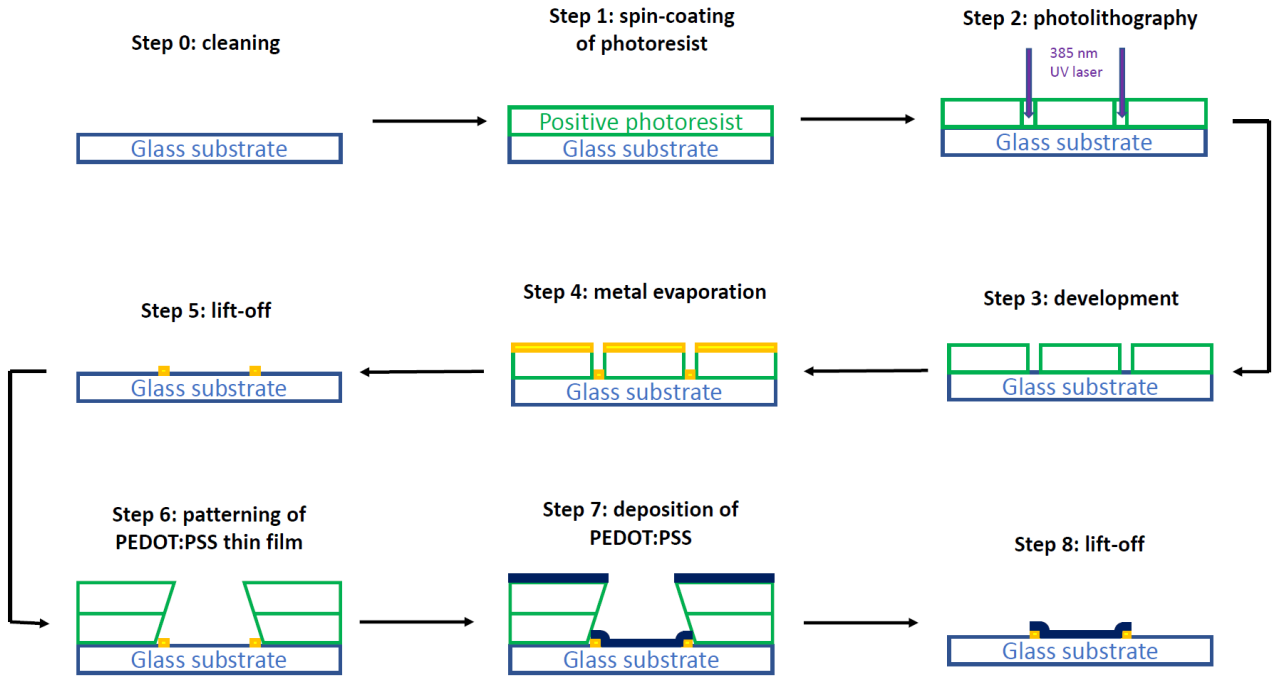

Figure 2.1.4: Microfabrication process for the EgVDP devices. Each step is discussed in detail in the list below.

- **Step 0: glass substrate cleaning:**

We fabricated EgVDP devices on glass substrates, constituted by microscope slides with dimensions 2.5x2.5 cm. The cleaning procedure of the substrates was performed in 4 steps: initially glass slides were immersed in an ultrasonic bath with soap and water (1/10 volume-volume ratio) for 10 minutes, and then rinsed with distilled water. The same procedure was repeated by dipping substrates in distilled water, acetone, and isopropanol. Finally, a nitrogen flow was used to blow-dry the slides, followed by a dehydration step: the adsorbed water on the surface of the substrates was removed by placing them on a hot plate at 110°C for 5 min. This passage also improves the photoresist adhesion. After a 30 seconds cooling, substrates were ready for the following step.

- **Step 1: spin coating of positive photoresist:**

MicroChem S1818 positive photoresist was spin-coated on the glass substrates, using 450 µL of S1818 for each 2.5x2.5 cm slide. Spin-coating was performed at 4000 rpm. This angular velocity was reached in t_{ramp} = 1 s (4000 rpm/s acceleration), and maintained for t_{dwell} = 60 s. After spin-coating, substrates were annealed on a hot plate at 110°C for 1 min.

- **Step 2: photolithography of metallic contacts:**

Microlithography of metallic contacts was performed by using ML3 MicroWriter from Durham Magneto Optics. ML3 is a direct-write photolithography machine. Conventional approaches to photolithography are usually based on exposing through a chromium-glass mask manufactured by specialist vendors. In research environments it is often necessary to change the mask design frequently. Direct-write lithography tools (also known as digital mask aligners or maskless aligners) overcome this problem by holding the mask in software. Rather than projecting light through a physical mask, direct-write lithography uses computer-controlled optics to project the exposure pattern directly onto the photoresist. Patterns were drawn with CleWin 4 software and loaded on the microwriter controlling software. ML3 microwriter uses a 385nm light source able to go down to 1 µm resolution. During EgVDP fabrication, the light exposition on the photoresist was set to 260 mJ/cm^2.

- **Step 3: photoresist development:**

After microlithography, samples were immersed and moved gently in a beaker containing Microposit MF-319 developer for 45 s. Then, the same procedure was repeated in distilled water. As S1818 is a positive photoresist, the regions of the photoresist layer which had been exposed to the microwriter light became soluble to the developer and were removed during this procedure. Finally, samples were blow-dried with N_2 flow.

- **Step 4: metal evaporation:**

(20 ± 4) mg of chromium and (170 ± 4) mg of 99.9% pure gold were used for evaporation. The metallic filaments were washed in an ultrasonic bath with acetone, isopropanol and distilled water, and sonicated for 10 minutes in each step. Then, they were placed on two different tungsten filaments inside an evaporation chamber. The double heat source of the evaporator allowed the sequential deposition of the two metals. In fact, chromium is deposited before gold because it has better adhesion on slides and is used as a precursor. By activating a rotary pump and a molecular pump, the pressure inside the chamber was lowered to about 10^{-6} torr. Thereafter, the power of the evaporator was gradually increased to heat the crucible by increasing the current intensity flowing in the tungsten filaments. In particular, the power delivery has been increased by 5% every 30-40 seconds to avoid breakage of the filaments. Since impurities evaporate at lower temperatures than those of chromium and gold, to avoid contamination the slides were covered by an appropriate protection (called shutter) until the apparatus reached high temperatures. At that point, the shutter was removed, and the sequential deposition of the metals took place until their complete evaporation. Subsequently, the power delivered by the evaporator was gradually reduced until the device was switched off. On average, a 10 nm thick layer of chromium and above it a 60 nm thick layer of gold were deposited on each sample.

➢ **Step 5: photoresist lift-off:**

Samples were placed in a container filled with acetone for 4 hours. Then, the container was sonicated for 10 s. During lift-off, acetone dissolved the photoresist and, consequently, it removed all the metallic layer which had been evaporated onto it. Samples were then immersed in a new container with fresh acetone and sonicated for 10 s to remove all remaining resist. This procedure was repeated in isopropanol and distilled water. Finally, samples were blow-dried with nitrogen flow.

➢ **Step 6: patterning of the PEDOT:PSS thin film**:

Step 1 was repeated twice to deposit a double layer of photoresist (**Figure 2.1.5 a**). The sample surface was treated for 6 minutes with chlorobenzene, which hardens the external photoresist layer. [50] Then, photolithography and development were performed by repeating steps 2 and 3. Because of the double layer of photoresist, the exposition rate during photolithography was set to 580 mJ/cm^2. After these passages, we expect the irradiated region of the surface to have a trapezoidal structure (see **Figure 2.1.5 b**), because the internal layer of photoresist was more sensitive to the light exposure and was more erased with respect to the external one. This structure can be exploited to reduce the broadening of the PEDOT:PSS pattern. In fact, once the film is deposited, PEDOT:PSS chains tend to crosslink between the developed and not-developed regions of the sample surface (see **Figure 2.1.5 c**), increasing the film broadening after the photoresist lift-off. The trapezoidal structure in Figure 2.1.4 b should reduce the (vertical) crosslinking, giving to the film a less broadened boundary.

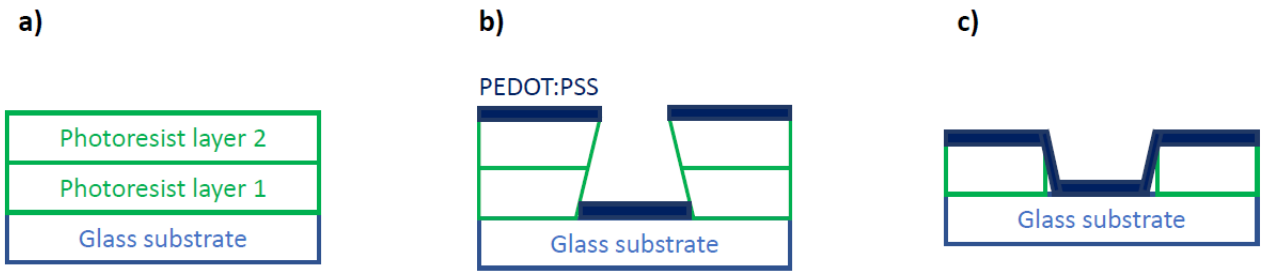

Figure 2.1.5: a) Double photoresist layer for PEDOT:PSS thin film patterning. **b)** Sample structure after microlithography, development and PEDOT:PSS deposition. The trapezoidal arrangement of the two photoresist layers prevents the (vertical) crosslinking between PEDOT:PSS chains placed respectively on the glass substrate and above the photoresist layers. **c)** Sample structure after PEDOT:PSS deposition, when only one layer of photoresist is deposited. Once lift-off is performed, PEDOT:PSS chains crosslinked between the substrate and the photoresist layer are not completely removed and cause broadening of the film boundaries.

➢ **Step 7: preparation and deposition of the PEDOT:PSS solution:**

The active region of the EgVDP devices was realized by depositing on the samples a solution composed by:

- Basic solution: PEDOT: PSS Clevios PH1000
- 5% Ethylene Glycol (EG)
- 1% glycidoxypropyl trimethoxylane (GOPS)
- 0.25% Dodecylbenzene-sulfuric acid (DBSA)

where the volume percentages are referred to the total volume of the solution. EG is a secondary additive that is used to make PEDOT: PSS more conductive. GOPS is a crosslinker that improves the formation of covalent bonds between the polymer chains, increasing the stability of the films in aqueous solution. DBSA is a surfactant that is used to lower the surface tension of the solution, which consequently relaxes with more ease on the glass substrate, improving its adhesion. A 10 ml solution was prepared by adding through a pipette EG, GOPS and DBSA into PEDOT: PSS PH1000 according to the order mentioned. Once composed, the solution was posed ten minutes in an ultrasonic bath to mix it and improve its homogeneity. During this time, substrates were treated by air plasma cleaning. This process removes remaining traces of photoresist and activates OH groups on the surface, improving PEDOT:PSS adhesion. It is advisable to deposit the solution on the substrate immediately after mixing, as the presence of additives (in particular the cross-linking agent) tends to aggregate the polymer chains, forming lumps and deposits on the edges of the container. The PEDOT: PSS solution was deposited on the slides using the spin-coating technique. Before its application on the substrates, the solution was filtered with a cellulose acetate filter, with pores of the diameter of 1.2μm. Spin-coating was performed at 3000 rpm. The angular velocity was reached in t_{ramp} = 1 s (3000 rpm/s acceleration), and maintained for t_{dwell} = 9 s. Finally, samples were annealed at 120° C on a hot plate for 1 hour.

- **Step 8: photoresist lift-off:**

After PEDOT:PSS deposition, samples were placed in a container with acetone and immersed for 4 hours and 30 minutes. During lift-off, acetone dissolved the photoresist and, consequently, all the PEDOT:PSS film regions which had been deposited onto it. Samples were then immersed in a new container with fresh acetone and sonicated for 10 s to remove all remaining resist. This procedure was repeated in isopropanol and distilled water. Finally, samples were blow-dried with nitrogen flow.

2.1.3 Fabrication of millimeter-sized EgVDP devices

Millimeter-sized devices were fabricated with a simpler process. 2.5x2.5 cm glass substrates were cleaned through the procedure discussed in step 0 of the previous list. Then, PEDOT:PSS was prepared and deposited following the procedure in step 7. The sample pattern in Fig. 2.1.1 was impressed by manually scratching PEDOT:PSS thin film with a razor blade. The film geometry was drawn on a piece of graph paper and carefully reproduced on the sample with the help of a microscope. Finally, metallic contacts were realized by applying silver paste directly in the designed positions of the polymeric film.

2.1.4 Fabrication two-contacts devices

Two-contacts devices were realized with the microfabrication process used for the miniaturized EgVDP samples, but with a different design (see Fig. 2.1.3).

2.2 PEDOT:PSS thin films characterization methods

Electrolyte-gated van der Pauw (EgVDP) measurements combined with electrochemical impedance spectroscopies (EIS) and cyclovoltammetries (CV) were performed to study the charge transport and accumulation in PEDOT:PSS thin films. The experimental procedure adopted for the characterization of the fabricated samples is discussed in detail in this section.

2.2.1 Experimental setup

EgVDP characterization requires a measurement system which is able to perform 4-point probe (4PP) measurements and to simultaneously control a voltage applied in solution. The abstract electrical circuit needed for this scope is presented in **Figure 2.2.1.**

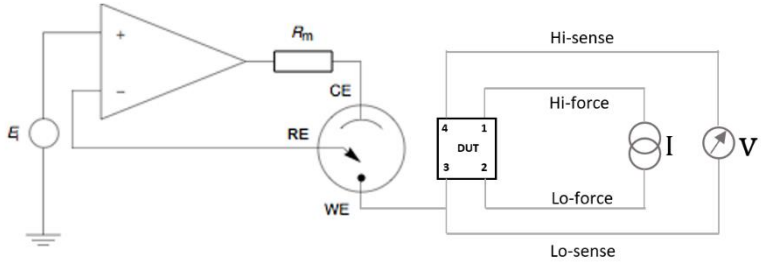

Figure 2.2.1: Electrical circuit needed to perform the EgVDP characterization. The voltage applied in solution is controlled through a potentiostat (left), while a current generator and a voltmeter (right) are needed to perform 4-wires measurements. The contacts on the EgVDP sample are indicated with numbers.

The Keysight B2912A source-measure unit (SMU) and the Autolab PGSTAT 204 potentiostat were used for this scope. A schematic overview of the experimental setup is reported in **Figure 2.2.2** The SMU disposes of two independent measurement channels, both supporting 4-wire measurement function. The four contacts of the fabricated EgVDP devices were connected to channel 1. In the 4-wire scheme, two of the connectors forced current and the other two connectors measured the corresponding voltage drop on the sample.
Meanwhile, the potentiostat was used to control the potential applied in solution. The working electrode (WE) was connected to the low-sensing voltage terminal of the SMU. In this way, the measurements of both the voltage drop on the sample and the voltage applied in solution were referred to a common terminal. The counter electrode (CE) and the reference electrode (RE) of the potentiostat were placed in direct contact with the electrolyte and were respectively constituted by a platinum wire and by a silver/silver chloride electrode. The voltage applied in solution $-E = -(V_{WE} - V_{RE}) = -(V_{WE} - V_{Ag/AgCl})$, was measured by the potentiostat and acquired with the second SMU channel, which acted as an analog to digital converter (ADC).
Samples were covered with the contact-protecting PDMS film (see section 2.1.1) and mounted in an electrolytic cell. The cell was then placed inside a faradaic cage. The PEDOT:PSS film was put in direct contact with a 0.1 M phosphate-buffered saline (PBS) solution. Literature studies [51] demonstrate faradaic side reactions between PEDOT and oxygen. Therefore, we performed the measurements in a nitrogen atmosphere by keeping the cell under a continuous nitrogen flow. Our experimental setup did not have a measurement system able to quantitatively determine the amount of gasses dissolved in solution. For this reason, we applied the nitrogen flow directly in solution for one hour before stating the measurement, and after that we assumed a completely nitrogen-saturated atmosphere in the cell. The role of oxygen-related

charge transfer was analyzed with preliminary measurements, whose results are presented in Section 3.2.1

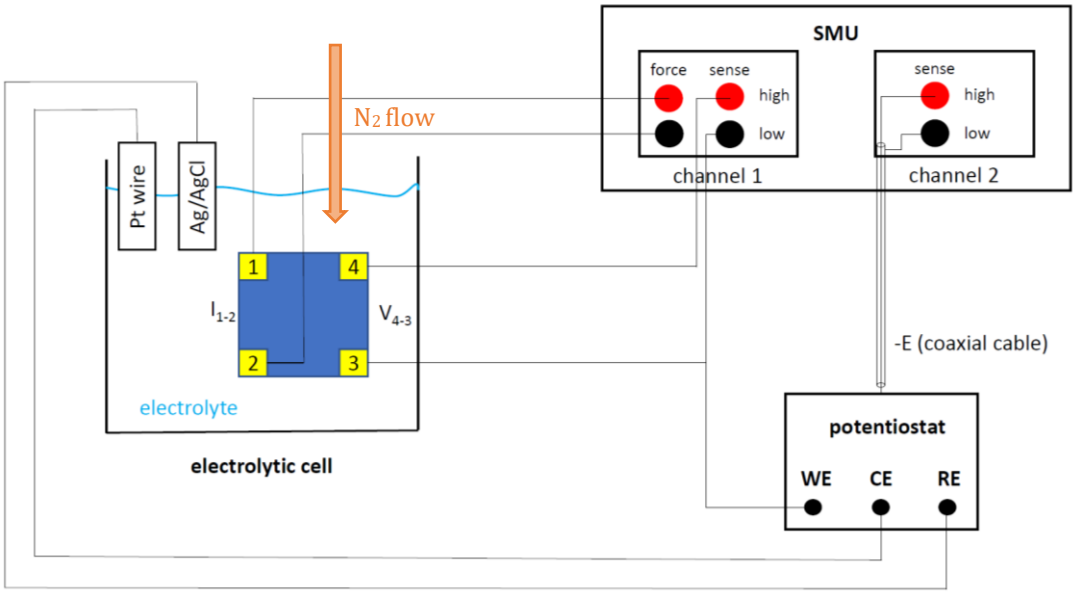

Figure 2.2.2: Scheme of the experimental setup used in the experiments for EgVDP characterization.

2.2.2 Measurements

Three different measurement techniques were adopted for the samples' characterization:

- **Electrochemical impedance spectroscopy (EIS)**

EIS is an electrochemical technique to measure the frequency response of a system in dependence of an applied AC potential. The potentiostat generates an AC voltage between the working and the reference electrodes over a wide range of frequencies and gives the possibility to apply an DC offset to the generated AC signal.

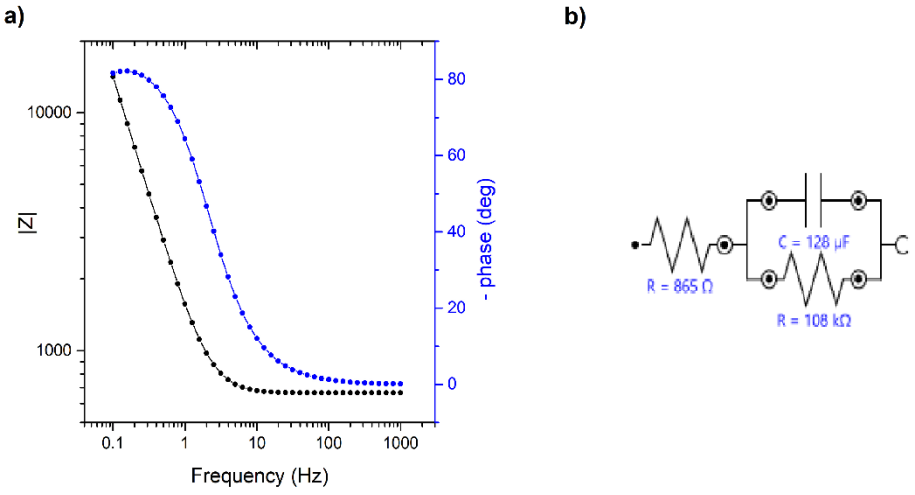

Figure 2.2.3: a) Bode plot resulting from an electrochemical impedance spectroscopy. Dots indicate experimentally acquired values, while lines are fit curves corresponding to the transfer function of the circuit in **b)**. The physical interpretation of the circuital components is crucial to investigate the charge transfer and accumulation mechanisms on the sample.

An integrated frequency response analyzer (FRA) measures the transfer function of the samples and provides their Bode plot, containing the impedance and the phase shift versus the applied signal frequency. The Bode plot can be fitted with the frequency response of an equivalent circuit, providing an electrical modeling of the characterized system. An example of EIS is reported in **Figure 2.2.3:**In this work, we performed EIS in the frequency range between 0.1 and 1000 Hz. The generated input signal was constituted by a sinusoidal wave, with 10 mV rms amplitude. During measurements, the four contacts of the sample were short-circuited to maintain a more uniform electrical potential on the PEDOT:PSS film. EIS was used for many purposes:

1) Analysis of the redox processes between PEDOT and oxygen:

Preliminarily to the EgVDP characterization, we performed EISs to study the electrochemical processes between PEDOT and oxygen. PEDOT:PSS was deposited on 2.5x2.5 cm microscope slides coated with indium-tin oxide (ITO). The preparation of the PEDOT:PSS solution and its deposition are reported in step 7 of **Section 2.1.2**. PEDOT:PSS-ITO samples were then mounted on the electrolytic cell, and EISs were executed in air at different DC offset voltages (corresponding to different potential applied in solution). Then, measurements were repeated after keeping the cell on a nitrogen flow for one hour, where we assumed a 100% nitrogen atmosphere. A comparison between the obtained results provides a quantitative investigation of redox processes between PEDOT and the oxygen dissolved in solution.

2) Analysis of the PEDOT:PSS/electrolyte interface:

EIS was used to investigate charge transport and accumulation processes between the PEDOT:PSS film and the electrolyte in EgVDP samples. The interface double layer capacitance (gate capacitance) was measured in function of the applied DC voltage in solution. Moreover, through EIS we monitored the presence of parasitic charge transfer processes in the samples, such as faradaic side reactions.

- **Cyclovoltammetry (CV)**

In cyclovoltammetry, the potential $E = V_{WE} - V_{RE}$ is varied at a constant rate $dE/dt = s$ in forward and backward direction over a constant potential interval. Meanwhile, the current flowing from the working electrode is measured. An example of CV is reported in **Figure 2.2.4:**

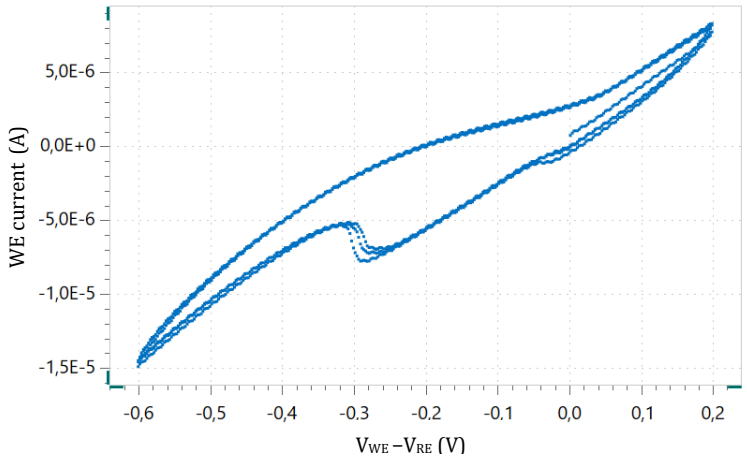

Figure 2.2.4: Example of cyclovoltammetry. The applied potential E is varied in the range between 0.2 and -0.6 V and the WE current is measured. The potential scan is repeated three times.

Current peaks in correspondence of fixed applied voltages indicates the presence of faradaic reactions. Due to the constant variation in potential, a constant capacitive current is always present. The sign of the current changes with the scan direction. CVs were performed to characterize each EgVDP sample, with a constant scan rate of 0.1 V/s. The voltage scan was repeated three times in every CV to observe the stability of the sample response.

- **Electrolyte-gated van der Pauw measurements:**

The four contacts of the EgVDP samples were connected to the experimental setup according to Fig. 2.2.1. A constant current was injected between contacts 1 and 2 by the first SMU channel, and the corresponding voltage drop between contacts 4 and 3 ($V_{4\text{-}3}$) was measured (HiF1LoF2HiS4LoS3 configuration, where F and S indicates respectively the forcing and the sensing terminal of the SMU channel). The magnitude of the injected current is an important parameter to set. Higher current values increase the signal-to-noise ratio, but produce large voltage drop on the sample, which must be avoided to prevent its damage. The current intensity was set to maintain the maximum voltage drop during the characterization under 0.2 V, to avoid non-linear effects in the conducting channel. Simultaneously to the 4PP measurements, a voltage $V_{sol} = V_{Ag/AgCl} - V_{WE} = V_{Ag/AgCl} - V_3$ was applied in solution with the potentiostat. Its value was scanned in a selected range to modify the conductivity of the PEDOT:PSS thin film (electrolyte gating). During each step, V_{sol} was kept constant for 10 s and then increased (or decreased) by 0.04 V (scan rate s = 40 mV/10 s). The potential scan was repeated twice for each characterization, in order to test the reproducibility of the sample response. An example of the results of the measurements is reported in **Figure 2.2.5:**

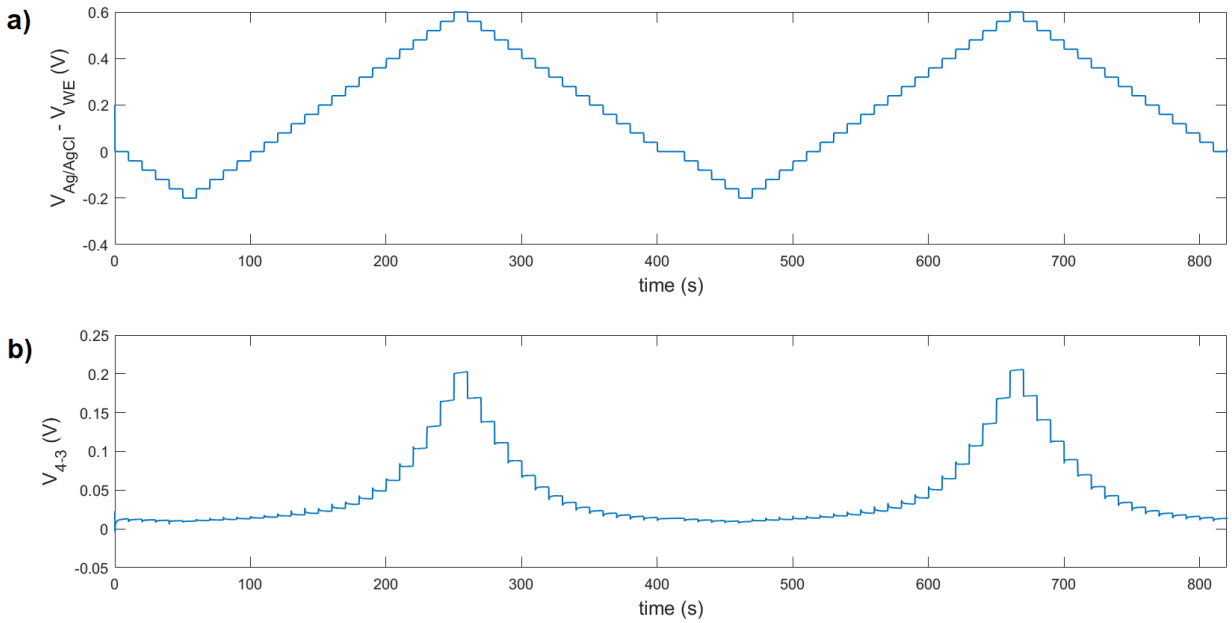

Figure 2.2.5: Example of EgVDP measurement. **a)** Starting from 0 V, the potential applied in solution is varied in the range between -0.2 and 0.6 V with a constant scan rate of 40 mV/10 s. The scansion is repeated twice. **b)** Corresponding voltage drop $V_{4\text{-}3}$ on the sample (see Fig. 2.2.1 for the electrical connection). The injected current is 0.01 mA. When $V_{Ag/AgCl} - V_{RE}$ assumes high positive values, the corresponding $V_{4\text{-}3}$ increases because of the decrease in conductivity of the PEDOT:PSS thin film.

The sample resistance $R_{12,34} = |V_4 - V_3|/I_{1,2}$ was calculated in function of V_{sol} by dividing the potential drop $V_{4\text{-}3}$ by the injected current intensity. Then, eq. 1.4.5 was applied to calculate the thin film sheet resistance $R_{S\text{-}12,34} = \pi R_{12,34}/ln(2)$. Values obtained in the two V_{sol} scan were

averaged. Then, the sheet resistance $R_{S\text{-}12,43}$ was measured by reversing the injected current direction. The same procedure was repeated for the HiF2LoF3HiS1LoS4 configuration. At the end of the measurements, four sheet resistance values were obtained for each V_{sol} step. These were averaged to calculate the mean sheet conductance as $\langle\sigma_S\rangle = \langle R_S\rangle^{-1} = ln(2)/(\pi\langle R\rangle)$.

Before starting the measurements, EgVDP samples were modeled with an equivalent electrical circuit and the measurement setup was tested. The circuit scheme is shown in **Figure 2.2.6**.

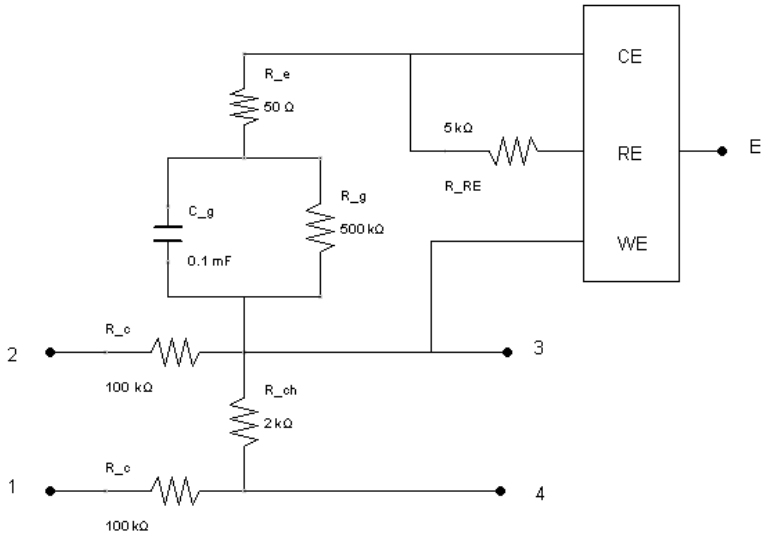

Figure 2.2.6: Equivalent circuit modeling of an EgVDP sample. The values of its components were estimated for the millimeter-sized devices (see Fig. 2.1.1), with film area $A \approx 37$ mm^2 and thickness 200 nm.

Because of the 4 wires configuration, the contact resistance R_C affects only the current-forcing contacts. The voltage drop $V_{4\text{-}3}$ on the PEDOT:PSS film was modeled with the channel resistance R_{ch}, while the gate capacitance (C_g) and resistance (R_g) describe charge transfer and accumulation at the film/electrolyte interface. The electrolyte resistance is indicated with R_e. Once a voltage V_{sol} is applied in solution, the EgVDP equivalent circuit behaves as an RC circuit, and a transient response is followed by a stationary behavior

$$V_{4-3}(t) = \left[\frac{V_{sol} + I_{1,2}(R_e + R_g)}{R_e + R_g + R_{ch}} R_{ch}\right]\left[1 - exp\left(-\frac{t}{R_e C_g + R_{ch} C_g}\right)\right] \qquad 2.2.1$$

where the time constant of the circuit is given by $\tau = (R_e + R_{ch})C_g$. In stationary condition, if the gate (or leakage) current is negligible with respect to the injected current ($R_g >> R_{ch}$), the channel resistance can be approximated with $R_{ch} \approx R_{12,34} = |V_4 - V_3|/I_{1,2}$, as it was done in the samples' characterization.

2.2.3 Characterization of two-contacts samples

The electrochemical properties of two-contacts samples were analyzed through EIS and CV. The procedure adopted for the measurements was the same used for EgVDP devices. 2-wires measurements were performed to study the charge transport properties of the samples. A potential difference $V_{1\text{-}2}$ was applied between the two contacts, and the resulting current was measured. The electrical scheme of the experimental setup is reported in **Figure 2.2.7**.

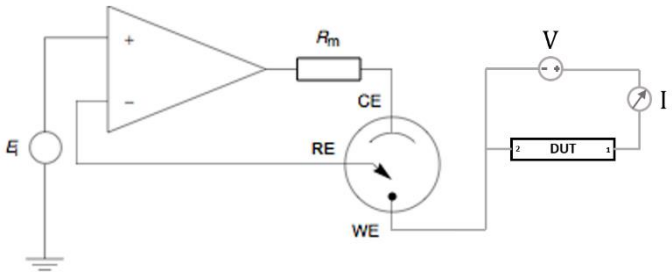

Figure 2.2.7: Electrical circuit needed to perform the characterization of two-contact devices. The voltage applied in solution is controlled through a potentiostat (left), while a voltage generator and an ammeter are needed to perform 2-wires measurements.

Simultaneously to the 2-wires measurements, a voltage $V_{sol} = V_{Ag/AgCl} - V_{WE} = V_{Ag/AgCl} - V_2$ was applied in solution with the potentiostat. Its value was scanned in a selected range to modify the conductivity of the PEDOT:PSS thin film (electrolyte gating). During each step, V_{sol} was kept constant for 10 s and then increased (or decreased) by 0.04 V (scan rate s = 40 mV/10 s). An example of the results of the measurements is reported in **Figure 2.2.8:**

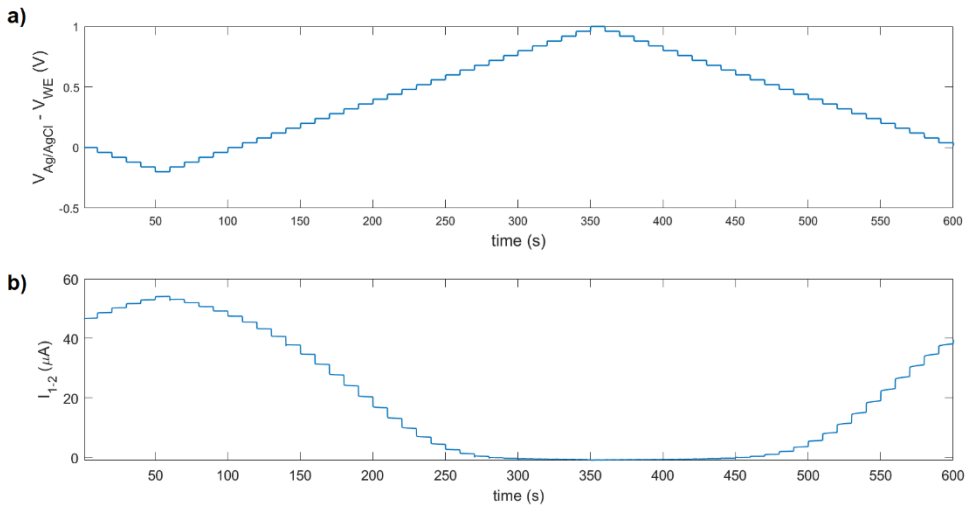

Figure 2.2.8: Example of a two-contact characterization. **a)** Starting from 0 V, the potential applied in solution is varied in the range between -0.2 and 1 V with a constant scan rate of 40 mV/10 s. **b)** Corresponding current $I_{1\text{-}2}$ flowing in the sample. The voltage applied between the contacts is 0.05 V. When $V_{Ag/AgCl} - V_{RE}$ assumes high positive values, the corresponding $I_{1\text{-}2}$ decreases because of the decrease in conductivity of the PEDOT:PSS thin film.

Electrolyte-gated 2-contacts devices are fully equivalent to organic electrochemical transistors, where the low-biased and the high-biased contacts are respectively the source and the drain terminals of an OECT. Consequently, $V_{1\text{-}2}$ acts as a drain voltage, V_{sol} as a gate voltage, and $I_{1\text{-}2}$ is the resulting drain current. The two-contacts characterizations measure I_{drain} in function of V_{sol}, and therefore the transfer characteristic of the OECT. Transfer curves were acquired and analyzed both in linear and in saturation regime to extract the holes' mobility in PEDOT:PSS.

CHAPTER 3: RESULTS

This section introduces the main results obtained in this work. The first paragraph presents the PEDOT:PSS thin film devices realized with the fabrication techniques illustrated in sect. 2.1.2/3/4. The second paragraph is focused on the interaction between PEDOT and the oxygen dissolved in the electrolyte. In the third paragraph, electrochemical impedance spectroscopies are analyzed to study charge accumulation in PEDOT:PSS. Then, the transport properties of organic electrochemical transistors are studied from the characterization of two-contacts devices. Finally, EgVDP measurements are examined both for millimeter-sized and miniaturized samples and a first analysis is applied to extract relevant material properties, such as the charge carrier mobility.

3.1 Fabrication of PEDOT:PSS thin film devices

We fabricated three different kind of devices for the characterization of PEDOT:PSS thin films, as reported in chapter 2.1. Results are shown in **Figure 3.1**. Micro-structured EgVDP samples (**fig. 3.1 a**) and two-contacts samples (**fig. 3.1 c**) were realized through microfabrication techniques, using photolithography.

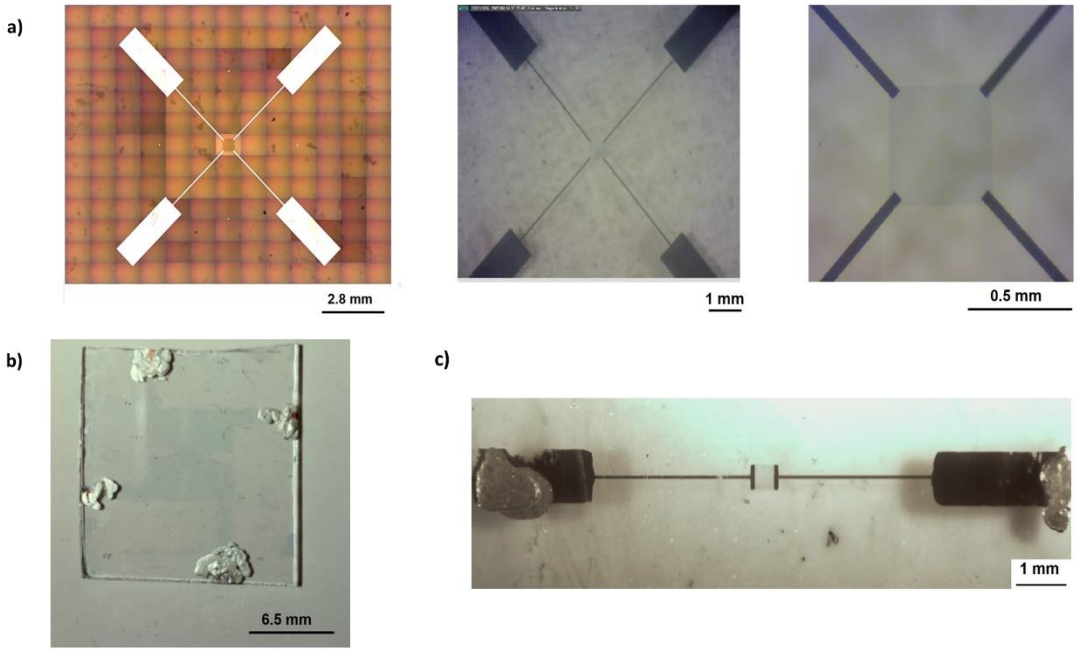

Figure 3.1: Fabrication results. **a)** Left: microfabricated EgVDP device. The picture was taken through the microwriter microscope. Center: optical microscopy of the device. Right: detail on the PEDOT:PSS thin film placed at the center of each sample. **b)** Picture of a millimeter-sized EgVDP sample. The film geometry is barely visible because of the thin layer of the spin coated PEDOT:PSS film. **c)** Optical microscopy of a microfabricated two-contact sample. The PEDOT:PSS thin film is clearly visible at its center. Conductive silver paste was placed on the golden pads to connect the device with the measurement system.

The optical micrographs demonstrate the well-defined gold contacts serving as electrodes for the measurements. The area covered by PEDOT:PSS gets visible by its slightly blue color due to the absorption of reduced PEDOT polymers. Due to the patterning technique I was able to

confine the active layer on a size of 500x500 µm, with important effects on the measurements as outlined below. For comparison also millimeter-sized EgVDP samples (**fig. 3.1 b**) were patterned by manually scratching the deposited PEDOT:PSS thin film with a razor blade.

3.2 Analysis of the oxygen-related charge transfer processes in PEDOT:PSS thin films

The electrochemical impedance spectroscopies of ITO/PEDOT samples in air and in a 100% N_2 environment are presented in **Figure 3.2**. Bode plots obtained for two different voltages applied in solution, respectively $V_{Ag/AgCl} - V_{WE} = V_{sol} = -0.2$ V and $V_{sol} = 0.6$ V are compared. Each plot depicts the acquired impedance and phase in function of the input signal frequency. The transfer function of the ITO/PEDOT samples is fitted the one of an equivalent electrical circuit.

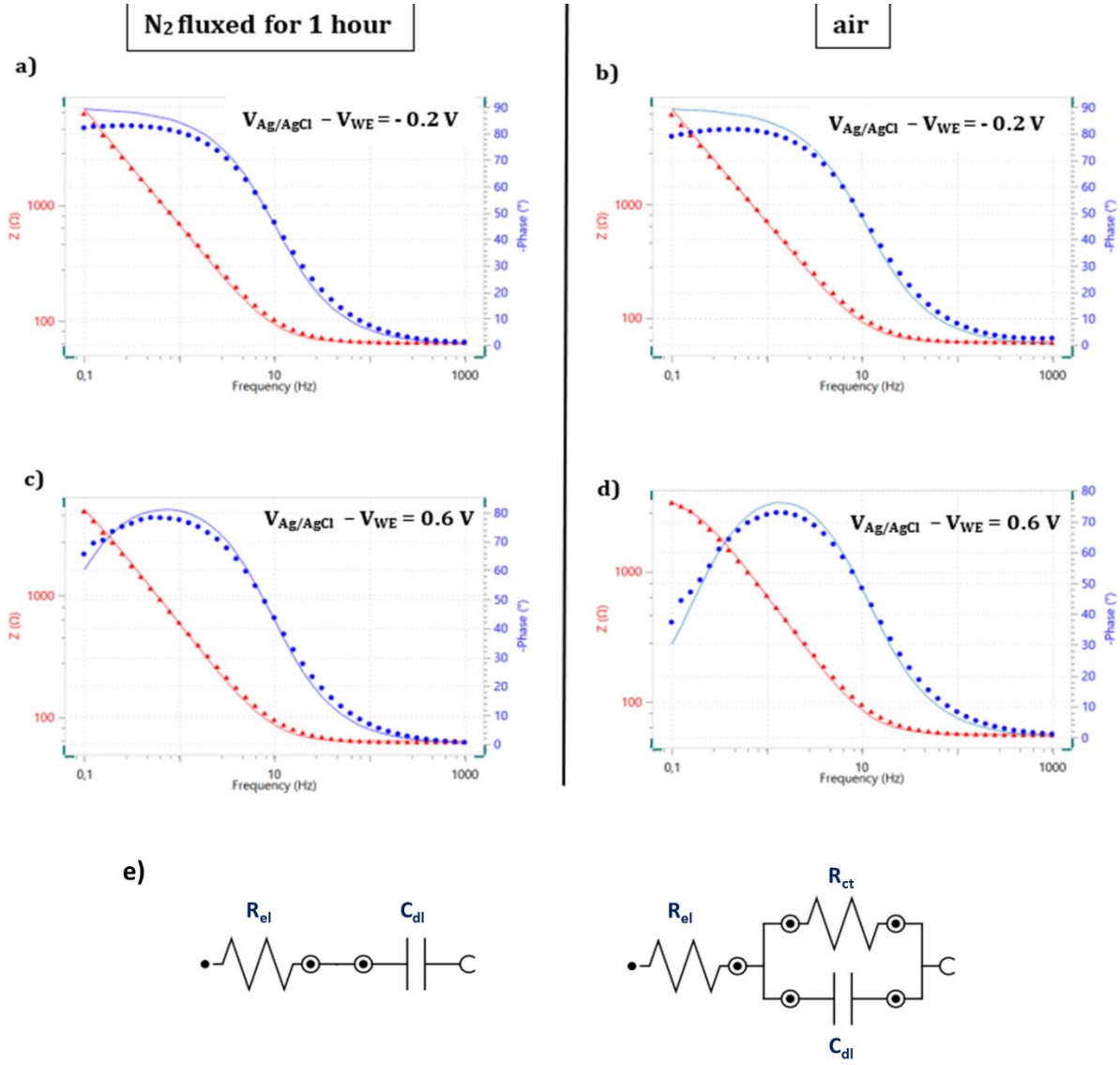

Figure 3.2: Analysis of the oxygen-related charge transfer between PEDOT and the electrolyte. Comparison between EISs performed in air (**b** and **d**) and in 100% nitrogen (**a** and **c**) for ITO-PEDOT:PSS/electrolyte interface. Dots indicate experimental values, while lines are equivalent circuit fits. Two different potentials are applied in solution, respectively $V_{sol} = -0.2$ V (**a** and **b**) and $V_{sol} = 0.6$ V (**c** and **d**). **e)** Scheme of the equivalent circuits for $V_{sol} = -0.2$ V (left) and $V_{sol} = 0.6$ V (right). The results of the fits are reported in **table 3.2**.

We can observe that the charge transfer processes between the samples and the electrolyte depend on the applied voltage. When V_{sol} = -0.2 V, the system can be modeled with a RC series circuit, whose components indicate respectively the electrolyte resistance (R_{el}) and the double layer capacitance (C_{dl}) at the PEDOT:PSS/electrolyte interface. On the other hand, when V_{sol} = 0.6 V charge transfer processes are clearly observable: the phase value decays and also the impedance deviates from the reciprocal relationship with frequency. Therefore, interface cannot be described with a simple RC circuit, but an additional resistor R_{ct} must be connected in parallel with C_{dl} to model charge transfer processes between the film and the electrolyte.
The quantitative results of the fits are presented in **Table 3.2.** We can observe that the value of R_{ct} is higher in measurements acquired in nitrogen.

environment	**V_{sol}**	**R_{el}**	**C_{dl}**	**R_{ct}**
air	-0.2 V	(61.9±1.3) Ω	(229±5) µF	–
N_2	-0.2 V	(66.2±1.1) Ω	(234±4) µF	–
air	0.6 V	(56.0±0.3) Ω	(204±2) µF	(3.90±0.13) kΩ
N_2	0.6 V	(62.6±0.3) Ω	(236±2) µF	(10.6±0.7) kΩ

Table 3.2*:* Equivalent circuit components resulting from the analysis of EISs in Figure 3.2.

The obtained results demonstrate qualitatively and quantitatively the presence of redox processes between PEDOT and O_2. When V_{sol} = 0.6 V, the charge transfer mechanisms at ITO/PEDOT:PSS - electrolyte interface are more pronounced in air, and the two environments are clearly distinguishable from EISs. On the other hand, when V_{sol} = -0.2 V faradaic reactions between the samples and the electrolyte are strongly inhibited. The main faradaic process between PEDOT:PSS and oxygen is the two-electron reaction $O_2 + 2H^+ + 2e^- \rightarrow H_2O_2$. [51] The application of a negative bias in solution decreases the free energy gain of the process, and the electron transfer at the PEDOT:PSS-electrolyte interface is strongly reduced. Anyway, the in-depth analysis of such reactions is not objective of this work. Oxygen-related electron transfer mechanisms are in this contest faradaic side reactions that should be avoided during EgVDP characterization. Therefore, the electrochemical impedance spectroscopy of the ITO/PEDOT:PSS-electrolyte interface indicates the importance to perform the thin-film characterization in a nitrogen-saturated environment. The presence of charge transfer processes in N_2 when V_{sol} = 0.6 V probably indicates that it is not possible to deplete completely the electrolyte from oxygen, or the presence of an additional parasitic faradaic process which was not identified.

3.3 Charge carrier density in PEDOT:PSS thin films

The capacitance of the PEDOT:PSS-electrolyte interface was measured to study charge accumulation processes in PEDOT:PSS thin films. The electrochemical impedance spectroscopy of the PEDOT:PSS-electrolyte interface in millimeter-sized samples is reported in **Figure 3.3.1 a**. Measurements were fitted with the equivalent circuit in **Fig. 3.3.1 b.**

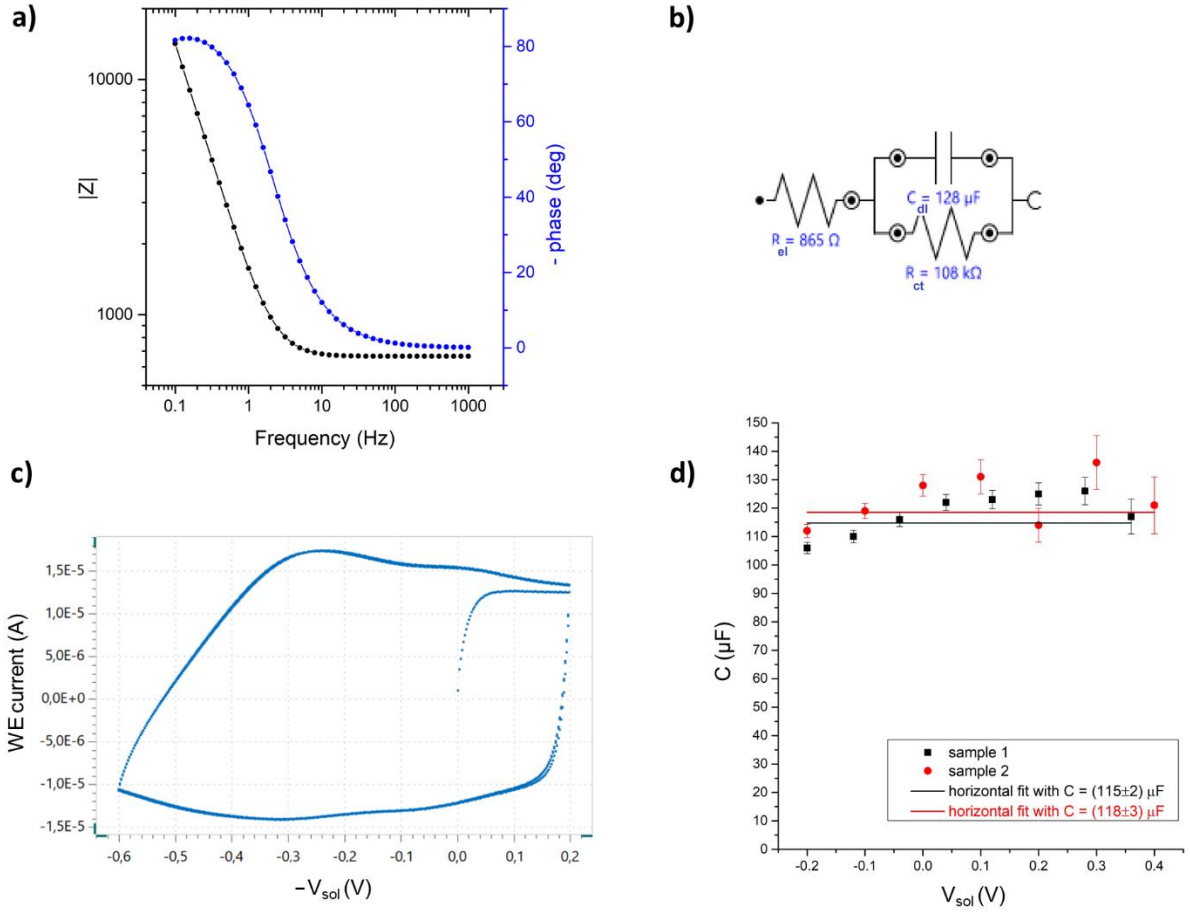

Figure 3.3.1: Capacitance measurements and electrochemical characterization of manually patterned millimeter-sized EgVDP devices. **a)** EIS of PEDOT:PSS-electrolyte interface. The voltage applied in solution is $V_{Ag/AgCl} - V_{WE}$ = 0 V. Dots indicate experimental values, while lines are the equivalent circuit fit. **b)** Equivalent circuit of the interface. **c)** Cyclovoltammetry of a millimeter-sized EgVDP sample. The scan rate was set to s = 0.1 V/s. The scan was repeated three times to test the stability of the sample response. **d)** Capacitance of the PEDOT:PSS/electrolyte interface in function of the voltage applied in solution. Results obtained for two millimeter-sized samples are compared and fitted with a horizontal line, getting C_1 = (115±2) µF and C_1 = (118±3) µF.

The interface is accurately modeled by a RC circuit (χ^2_{fit} = 0.26), where the electrolyte resistance R_{el} is connected in series with the double layer capacitance C_{dl} and the charge transfer resistance R_{ct}. The acquired data does not permit to extract a value for R_{ct}, because the phase remains almost at 90° at low frequencies. Therefore, the reported value has to be interpreted as an upper limit for the charge transfer resistance. The double layer capacitance of millimeter-sized EgVDP samples is quite high (C_{dl} = (128±4) µF), due to the large area of the film immersed in the electrolyte (≈ 37 mm^2) and to the high volumetric capacitance of PEDOT:PSS (from 20 to 30 F/cm^3, depending on the formulation of the deposited PEDOT:PSS solution) [52].

Figure 3.3.1 c reports a cyclovoltammetry obtained in the range -0.2 V < V_{sol} < 0.6 V. The sample shows an almost-capacitive behavior. A charging ramp starting from the lower vertex potential (-V_{sol} = -0.6 V) is followed by a stationary state, with a constant WE current. The same trend is repeated once the scan direction is reversed, and the current flows in the opposite sense. The curve is analogous to the CV of an ideal RC circuit. In such a case, the stationary current is expressed by $I_{WE}^{RC} = C \cdot s_r$, being s_r the CV scan rate. If we apply this equation to the measurements (with s_r = 0.1 V/s and C = 120 µF), we expect a stationary current of 12 µA, which is consistent with the observations. The large area between the forward and the backward scan of the CV is due to the large capacitance of the devices.
C_{dl} was measured in function of the voltage applied in solution. The results obtained for two different samples are presented in **Figure 3.3.1 d**.
We observe that the PEDOT:PSS capacitance is independent from V_{sol}, and its value is approximately constant in the voltage range in which the EgVDP characterizations were performed (-0.2 V < V_{sol} < 0.4 V). Therefore, measurements were fitted with a constant line, and the resulting mean capacitances are compatible to each other within the experimental errors. The average volumetric capacitance of the film was calculated to be (19±2) F/cm^3, which coincides with the one measured in Tybrandt's work .

The same analysis was repeated for microfabricated devices. The electrochemical impedance spectroscopy of the PEDOT:PSS-electrolyte interface in miniaturized EgVDP samples is reported in **Figure 3.3.2 a**. Measurements were fitted with the equivalent circuit in **Fig. 3.3.2 b**.

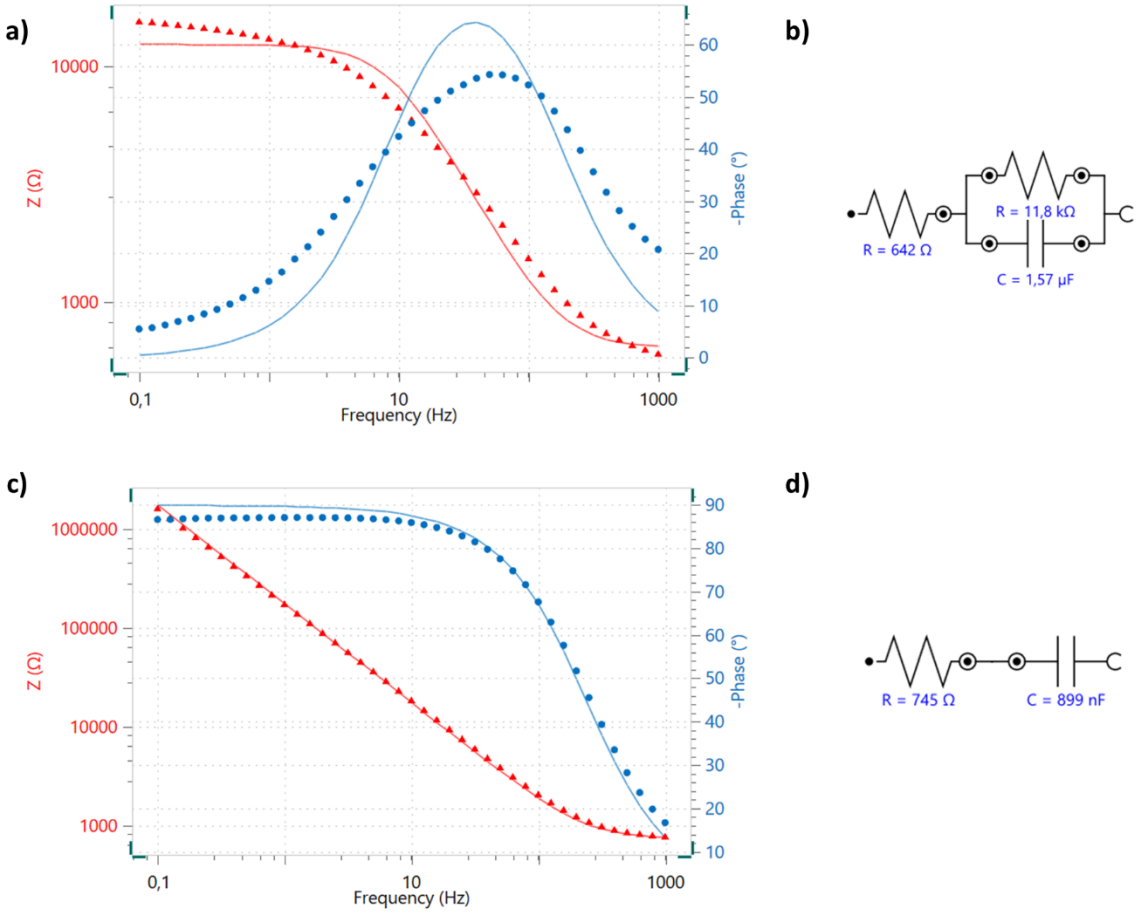

Figure 3.3.2: Characterization of PEDOT:PSS-electrolyte interface in microfabricated devices. EIS of miniaturized EgVDP samples (**a**) and of two-contacts samples (**c**). The voltage applied in solution is $V_{Ag/AgCl} - V_{WE}$ = 0 V. The equivalent circuits of the interfaces are reported respectively in figures **b** and **d**.

As for millimeter-sized devices, the interface can be modeled by a RC circuit, where the electrolyte resistance is connected in series with the double layer capacitance and the charge transfer resistance, but the goodness of the fit is lower (χ^2_{fit} = 1.52). As we expected, miniaturization has reduced the sample capacitance of two orders of magnitude, because the PEDOT:PSS film area was diminished from 37 mm^2 to 0.25 mm^2, and the thickness unchanged (t ≈ 170 nm). The results obtained for millimeter-sized devices demonstrate that the interface capacitance is independent from the voltage applied in solution (see Fig. 3.3.1 d). For this reason, the EIS of miniaturized devices was acquired only for V_{sol} = 0V. The average volumetric capacitance of the film was calculated to be (25±4) F/cm^3, which is consistent with the one measured in millimeter-sized samples.

The impedance spectroscopy in Fig. 3.3.2 a indicates the presence of a charge transfer process between the sample and the electrolyte. The phase decays rapidly at low frequencies and the charge transfer resistance R_{ct} is one order of magnitude smaller with respect to the one measured in millimeter-sized devices. This charge leakage is probably related to some non-ideality during that fabrication run, and not a consequence of the miniaturization process. In fact, the effect is not visible in the EIS of two-contacts devices, which were realized with the same fabrication procedure.

Figure 3.3.2 c shows the electrochemical impedance spectroscopy of the PEDOT:PSS-electrolyte interface of a two-contacts sample. Measurements were fitted with the equivalent circuit in **Fig. 3.3.2 d**. The interface acts as an almost ideal RC circuit. The absence of a charge transfer resistance indicates the absence of parasitic Faradaic reactions between the film and the electrolyte. As expected, the obtained double layer capacitance C = (0.90±0.09) μF is compatible with the one of miniaturized EgVDP samples (<C> = (1.1±0.2) μF) because the PEDOT:PSS film area is the same in both devices.

3.4 Transport properties of organic electrochemical transistors

Electrolyte-gated two-contacts devices are fully equivalent to organic electrochemical transistors. Therefore, the characterization of two-contacts samples can be examined to investigate the transport properties of miniaturized OECTs. The transfer curve of a two-contacts device is presented in **Figure 3.4 a**. V_{sol} was scanned between -0.2 and 0.6 V, while the voltage applied between the contacts (V_{drain}) was fixed to 0.05 V. The behavior of the device is reproducible during the voltage scan, and measurements show a small hysteresis.

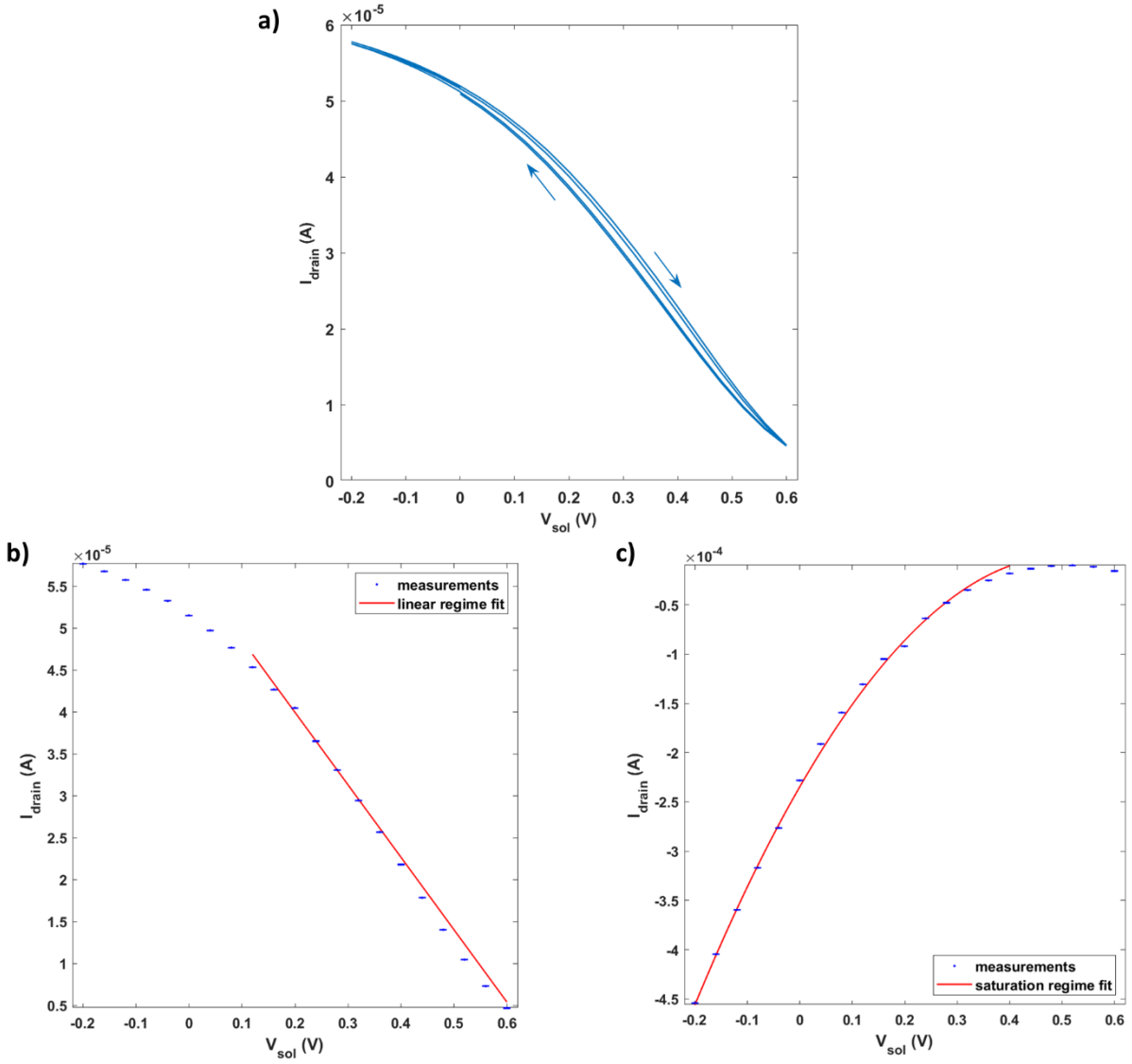

Figure 3.4: Characterization of miniaturized OECTs. **a)** Transfer curve of a two-contacts sample. Drain current is plotted as a function of the potential applied in solution. V_{sol} was varied between -0.2 and 0.6 V. The scan was repeated three times, with a scan rate of 0.04 V/10 s. The drain voltage is 50 mV. **b)** Linear regime fit with Bernards' model for OECTs. The applied drain voltage is 50 mV. **c)** Saturation regime fit with V_{drain} = -0.9 V. Quantitative results are reported in **Table 3.4**.

The charge carrier mobility can be extracted from the transfer curves of organic electrochemical transistors in two different regimes. When the applied drain voltage is small ($|V_{drain}| < |V_{sol} - V_t|$, being V_t the threshold voltage), the device physics is described by the Bernards' [53] model for OECTs in linear regime, and the drain current can be expressed as

$$I_{drain}^{lin} = \mu_{lin} c \frac{W}{L}\left(V_t - V_{sol} + \frac{V_{drain}}{2}\right) V_{drain} \qquad 3.4.1$$

where c is the capacitance per unit area of the sample, μ_{lin} is the holes' mobility in PEDOT:PSS (in linear regime), V_t is the threshold voltage and W and L are respectively the width and the length of the PEDOT:PSS conductive channel. For high drain voltages ($|V_{drain}| > |V_{sol} - V_t|$), the conductive channel pinches off near the drain contact, and I_{drain} is independent from V_{drain}. This condition is called saturation, and is expressed by the Bernards' model as

$$I_{drain}^{sat} = -\mu_{sat} c \frac{W}{L} \frac{(V_{sol} - V_t)^2}{2} \qquad 3.4.2$$

The transfer curves measured in linear (V_{drain} = 0.05 V) and saturation (V_{drain} = -0.9 V) conditions were fitted with eq. 3.1.2 and 3.1.3. The results of this analysis are reported in **Figure 3.4 b** and **c** and in **Table 3.4**:

V_{drain} (V)	regime	μ_p ($cm^2V^{-1}s^{-1}$)	V_t (V)
0.05	linear	4.6±0.3	0.53±0.03
– 0.9	saturation	5.0±0.2	0.56±0.03

Table 3.4: Results from the characterization of two-contacts samples.

3.5 Electrolyte-gated van der Pauw measurements

Results obtained in the EgVDP characterization of a millimeter-sized sample are presented in **Figure 3.5 a**. The measured sheet resistance (R_S) is plotted as a function of the potential applied in solution.

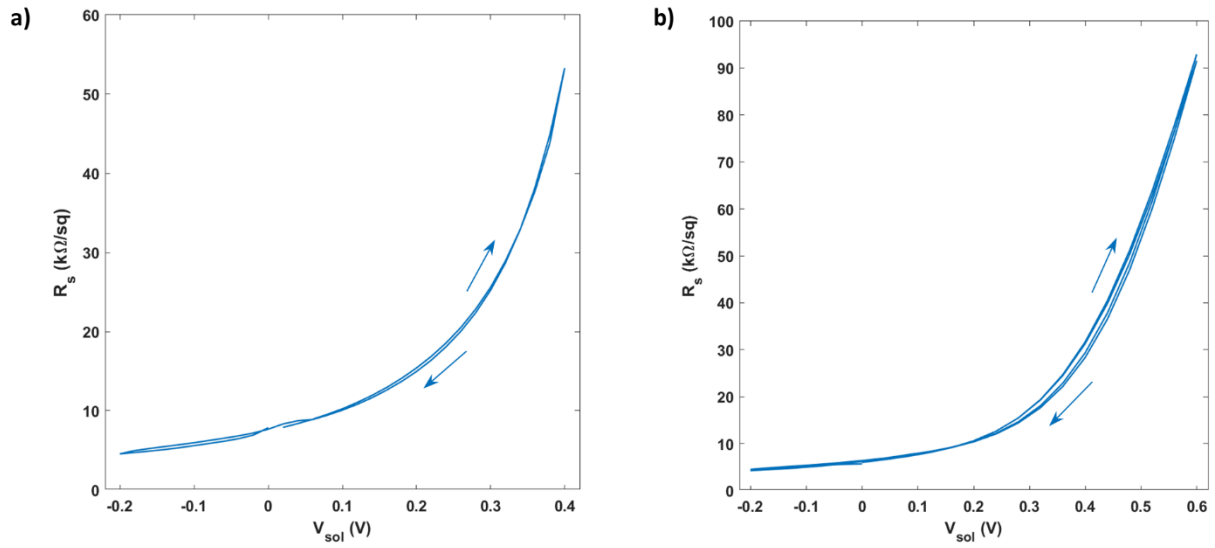

Figure 3.5.1: EgVDP characterization of a millimeter-sized **(a)** and of a microfabricated **(b)** sample. Sheet resistance is plotted as a function of the potential applied in solution. Measurements were acquired with a selected contact configuration (HiF1LoF2HiS4LoS3). The injected currents are respectively1 µA **(a)** and 10 µA **(b)**. Voltage scan is repeated twice.

We observe that R_S (resistivity per unit of thickness) and the voltage applied in solution are positively correlated. In fact, when V_{sol} is increased, the charge carrier concentration in the PEDOT:PSS film is reduced, and the resistivity of the sample becomes larger. The behavior of the samples is reproducible during the voltage scan and measurements show a very small hysteresis.
The same considerations can be repeated for microfabricated devices (**Fig. 3.5 b**). Measurements were performed in a larger potential range (-0.2 V < V_{sol} < 0.6 V) to study low carrier concentration regimes. The relation between R_S and the voltage applied in solution is qualitatively consistent with the one found for millimeter-sized samples. Even in this case, the device response in reproducible during the voltage scan.

3.5.1 Optimization of the sample geometry for EgVDP characterization

As discussed in **sect. 1.4.1**, the sample geometry is crucial to minimize contact misplacement errors during van der Pauw's characterization. For this reason, we patterned the PEDOT:PSS films on the fabricated devices with a specific shape. In electrolyte-gated measurements, another important effect is given by the film size. In fact, the transient response of the device once a potential step is applied in solution depends on its capacitance, which is proportional to the PEDOT:PSS film area in direct contact with the electrolyte.
In miniaturized samples, an additional capacitive contribution is given by the small portion of the gold tracks systematically placed in contact with the solution (see **fig. 2.1.2**). Anyway, the resulting parasitic capacitance is negligible ($C_{gold} \approx 46$ nF) because of the small specific capacitance of gold ($c = 20 \mu F/cm^2$).
Figure 3.5.2 a shows the behavior of an EgVDP sample when potential steps are applied in solution. As discussed in **sect. 2.2.2** and modeled by **eq. 2.2.1**, the voltage drop on the sample between contacts 4 and 3 reaches a stationary state after a transient RC response. The time duration of the transitory state depends on the time constant of the device (τ), which is proportional to its capacitance. The transient state of a millimeter-sized (**fig. 3.5.2 b**) and of a miniaturized (**fig. 3.5.2 c**) sample were fitted to extract the time constant and the stationary voltage (V_{stat}). In both cases, the voltage drop between contacts 4 and 3 is plotted in function of time. When t = 380 s in **fig. 3.5.2 b** (or t = 160 s in **fig. 3.5.2 c**) the voltage applied in solution is increased to $V_{sol} = 0.32$ V, and kept constant for 10 s. We note that in the miniaturized sample, the transient is too fast to be precisely measured with our experimental setup, and only an upper limit for the time constant can be determined.
Miniaturization has decreased the time constant of the devices of about two orders of magnitude (from $\tau_{mill} = (0.8475 \pm 0.008)$ s to $\tau_{micro} \leq (0.0099 \pm 0.0004)$ s), proportionally to the reduction of the film area (from $A_{mill} = 35$ mm^2 to $A_{micro} = 0.25$ mm^2). In fact, the capacitance of a PEDOT:PSS film depends on its volume, but the film thickness was the same in every sample because the blend was deposited with the same technique and parameters.
This analysis demonstrates that the large capacitance of millimeter-sized EgVDP samples is a strong limitation during the EgVDP characterization. When the carrier concentration in PEDOT:PSS is small, and the channel resistance is large, the charge/discharge processes are too slow for a reasonable scan rate on V_{sol}, and the circuit does not reach the stationary behaviour. For this reason, during the characterization of millimeter-sized samples it was not possible to apply voltages in solution above 0.4 V, and only a limited range of carrier concentration was studied. On the other hand, the small time constant of microfabricated devices allows measurements to be performed in a wider potential range: miniaturization is crucial to study low carrier concentration regimes in PEDOT:PSS thin films.

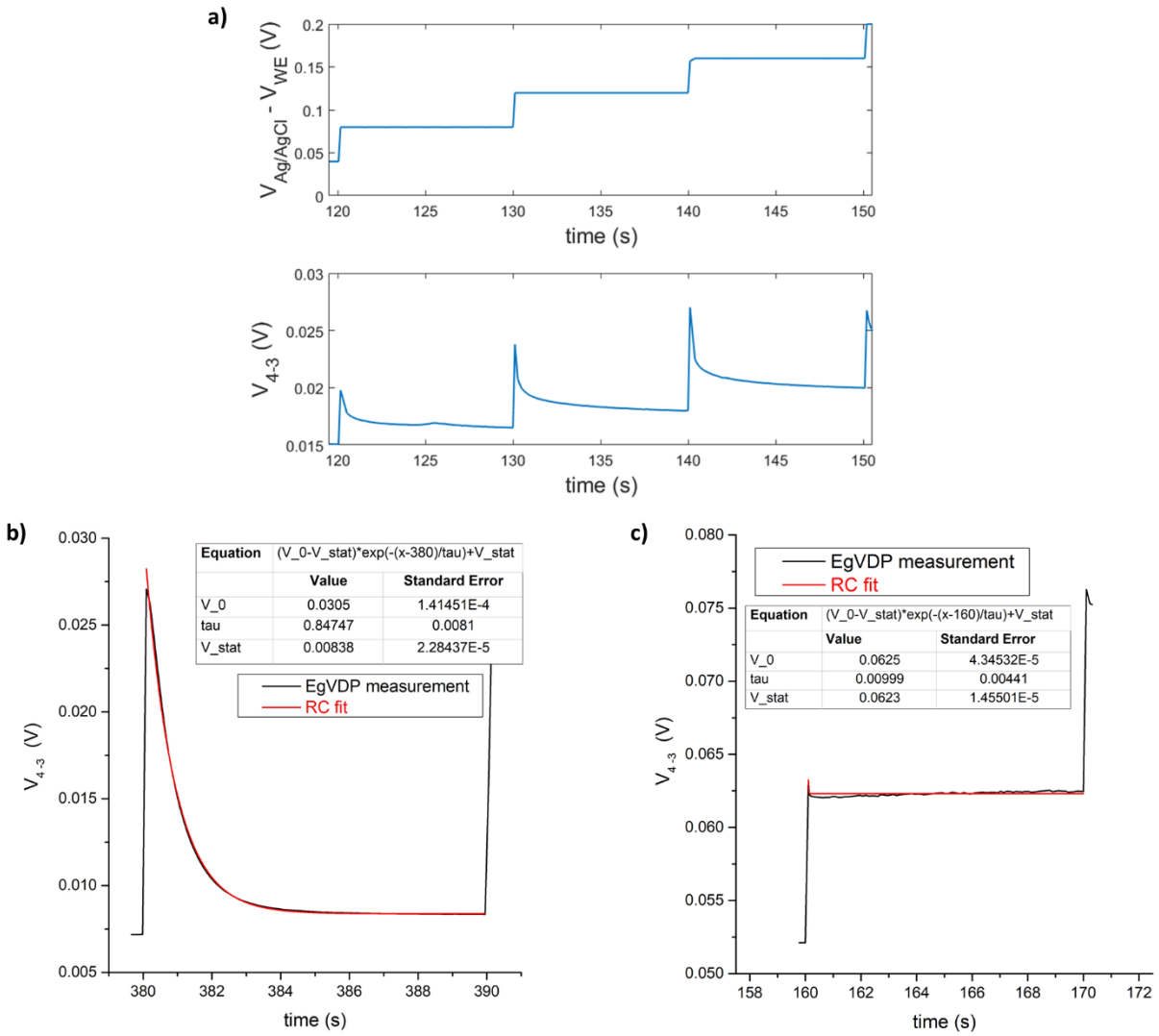

Figure 3.5.2: Analysis of EgVDP measurements in the time domain. **a)** Response of an EgVDP sample when voltage steps are applied in solution. Both $V_{sol} = V_{Ag/AgCl} - V_{WE}$ and the voltage drop between contacts 4 and 3 of the device (V_{4-3}) are plotted in function of time. **b)** and **c)** Transient response of a millimeter-sized **(b)** and of a microfabricated **(c)** EgVDP device during a voltage step (V_{sol} = 0.32 V). The injected currents between contacts 1 and 2 are respectively 1 µA **(b)** and 10 µA **(c).** Measurements were fitted with an equivalent RC circuit to extract the stationary voltage and the time constant.

3.5.2 PEDOT:PSS transport properties extracted from EgVDP measurements

Results obtained in the EgVDP measurement can be examined by applying Rolin's analysis [6] for gVDP method (see **sect. 1.4.2**) to extract the charge carrier mobility in PEDOT:PSS thin film. In particular, if we define the sheet conductance as $\sigma_s = R_s^{-1}$, **eq. 1.4.8** can be rewritten in this contest as

$$\sigma_S = \mu_p c|V_g - V_t| \qquad 3.5.2$$

where c is the capacitance per unit area of the sample, μ_p is the holes' mobility in PEDOT:PSS, V_g is the gate voltage and V_t is the threshold voltage. In particular, V_g is defined as the difference between the voltage applied in solution and half the voltage drop on the conductive channel of

the sample: $V_g = V_{sol} - V_{ch}/2$, where $V_{sol} \equiv V_{Ag/AgCl} - V_{WE}$ and $V_{ch} = |V_4 - V_3|/2 \equiv |V_4|/2$ in the HiF1LoF2HiS4LoS3 contact configuration. Eq. 3.5.2 was fitted to data in **Figure 3.5.3 a** and **b** respectively for millimeter-sized and miniaturized devices.
The experimental relation between the gate voltage and the sheet conductance is qualitatively consistent with the one expected from eq. 3.5.2. Anyway, when the gate voltage is high and the carrier concentration small, the two quantities are not linearly correlated. The non-linear tail cannot be included in Rolin's analysis, and therefore was not considered in this section.

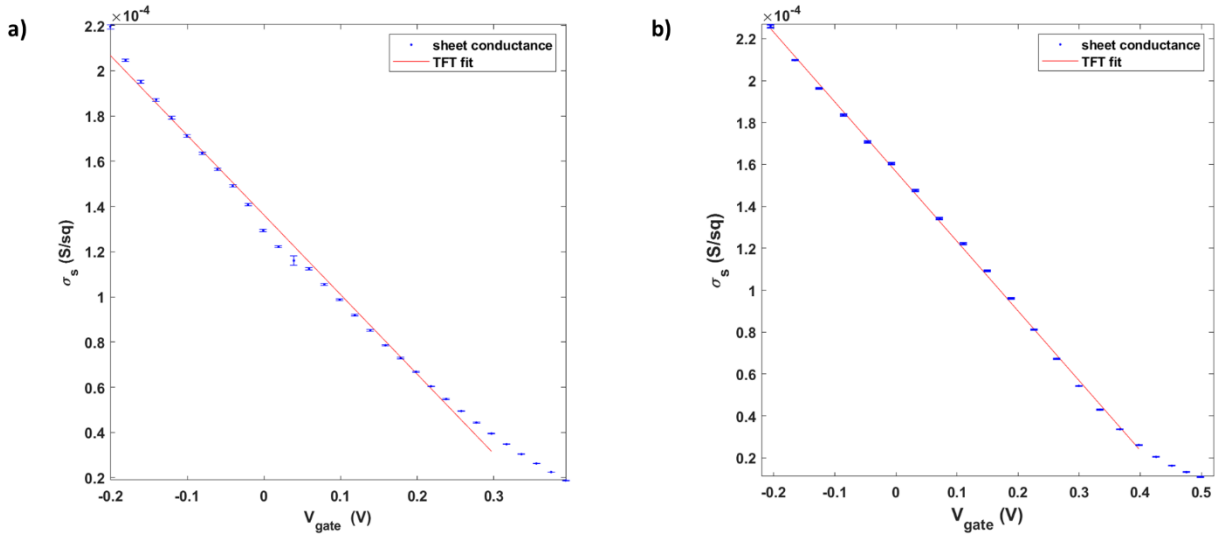

Figure 3.5.3: Quantitative analysis of EgVDP measurements. **(a)** Sheet conductance of a millimeter-sized EgVDP sample as a function of the gate voltage. Measurements have been fitted with eq. 3.1.1, obtaining $\mu_p = (0.97\pm0.03)$ $cm^2V^{-1}s^{-1}$ and $V_t = (0.41\pm0.02)$ V. The same analysis is repeated for miniaturized samples **(b)**, giving $\mu_p = (0.59\pm0.04)$ $cm^2V^{-1}s^{-1}$ and $V_t = (0.35\pm0.05)$ V.

From the fit slope and intercept, it is possible to calculate the holes' mobility and the threshold voltage. Results are reported in **Table 3.5.1** and **Table 3.5.2**.

Sample	μ_p ($cm^2V^{-1}s^{-1}$)	V_t (V)
1	0.23±0.02	0.41±0.02
2	0.45±0.02	0.40±0.02
3	0.97±0.03	0.41±0.02

Table 3.5.1: Results from EgVDP characterization of millimeter-sized samples.

Sample	μ_p ($cm^2V^{-1}s^{-1}$)	V_t (V)
1	0.59±0.04	0.35±0.05
2	0.749±0.013	0.470±0.011

Table 3.5.2: Results from EgVDP characterization of millimeter-sized samples.

CHAPTER 4: DISCUSSION

The main results obtained in the measurements are discussed in this chapter and compared with literature.
The EgVDP characterization has revealed to be an effective tool for the measurements of charge carrier mobility in PEDOT:PSS thin films, but its results are quite different with respect to two-contacts characterizations. For this reason, in the first part of this section, EgVDP and two-contacts measurements are compared to investigate the possible role of the contacts resistance during mobility extraction.
The second part of this section is focused on the analysis of charge accumulation in PEDOT:PSS. Measurement results from EIS are interpreted to investigate the origin of the large capacitance of hydrated PEDOT:PSS thin films.
Finally, charge transport properties of PEDOT:PSS are examined: the PEDOT:PSS density of state is investigated, and EgVDP measurements are analyzed by applying Tybrandt's model.

4.1 Comparison between EgVDP and two-contacts characterization

The charge carrier mobilities and the threshold voltages resulting from the experiments can be averaged to obtain a conclusive summary, which is reported in **Table 4.1**:

characterization method	$<\mu_p>(cm^2V^{-1}s^{-1})$	$<V_t>(V)$
EgVDP, millimeter-sized samples	0.55±0.03	0.41±0.02
EgVDP, microfabricated samples	0.67±0.02	0.42±0.05
Two-contacts linear transfer analysis	4.6±0.3	0.53±0.03
Two-contacts saturation transfer analysis	5.0±0.2	0.56±0.03

Table 4.1: Comparison between EgVDP and two-contacts characterization methods.

EgVDP characterizations of millimeter-sized and miniaturized samples give consistent results. The extracted threshold voltages are compatible within the experimental errors, while mobilities show a small discrepancy. This could be related to many different causes, such as the presence of parasitic charge transfer processes during measurements, which complicate the extraction of conductivity, or to small differences in temperature, which determines the carrier mobility in disordered organic semiconductors. [54]
On the other hand, the holes' mobility obtained from two-contacts measurements is about eight times higher. In this contest, μ_p was extracted by fitting the transfer characteristic of an OECT. Thin film transistors based on high-mobility organic semiconductors are often prone to contact problems that complicate the interpretation of their electrical characteristics and the extraction of important material parameters such as the charge carrier mobility.[6]
In particular, Liu et. al [55] asserted that mobility in transistors with resistive contact can be underestimated with the presence of the injection barrier, whereas mobility in transistors with gated Schottky contact can be overestimated by more than 10 times. Quantitative calculations reveal that the overestimation originates from the evolution of the injection barrier and band bending under the different gate field, which induces nonlinearly increased carrier concentration in the channel. Such an effect can occur even in long-channel devices, and it becomes more severe when using highly disordered semiconductors.

4.1.1 The effect of contact resistance on mobility measurements

In an ideal FET or TFT operating in linear regime, the drain current I_{DS} is totally determined by the channel resistance (R_{ch}).
The transfer curve can be written as

$$I_{DS} = \mu_0 c \frac{W}{L}[V_t - V_g + V_{DS}/2]V_{DS} \quad 4.1.1$$

Here, W and L are the channel width and length, respectively, c is the gate dielectric capacitance per unit area, μ_0 is the intrinsic carrier mobility and V_{DS} and V_g are the drain and gate voltages. The channel resistance is expressed as $R_{ch} = V_{DS}/I_{DS} = 1/[\mu_{lin} c \frac{W}{L}(V_t - V_g + V_{DS}/2)]$. The field-effect mobility μ_0 can be calculated by extracting the transconductance g_0:

$$\mu_0 = \frac{L}{WcV_{DS}} g_0 = \frac{L}{WcV_{DS}}\left[-\frac{V_{DS}}{(R_{ch})^2}\frac{\partial R_{ch}}{\partial V_g}\right] \quad 4.1.2$$

The above equation holds only when contact resistance $R_c = 0$ (the subscript 0 denotes zero R_c). In the case of nonzero R_c, $I_{DS} = V_{DS}/(R_{ch} + R_c)$, and g becomes

$$g = -\frac{V_{DS}}{(R_{ch} + R_{ch})^2}\left(\frac{\partial R_{ch}}{\partial V_g} + \frac{\partial R_c}{\partial V_g}\right) \quad 4.1.3$$

Hence, μ calculated by g can be overestimated if $(g - g_0) < 0$ or underestimated if $(g - g_0) > 0$. It can be derived that

$$g - g_0 < 0 \text{ when } \frac{\partial R_c}{\partial V_g} > \frac{\partial R_{ch}}{\partial V_g}\left[\left(2 + \frac{R_c}{R_{ch}}\right)\frac{R_c}{R_{ch}}\right] \quad 4.1.4$$

$$g - g_0 > 0 \text{ when } \frac{\partial R_c}{\partial V_g} < \frac{\partial R_{ch}}{\partial V_g}\left[\left(2 + \frac{R_c}{R_{ch}}\right)\frac{R_c}{R_{ch}}\right] \quad 4.1.5$$

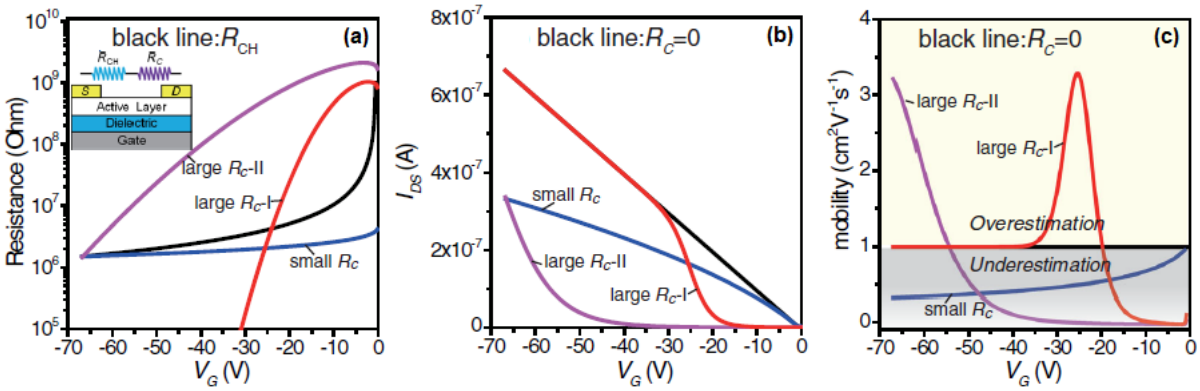

Figure 4.1.1: Under or overestimation of carrier mobility due to contact resistance (linear regime). Gate dependence of **(a)** resistance (R_c, R_{ch}), **(b)** drain current (I_{DS}), and **(c)** extracted field-effect mobility by Eq. 4.1.2 when setting μ_0 = 1 $cm^2V^{-1}s^{-1}$.

Thus, mobility is underestimated if R_c is much less V_g dependent than R_{ch}, i.e., with a resistive contact during gating operation (eq. 4.1.5). In comparison, the mobility is overestimated when the gate dependence of R_c overwhelms that of R_{ch} (eq. 4.1.4). This is especially true when R_c rapidly decreases to approach R_{ch} , which may occur with a gated Schottky contact.
To exemplify the meaning of Eq. 3.2.4 and 3.2.5, Liu calculated the behavior of I_{DS} and μ in different cases, as reported in **Figure 4.1.1**.
Specifically, when contact resistance R_c decreases with gate voltage more slowly than channel resistance R_{ch} ("small R_c" case in Fig. 4.1.1), the voltage drop at the contact increases with V_g, leading to an underestimation of mobility. When R_c is much higher but also decreases faster than R_{ch} with V_g ("large RC-I "case), the effect is rather convoluted and leads to an initial underestimation of mobility followed by an overestimation with a peak value. It is interesting to note that, while the peak is clearly an artifact, beyond this point, the mobility extraction is actually quite accurate. Moreover, depending on the actual values of R_c ("large R_c-II" case), the peak value may exist beyond the actual measurement range, so that only a mobility which superlinearly increases with voltage would be measured.
The linear transfer curves measured with 2-contacts devices are qualitatively similar to the "large R_c-I" case of Liu's analysis (see Fig. 3.2.1 b), and the slope of the curve visibly changes when the voltage applied in solution is lower than 0 V. For this reason, we can hypothesize that the analysis conducted in sec. 3.1.5 overestimates the film mobility because of contact resistance effects. Therefore, in **Figure 4.1.2** the two different regions of the transfer curve are linearly fitted and Bernard's model (eq. 3.4.1) is applied to calculate the mobility. The obtained results are respectively $\mu_{p,1}$ = (4.6±0.3) $cm^2V^{-1}s^{-1}$ when 0 V < V_{sol} < 0.6 V (as reported in Table 3.2.1) and $\mu_{p,2}$ = (0.93±0.02) $cm^2V^{-1}s^{-1}$ when V_{sol} < 0V. According to Liu's work, this last value should correspond to the contact-independent holes' mobility. Anyway, we can only consider $\mu_{p,2}$ as an estimate of the real value, because the analysis is conducted only for a small number of measured values. Experiments performed in a wider range of negative V_{sol} could confirm this result.

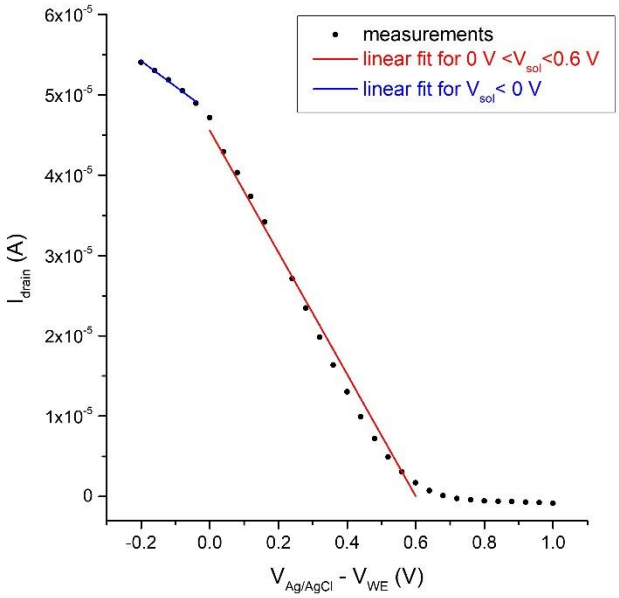

Figure 4.1.2: Analysis of the transfer curve of a two-contacts sample. The plot clearly shows two different slopes. The holes' mobility μ_p = (4.6±0.3) $cm^2V^{-1}s^{-1}$ extracted in section 3.4 (red fit line) may be overestimated due to contact resistance effect. A more accurate value can be evaluated from the slope of the blue fit line, that is μ_p = (0.93±0.02) $cm^2V^{-1}s^{-1}$.

4.1.2 Lateral ion transport in OECTs

According to Liu's analysis, results obtained in **Fig. 4.1.2** suggest the presence of a rectifying contact at drain terminal. Such a hypothesis is not reliable, because many studies demonstrate that the PEDOT-gold contact is ohmic [56]. However, contact resistance effects were proposed earlier to explain the strong non-monotonic dependency of the transconductance on the gate potential observed in most OECT reports. [57]

A possible explanation of this phenomenon is provided by Kaphle et. al. [58]. In their work, scientists argue that current capacitive OECT models neglect lateral ion currents in the transistor channel and therefore fail to describe the equilibrium state of the devices. Lateral ion currents lead to an accumulation of ions at the drain contact, which significantly alters the transistor behavior.

To demonstrate its hypothesis, Kaphle measured the threshold voltage of an OECT in linear regime at different drain and gate potentials and found a systematic dependence on the applied voltage. According to Bernard's model for OECTs [53], this parameter should be only defined by design parameters only ($V_t = ep_0/C_g$, where C_g is the gate capacitance and p_0 the density of holes without injected cations, which is supposed to be proportional to the density of sulphonate (PSS^-) groups) and should not vary with the applied potential. This failure of the model to consistently describe the potential along the transistor channel was interpreted as an incorrect description of the device operation. In Bernard's model, the density of cations is calculated by the gate capacitance, that is, using

$$p_{ion}(x) = \frac{C_g}{e}\left[V_g - \phi(x)\right] \tag{4.1.6}$$

where p_{ion} is the ion concentration along the conducting channel, , V_g the gate potential and $\phi(x)$ the channel potential. This approach implicitly assumes that cations entering the channel from the electrolyte do not move laterally, which, however, is in contradiction with the moving front experiments by Stavrinidou [59] et al. showing that cations move efficiently inside the PEDOT:PSS. Considering the considerable ion mobility inside PEDOT:PSS, cations do not only move vertically from the gate electrolyte into the channel, but also move laterally from source to drain under the influence of the lateral source–drain field.

A 2D drift-diffusion simulation was developed by Kaphle to obtain the steady-state carrier distribution inside the transistor channel. Poisson's equation and the continuity equations for cations and holes can be written as

$$\nabla^2\phi(x,y) = \frac{e}{\varepsilon\varepsilon_0}\left[-p(x,y) - p_{ion}(x,y) + p_0(y) + N_0(y)\right] \tag{4.1.7}$$

$$\nabla \boldsymbol{j_p} = 0 \tag{4.1.8}$$

$$\nabla \boldsymbol{j_{p,ion}} = 0 \tag{4.1.9}$$

where N_0 is the anion concentration in the electrolyte.

The simulation setup and results are reported respectively in **Figure 4.1.3 a** and **b**. The cation concentration increases exponentially towards the drain contact:

$$p_{ion}(x) = N_0 exp\left[\frac{V_g - \phi(x)}{V_t}\right] \tag{4.1.10}$$

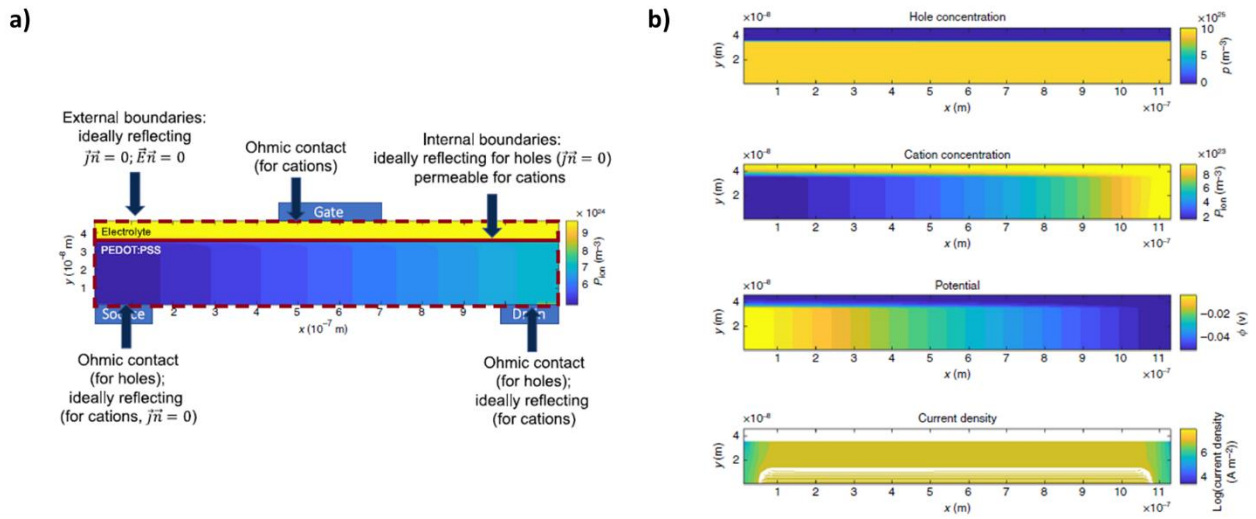

Figure 4.1.3: Kaphle's simulation for OECT including lateral ion motion. The applied drain and gate voltages are equal to $-2V_t$. **(a)** Setup and boundary conditions. **(b)** Resulting spatial distribution of hole and ion concentrations, electrical potential and current density.

Following the results of the 2D model, the potential within the channel (i.e., for all measurements along the channel but excluding the potential applied to the drain electrode) can be fitted by a linear function. An optimized fit is shown in **Fig. 4.1.4 a.** Kaphle extrapolated the linear fit of the channel potential to the drain electrode, which allowed to quantify the additional potential drop caused by the accumulation of ions at the drain ΔV_{ion}. **Fig. 4.1.4 b** plots this potential drop at the drain contact with respect to the different drain and gate bias.
The additional potential drop can be formally modeled by a contact resistance: $R_c = \Delta V_{ion}/I_{drain}$.

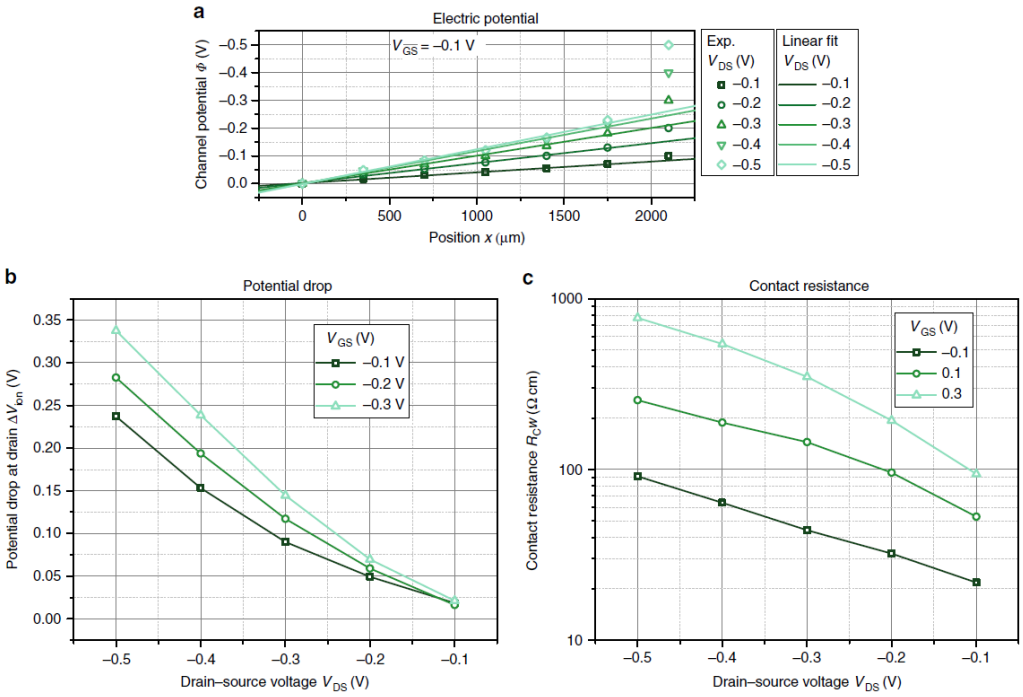

Figure 4.1.3: Describing ion accumulation by contact resistances. **(a)** Channel potential profile at the gate potential V_{gate} = −0.1 V. The lines are linear fits. **(b)** Potential drop at drain contact for different gate and drain voltages. **(c)** Contact resistance at varying gate and drain voltages. [6]

In **Fig. 4.1.4 c** the resulting contact resistance for different drain and gate voltages is plotted. It is found that the contact resistance is exponentially increasing with drain and gate voltages, which is in line with an earlier report. [57] Therefore, Bernard's model can be seen as an approximation of the device at low voltages. For larger voltages, the observed redistribution of cations in the channel to reach an equilibrium state can be included by a gate potential dependent contact resistance. It has furthermore to be stressed that the contact resistance as described here does not represent a contact resistance in the conventional sense, that is, it does not describe an inhibition in the carrier injection. Rather, it describes the effects of ion accumulation at the drain contact, caused by ion currents inside the transistor channel, and the additional potential drop by the accompanying space charge region.

Kaphle's argument can be applied for a qualitative interpretation of the OECT characteristics in **Figure 4.1.2**. According to Liu's analysis in **sect. 4.1.1,** the transfer curve assumes different slopes when the contact resistance is much higher but also decreases faster than the channel resistance with V_g. This leads to an initial overestimation of mobility. Because the ion accumulation at the drain contact can be modeled with a contact resistance which exponentially decreases with decreasing gate voltage, we can assume that lateral ion transport complicates the mobility extraction from OECT characteristics and is responsible of the mobility overestimation in two-contacts measurements. Further experiments are needed to verify this hypothesis.

4.2 Analysis of charge accumulation in PEDOT:PSS thin films

Charge accumulation in hydrated PEDOT:PSS thin films was studied by measuring the electrical capacitance of the PEDOT:PSS-electrolyte interface. The average volumetric capacitance was calculated to be (25±4) F/cm^3, which is consistent with values found in literature [60].

The PEDOT:PSS-electrolyte interface capacitance resulted to be independent from the voltage applied in solution ($V_{sol} = V_{Ag/AgCl} - V_{WE}$). Despite measurements were performed only in a limited potential range ($-0.2\ V < V_{sol} < 0.4\ V$), this result can be significative to investigate the origin of the PEDOT:PSS capacitance.

The semiconductor-electrolyte interface capacitance is typically voltage-dependent and can be compared to a metal-semiconductor interface. [61] Let us consider a n-type semiconductor with Fermi level E_F, put in contact with an electrolyte, which is a conductor with a defined vacuum level $E_{vac,\,el}$ (**Fig. 4.2 a**). The application of a voltage V_{sol} modifies $E_{vac,\,el}$, causing the charging of the interface and the bending of the energetic levels of the semiconductor. The flat-band potential V_{fb} is defined as the value of V_{sol} at which the vacuum levels of both the semiconductor and the electrolyte coincide (**Fig. 4.2 c**). When $V_{sol} < V_{fb}$, the interfacial region of the semiconductor is depleted from charge carriers (**Fig. 4.2 b**). This has the effect of charging the semiconductor positively, and since semiconductor carrier densities are much lower than those in solution, the diffuse charge in the semiconductor (space charge region) is counterbalanced essentially by a sheet of charge in the electrolyte. Therefore, an electrical capacitance is generated in correspondence of the 2-dimesional interface. This phenomenon is called Mott-Schottky effect, and the interface capacitance depends strongly on the applied voltage ($C^{-2} \propto (V_{fb} - V_{sol})$).

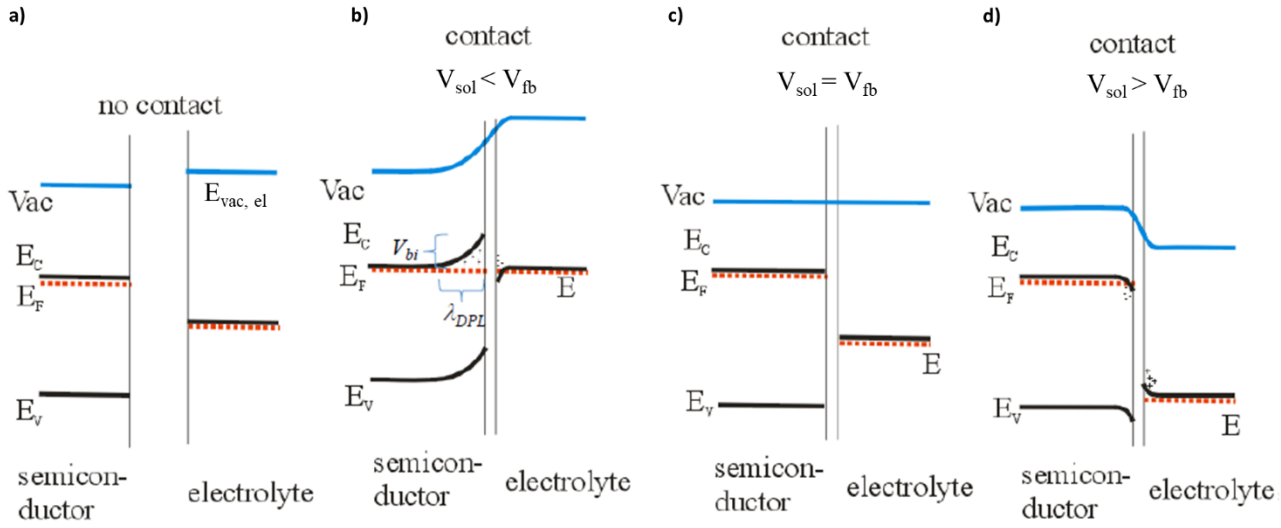

Figure 4.2: Electrolyte-semiconductor interface. **(a)** Schematic of an n-type semiconductor showing the valence and conduction bands (with energies E_V and E_C, respectively), Fermi level (E_F) and vacuum levels. **(b)** The application of V_{sol} lower than the flat band potential generates a depletion region in the semiconductor and an interface capacitance. **(c)** Situation when the semiconductor is at its flat-band potential. **(d)** Accumulation of carriers in the semiconductor when $V_{sol} > V_{fb}$. The Mott-Schottky effect is absent in this regime.

The Mott-Schottky effect was not observed in this work. We can hypothesize that the capacitance of hydrated PEDOT:PSS thin films in the voltage range of measurements is dominated by an intrinsic contribution. In **sect. 1.3.2**, we attributed the origin of the PEDOT:PSS volumetric capacitance to the electrical double layers formed along the interfaces between the electronic (PEDOT) and ionic (PSS) phases. [34] The origin of such a capacitance is morphological, and independent from the applied voltage.
The two-phases separation inside PEDOT:PSS layers determines the charge accumulation processes in the blend. Consequently, as emphasize by Tybrandt, [1] two distinct electrical potentials are established in the active layer, one potential inside the PSS phase, and one inside the PEDOT phase, and this determines the charging of the interface. Differently form the Mott-Schottky capacitance, which regards only the 2-dimentional interface between the film surface and the electrolyte, the interface between the PEDOT and the PSS phase is diffused, and electrical double layers are formed in the whole film volume.

4.3 Analysis of charge transport in PEDOT:PSS

Charge transport and optical properties of a material are determined by its energy spectrum, also called the density of states (DOS). [62] Reliable first-principles calculations of the DOS in disordered organics are not yet known. Therefore, the only way to determine the DOS is to compare experimental data with the appropriate theory using some trial DOS functions g(ε), aiming at the best agreement between experimental and theoretical results.
Tybrandt's model couples the electric double layer residing at the PEDOT-PSS interface with the chemical potential ε_F of holes in PEDOT. The changes in the latter have a significant impact at low carrier concentration and depend on the shape of the density of states of PEDOT. Tybrandt assumed in his work a Gaussian density of states (eq. 1.3.8) , but different DOS could provide a different relation between p and ε_F which fits better with experiments. In disordered organic semiconductors, charge transport occurs via incoherent hopping of carriers (electrons or holes) between strongly localized states. [63] It is well known that in some of their inorganic counterparts, such as amorphous Si:H or chalcogenides, the DOS is purely exponential:

$$g(\varepsilon) = \frac{N_t}{\sigma} exp\left(-\frac{\varepsilon}{\sigma}\right) \qquad 4.3.1$$

where N_t is the total number of hopping sites, σ is a constant which is a measure of the energetic disorder and the energy ε is counted positively downwards from some reference level set to zero. [62] The distribution of carriers in thermal equilibrium is described by the product g(ε)*f(ε)*, where g(ε) is the DOS and *f (ε)* is the Fermi distribution

$$f(\varepsilon) = \frac{1}{1 + exp\left(\frac{\varepsilon - \varepsilon_F}{k_b T}\right)} \qquad 4.3.2$$

Transport in disordered organic semiconductors is dominated by thermally activated transitions of charge carriers towards the energy level ε_t, traditionally called the transport energy, situated far above the energy region occupied by carriers. [63] This feature is qualitatively similar for all steeply energy-dependent DOS functions. If we assume a carrier occupying a level with energy ε_i, we can calculate the transport energy by finding the most likely targeted energy in a hop from the level ε_i upwards in energy. It can be shown that ε_t does not depend on the initial energy ε_i and is therefore a universal quantity for a given set of system parameters (N_t, T, σ) . Therefore, charge carriers situated at energies below ε_t will most probably be activated to energies in the vicinity of ε_t and carriers above ε_t will most probably fall down in energy. The position of the transport energy depends slightly on the shape of the DOS. What is, however, qualitatively different in the case of Gaussian DOS, as compared to the case of the exponential DOS, is the kind of thermal distribution of carriers along the energy spectrum of the system. In the exponential DOS, the maximum of the carrier distribution g(ε)*f(ε)* at $k_bT < \sigma$ is in close vicinity of the concentration-dependent chemical potential (or Fermi energy) $\varepsilon_F(p)$, as illustrated schematically in **Figure 4.3.1 a**. Mobility, determined by carrier activation from $\varepsilon_F(p)$ towards ε_t, is therefore always a function of p.

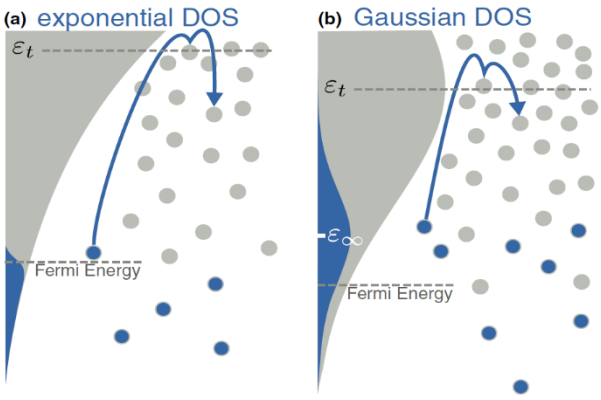

Figure 4.3.1: Schematic picture of the equilibrium carrier distribution in the exponential **(a)** and Gaussian **(b)** DOS. Occupied states are marked blue.

In the Gaussian DOS, on the contrary, most carriers at low p are distributed not around the Fermi level, but are instead situated around the so-called equilibration energy ε_∞, identified with the average carrier energy $\varepsilon_\infty = -\sigma^2/(k_bT)$. This situation, with most carriers occupying in thermal equilibrium energy levels far above the Fermi level, is counter-intuitive. It occurs because the number of states in the Gaussian DOS increases above the Fermi level at a much steeper rate than the decrease of the occupation probability described by the Fermi function. The distribution of carriers in the Gaussian DOS at low p is illustrated schematically in **Figure 4.3.1 b**. In such a case, transport in the Gaussian DOS is due to carrier transitions via energy levels in the range between ε_∞ and ε_t. Neither of these energies depend on the concentration of carriers. Furthermore, the occupation numbers of states in the range between ε_∞ and ε_t is very low ($f(\varepsilon) << 1$) and the carriers can be considered as independent from each other (filling of states in the range between ε_∞ and ε_t can be neglected). Therefore, the carrier mobility in the Gaussian DOS at low p does not depend on p, which is in striking contrast to the situation in the exponential DOS, where carrier mobility depends on p at all p values.

The analysis of EgVDP measurements reported in **Fig. 3.5.3** clearly indicate a linear dependence between the sheet conductivity and the gate voltage when $V_{gate} < V_t$. In such a condition, we can assume the charge carrier mobility as constant, independently from their concentration p. Otherwise, p should be an unknown function of the gate voltage which exactly compensates the non-linearity introduced by a non-constant mobility. This observation should exclude a purely exponential DOS for PEDOT:PSS, because we found a concentration range where mobility is constant independently from p. Anyway, we cannot exclude the presence of an exponential tail in the Gaussian DOS, which was observed in other organic semiconductors at very low carrier concentrations. [64] This aspect cannot be investigated in this work due to the limited variation in carrier density (10^{18} -10^{20} cm^{-3}).

In order to derive a quantitative analysis of the DOS shape from EgVDP measurements we apply the approximation of a low concentration regime. In the limit of small p, carriers can be considered essentially independent of each other, and the Fermi statistics (eq. 4.3.2) can be replaced by the Boltzmann statistics: [36]

$$f_{Boltz}(\varepsilon) = exp\left(-\frac{\varepsilon - \varepsilon_F}{k_bT}\right) \qquad 4.3.3$$

If we consider an exponential DOS, we can find an analytical expression for the Fermi level in function of p. In the Boltzmann's limit, the equation

$$p = \int_0^{+\infty} g(\varepsilon) \cdot f_{Boltz}(\varepsilon)\, d\varepsilon = \int_0^{+\infty} \frac{N_t}{\sigma} exp\left(-\frac{\varepsilon}{\sigma}\right) \cdot exp\left(-\frac{\varepsilon - \varepsilon_F}{k_b T}\right) d\varepsilon \qquad 4.3.4$$

can be analytically solved, giving

$$\varepsilon_F(p) = k_b T \cdot ln\left[\frac{(\sigma + k_b T)}{N_t k_b T} \cdot p\right] = k_b T \cdot ln(p) + B_{exp} \qquad 4.3.5$$

where B_{exp} is a constant depending on the DOS parameters. Eq. 4.3.5 is perfectly analogous to eq. 1.3.10, obtained for a Gaussian density of states. When the carriers' concentration is small, the dependence between ε_F and p has the same form for both the exponential and the Gaussian DOS.

The analysis of the EgVDP measurements conducted in section 3.5 extracts the contact-independent charge carrier mobility by fitting the linear regime of a thin film transistor (TFT). This approach, introduced by Rolin [6] for gated van der Pauw's characterization, has revealed to be effective, but does not consider the low carrier concentration regime observed in the measurements. Such a condition is particularly relevant for this work because the relation between σ_s and V_g is not linear, and holes' mobility cannot be simply assumed as constant, but could depend on the holes' concentration. Therefore, the study of low concentration regimes is crucial to investigate the charge transport processes in PEDOT:PSS thin films.

The first step required for a more-in-depth analysis of EgVDP measurements is the calculation of holes' concentration in PEDOT:PSS. By applying Tybrandt's model (see sect. 1.3.3), we can write

$$p/C_V + k_b T\, ln(p)/e\ + B - W_{AgCl}/e = -V_g \qquad 4.3.6$$

where C_V is the volumetric capacitance of PEDOT:PSS, $W_{Ag/AgCl}$ is the work function of the silver-silver chloride reference electrode and B a constant proportional to the energetic width of the PEDOT:PSS density of states. As in sect 3.5, the gate voltage V_g is defined as the difference between the voltage applied in solution and half the voltage drop on the conductive channel of the sample: $V_g = V_{sol} - V_{ch}/2$, where $V_{sol} \equiv V_{Ag/AgCl} - V_{WE}$ and $V_{ch} = |V_4 - V_3|/2 \equiv |V_4|/2$ (in the HiF1LoF2HiS4LoS3 contacts configuration). Eq. 4.4.1 was numerically solved to calculate the carrier concentration in function of the gate voltage in EgVDP measurements. Results are compared with the purely capacitive model in **Figure 4.3.2 a**.

The sheet conductivity σ_s and the holes' concentration p (expressed in m^{-3}) are related by

$$\sigma_s = te\mu_p\, p \qquad 4.3.7$$

where t is the film thickness and e the elementary charge. The EISs of miniaturized EgVDP samples (**Fig. 3.3.2 a**) clearly show the presence of parasitic charge transfer processes between the film and the electrolyte. The reasons of such a charge leakage are unknown. Anyway, we can assume that the leakage produced a constant and systematic error a during sheet conductivity measurements, and define the effective sheet conductivity σ_s^{eff} as a sum between an intrinsic term σ_s and the leakage contribution:

$$\sigma_s^{eff} = \sigma_s + a = te\mu_p p + a \qquad 4.3.8$$

Hence, eq. 4.4.1 can be rewritten as

$$\frac{(\sigma_s^{eff} - a)}{te\mu_{p0}C_v} + \frac{k_bT}{e}\, ln\left[\frac{(\sigma_s^{eff} - a)}{te\mu_{p0}C_v}\right] + B - W_{AgCl}/e = -V_g \qquad 4.3.9$$

where the holes' mobility μ_{p0} is considered to be constant even in the low concentration regime. Eq. 4.4.4 was fitted to experimental measurements. Results are presented in **Figure 4.3.2 b**. The "corrected" Tybrandt's model reproduces the EgVDP measurements in the whole potential range. The extracted mobility is μ_{p0} = (0.862±0.003) $cm^2V^{-1}s^{-1}$, while B = (4.17±0.02) V and a = (8.0±0.3) µS/sq.
The goodness of the fit suggests that the mobility is constant even in the non-linear region. Anyway, the leakage contribution *a* becomes significative in that concentration regime (see inset in **Fig 4.3.2 b**). The introduction of a constant term which compensates the non-idealities of the samples improves the agreement between theory and experiments, but may be only a reductive approximation. Therefore, measurement should be repeated with new microfabricated devices in which leakage effects are negligible.

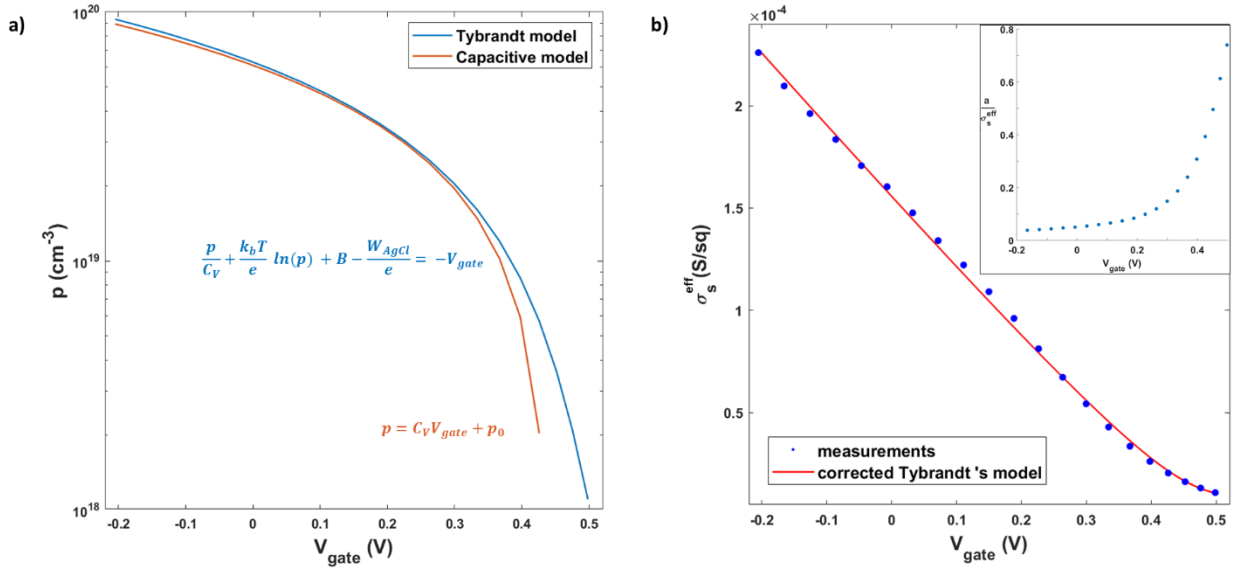

Figure 4.3.2: Application of Tybrandt's model in EgVDP measurements. **(a)** Calculation of the hole concentration in the conductive channel of a miniaturized EgVDP sample. Tybrandt's model is compared with the capacitive model. The second one cannot be applied in the low-concentration regime, as it predicts negative concentrations (which are not plotted in log scale). **(b)** Fitting of the sheet conductance measurements with the "corrected" Tybrandt's model, which contains the systematic leakage contribution *a*. Inset: ratio between *a* and σ_s^{eff} as a function of the gate voltage.

Conclusions

The objective of this Thesis is the study of charge transport and accumulation in degenerately doped semiconducting polymers with mixed ionic and electronic conductivity. The carrier density and mobility were measured in the hydrated conducting polymer–polyelectrolyte blend PEDOT:PSS, one of the most promising materials in the field of Organic Bioelectronics. A 4-wire contact-independent characterization technique was introduced for this scope, the electrolyte-gated van der Pauw (EgVDP) method. In contrast to methods described so far in literature, the EgVDP methods measures the semiconductors sheet resistance in function of the potential applied to the electrolyte. The sheet resistance is not affected by possible contact resistance effects and therefore provides a more reliable characterization of transport properties in contrast to normally applied two-contact transistor characterizations. Furthermore, electrochemical impedance spectroscopy (EIS) was applied to characterize charge accumulation in PEDOT:PSS thin films immersed in an electrolyte.
Both measurement techniques were applied to macro (film area 35 mm^2) and micro-structured (film area 0.25 mm^2) PEDOT:PSS thin film devices. A photolithography technique was developed to achieve the micrometric patterns of the semiconducting film and of the contacting electrodes. Micro-structured two-contacts devices were fabricated for 2-point-probe characterization. The obtained results were compared to EgVDP measurements to study the influence of the contact resistance on the extraction of the charge carrier mobility in organic electrochemical transistors.

The EgVDP characterization combined with the EIS was demonstrated to be an effective tool for the measurements of charge carrier mobility in PEDOT:PSS thin films. Experiments performed with different devices gave consistent results, and the average holes' mobility resulted to be $<\mu_p>$ = (0.67±0.02) $cm^2V^{-1}s^{-1}$. This value is quite different with respect to the one extracted from the two-contacts devices, $<\mu_p>$ = (4.6±0.3) $cm^2V^{-1}s^{-1}$, and we hypothesized that contact resistance effects resulted in an overestimation of mobility. In particular, we found the lateral ion transport in the OECT channel as a possible explanation of such an effect. In fact, ion accumulation at the drain contact creates a gate-dependent Schottky barrier which complicates the extraction of mobility in OECTs. Further experiments will be performed on two-contacts devices to verify this hypothesis.

Charge accumulation processes in CP-PE blends were studied by measuring the PEDOT:PSS-electrolyte interface capacitance. The latter revealed to be independent from the voltage applied in solution. Mott-Schottky effect was not observed in the potential range of measurements. Such a result confirmed the hypothesis that the capacitance of hydrated PEDOT:PSS thin films is dominated by an intrinsic contribution, related to the separation between the electronic (PEDOT) and ionic (PSS) phases in the blend. The origin of such a capacitance is morphological, and independent from the applied voltage. Differently from the Mott-Schottky capacitance, which regards only the 2-dimentional interface between the film surface and the electrolyte, the interface between the PEDOT and the PSS phase is diffused, and electrical double layers are formed in the whole film volume.

Charge transport properties of PEDOT:PSS were investigated by applying an extended drift-diffusion model (Tybrandt's model) to analyze the non-linear regime of EgVDP measurements. Such condition was of particular interest to find a possible dependence of mobility on the carriers' concentration, which is related to the material density of states (DOS). The analysis extracted a constant mobility in the whole measurement range (μ_p = (0.862±0.003) $cm^2V^{-1}s^{-1}$). This result suggested a Gaussian DOS for PEDOT:PSS, but the presence of possible exponential tails at low concentrations could not be observed because of the limited variation in carrier density (10^{18} -10^{20} cm^{-3}). Moreover, charge leakage processes

between the film and the electrolyte had a significant impact on measurements in low concentration regimes. The non-ideality of the sample were probably related to some anomaly during the fabrication process. Therefore, new microfabricated samples will be tested to clarify the latest results and confirm our thesis.

Bibliography

1. Tybrandt, K., Zozoulenko, I. V. & Berggren, M. Chemical potential-electric double layer coupling in conjugated polymer-polyelectrolyte blends. *Sci. Adv.* **3**, (2017).
2. Wang, Y. Research progress on a novel conductive polymer-poly(3,4-ethylenedioxythiophene) (PEDOT). *J. Phys. Conf. Ser.* **152**, 0–10 (2009).
3. Wang, Y. *et al.* A highly stretchable, transparent, and conductive polymer. *Sci. Adv.* (2017).
4. Rivnay, J. *et al.* Structural control of mixed ionic and electronic transport in conducting polymers. *Nat. Commun.* (2016).
5. Yeung, S. Y., Gu, X., Tsang, C. M., Tsao, S. W. & Hsing, I. ming. Engineering organic electrochemical transistor (OECT) to be sensitive cell-based biosensor through tuning of channel area. *Sensors Actuators, A Phys.* (2019).
6. Rolin, C. *et al.* Charge carrier mobility in thin films of organic semiconductors by the gated van der Pauw method. *Nat. Commun.* **8**, (2017).
7. Mantione, D., del Agua, I., Sanchez-Sanchez, A. & Mecerreyes, D. Poly(3,4-ethylenedioxythiophene) (PEDOT) derivatives: Innovative conductive polymers for bioelectronics. *Polymers* (2017).
8. Malliaras, G. G. Organic bioelectronics: A new era for organic electronics. *Biochimica et Biophysica Acta - General Subjects* (2013).
9. Prentki, M. *et al.* Rapid mobilization of Ca2+ from rat insulinoma microsomes by inositol-1,4,5-trisphosphate. *Nature* (1984).
10. Berggren, M. & Richter-Dahlfors, A. Organic bioelectronics. *Adv. Mater.* (2007).
11. Thery, M. *et al.* From the Cover: Anisotropy of cell adhesive microenvironment governs cell internal organization and orientation of polarity. *Proc. Natl. Acad. Sci. USA* (2006).
12. Nelson, C. M., VanDuijn, M. M., Inman, J. L., Fletcher, D. A. & Bissell, M. J. Tissue geometry determines sites of mammary branching morphogenesis in organotypic cultures. *Science (80-.).* (2006).
13. Simon, D. T., Gabrielsson, E. O., Tybrandt, K. & Berggren, M. Organic Bioelectronics: Bridging the Signaling Gap between Biology and Technology. *Chemical Reviews* (2016).
14. Rivnay, J. & Malliaras, G. G. The Rise of Organic Bioelectronics. (2014).
15. Hamedi, M., Forchheimer, R. & Inganäs, O. Towards woven logic from organic electronic fibres. *Nat. Mater.* (2007).
16. Rivers, T. J., Hudson, T. W. & Schmidt, C. E. Synthesis of a novel, biodegradable electrically conducting polymer for biomedical applications. *Adv. Funct. Mater.* (2002).
17. Mortimer, R. J., Dyer, A. L. & Reynolds, J. R. Electrochromic organic and polymeric materials for display applications. *Displays* (2006).
18. Smela, E. Conjugated polymer actuators. *MRS Bull.* (2008).
19. Jenkins, A. D., Stepto, R. F. T., Kratochvíl, P. & Suter, U. W. Glossary of basic terms in polymer science (IUPAC Recommendations 1996). *Pure Appl. Chem.* (1996).

20. Martínez-Duart, J. M., Martín-Palma, R. J. & Agulló-Rueda, F. The Physics of Low-Dimensional Semiconductors. in *Nanotechnology for Microelectronics and Optoelectronics* (2006).

21. Peierls, R. E. *Quantum Theory of Solids*. *Quantum Theory of Solids* (2007).

22. Elschner, A., Kirchmeyer, S., Lövenich, W., Merker, U. & Reuter, K. *PEDOT: Principles and applications of an intrinsically conductive polyme*. *PEDOT: Principles and Applications of an Intrinsically Conductive Polymer* (2010).

23. Heywang, G. & Jonas, F. Poly(alkylenedioxythiophene)s - New, very stable conducting polymers. *Adv. Mater.* (1992).

24. Dawydoff, W., Linow, K. -J & Philipp, B. Bildungsweise, Strukture und Anwendungsmöglichkeiten von Komplexen zwischen Polyelektrolyten und ionischen Farbstoffen (Literaturübersicht) Teil II: Komplexe zwischen anionischen Polymeren und kationischen Farbstoffen. *Acta Polym.* (1991).

25. Krebs, F. C. Fabrication and processing of polymer solar cells: A review of printing and coating techniques. *Solar Energy Materials and Solar Cells* (2009).

26. Okuzaki, H., Suzuki, H. & Ito, T. Electromechanical properties of poly(3,4-ethylenedioxythiophene)/Poly(4- styrene sulfonate) films. *J. Phys. Chem. B* (2009).

27. Gustafsson, J. C., Liedberg, B. & Inganäs, O. In situ spectroscopic investigations of electrochromism and ion transport in a poly (3,4-ethylenedioxythiophene) electrode in a solid state electrochemical cell. *Solid State Ionics* (1994).

28. Volkov, A. V. *et al.* Understanding the Capacitance of PEDOT:PSS. *Adv. Funct. Mater.* **27**, (2017).

29. Khodagholy, D. *et al.* NeuroGrid: Recording action potentials from the surface of the brain. *Nat. Neurosci.* (2015).

30. Jonsson, A. *et al.* Therapy using implanted organic bioelectronics. *Sci. Adv.* (2015).

31. Wang, X., Shapiro, B. & Smela, E. Development of a model for charge transport in conjugated polymers. *J. Phys. Chem. C* **113**, 382–401 (2009).

32. Wang, X. & Smela, E. Color and volume change in PPy(DBS). *J. Phys. Chem. C* (2009).

33. Ariza, M. J. & Otero, T. F. Ionic diffusion across oxidized polypyrrole membranes and during oxidation of the free-standing film. *Colloids Surfaces A Physicochem. Eng. Asp.* (2005).

34. Volkov, A. V. *et al.* Understanding the Capacitance of PEDOT:PSS. *Adv. Funct. Mater.* (2017).

35. Liu, C. *et al.* A unified understanding of charge transport in organic semiconductors: The importance of attenuated delocalization for the carriers. *Mater. Horizons* (2017).

36. Sharma, A. & Sheinman, M. Analytical approximation for chemical potential in organic materials with Gaussian density of states. *J. Phys. D. Appl. Phys.* **46**, (2013).

37. Lundstrom, M. Fundamentals of Carrier Transport, 2nd edn. *Meas. Sci. Technol.* (2002).

38. Romele, P., Ghittorelli, M., Kovács-Vajna, Z. M. & Torricelli, F. Ion buffering and interface charge enable high performance electronics with organic electrochemical transistors.

Nat. Commun. **10**, (2019).

39. Arkhipov, V. I., Emelianova, E. V., Heremans, P. & Bässler, H. Analytic model of carrier mobility in doped disordered organic semiconductors. *Phys. Rev. B - Condens. Matter Mater. Phys.* (2005).

40. Kokil, A., Yang, K. & Kumar, J. Techniques for characterization of charge carrier mobility in organic semiconductors. *Journal of Polymer Science, Part B: Polymer Physics* (2012).

41. Braga, D. & Horowitz, G. High-Performance organic field-effect transistors. *Advanced Materials* (2009). doi:10.1002/adma.200802733

42. Simonetti, O., Giraudet, L., Maurel, T., Nicolas, J. L. & Belkhir, A. Organic transistor model with nonlinear injection: Effects of uneven source contact on apparent mobility and threshold voltage. *Org. Electron.* (2010).

43. Pauw, L. J. van der. Philips Research. *Philips Res. Reports* **13**, 1–9 (1958).

44. Koon, D. W. & Knickerbocker, C. J. What do you measure when you measure resistivity? *Rev. Sci. Instrum.* (1992).

45. Koon, D. W. Effect of contact size and placement, and of resistive inhomogeneities on van der Pauw measurements. *Rev. Sci. Instrum.* **60**, 271–274 (1989).

46. Koon, D. W., Bahl, A. A. & Duncan, E. O. Measurement of contact placement errors in the van der Pauw technique. *Rev. Sci. Instrum.* **60**, 275–276 (1989).

47. Marinov, O., Deen, M. J., Zschieschang, U. & Klauk, H. Organic thin-film transistors: Part I-compact DC modeling. *IEEE Trans. Electron Devices* (2009).

48. Necliudov, P. V., Shur, M. S., Gundlach, D. J. & Jackson, T. N. Modeling of organic thin film transistors of different designs. *J. Appl. Phys.* (2000).

49. Marinkovic, M., Belaineh, D., Wagner, V. & Knipp, D. On the origin of contact resistances of organic thin film transistors. *Adv. Mater.* (2012).

50. Charlot, B. *et al.* Micropatterning PEDOT:PSS layers. *Microsyst. Technol.* **19**, 895–903 (2013).

51. Giovannitti, A. *et al.* Energetic Control of Redox-Active Polymers toward Safe Organic Bioelectronic Materials. *Adv. Mater.* **32**, 1–9 (2020).

52. Proctor, C. M., Rivnay, J. & Malliaras, G. G. Understanding volumetric capacitance in conducting polymers. *J. Polym. Sci. Part B Polym. Phys.* **54**, 1433–1436 (2016).

53. Bernards, D. A. & Malliaras, G. G. Steady-state and transient behavior of organic electrochemical transistors. *Adv. Funct. Mater.* (2007).

54. Marcus, R. A. Chemical and Electrochemical Electron-Transfer Theory. *Annu. Rev. Phys. Chem.* (1964).

55. Liu, C. *et al.* Device Physics of Contact Issues for the Overestimation and Underestimation of Carrier Mobility in Field-Effect Transistors. *Phys. Rev. Appl.* (2017).

56. Pretl, S. *et al.* Electrical characterization of PEDOT:PSS. in *Electronics System Integration Technology Conference, ESTC 2010 - Proceedings* (2010).

57. Kaphle, V., Liu, S., Al-Shadeedi, A., Keum, C. M. & Lüssem, B. Contact Resistance Effects in Highly Doped Organic Electrochemical Transistors. *Adv. Mater.* (2016).

58. Kaphle, V., Paudel, P. R., Dahal, D., Radha Krishnan, R. K. & Lüssem, B. Finding the equilibrium of organic electrochemical transistors. *Nat. Commun.* (2020).

59. Stavrinidou, E., Sessolo, M., Winther-Jensen, B., Sanaur, S. & Malliaras, G. G. A physical interpretation of impedance at conducting polymer/electrolyte junctions. *AIP Adv.*

60. Tybrandt, K., Zozoulenko, I. V. & Berggren, M. Chemical potential-electric double layer coupling in conjugated polymer-polyelectrolyte blends. *Sci. Adv.* **3**, 1–8 (2017).

61. Gelderman, K., Lee, L. & Donne, S. W. Flat-band potential of a semiconductor: Using the Mott-Schottky equation. *J. Chem. Educ.* (2007).

62. Oelerich, J. O., Huemmer, D. & Baranovskii, S. D. How to find out the density of states in disordered organic semiconductors. *Phys. Rev. Lett.* (2012).

63. Nenashev, A. V., Oelerich, J. O. & Baranovskii, S. D. Theoretical tools for the description of charge transport in disordered organic semiconductors. *J. Phys. Condens. Matter* (2015).

64. Shi, X. H., Sun, J. X., Xiong, C. H. & Sun, L. Exponential-type density of states with clearly cutting tail for organic semiconductors. *Org. Electron.* (2016).

Acknowledgments

This thesis concludes an important part of my University career, certainly tiring, but also full of great satisfactions. I would therefore like to thank all those who have been close to me during this long journey.
The first thanks go to my family, my parents Cristina and Andrea, my grandparents Imelde, Carlo, Chiara and Pietro, my uncles, my cousin (brother) Federico, my girlfriend Elisa. This work is not only *dedicated* to them, but it is their *merit*. Not a single day has passed in which I have not felt supported, encouraged and loved. They gave me everything, and made me who I am. They have endured my nervousness, my too many silences, the sometimes absent gaze, the stress. I hope it was worth it.
The second thanks goes to all my friends, with whom I have shared happy moments, holidays, adventures, lunches, dinners. In this case I prefer not to mention names, just for fear of forgetting someone. Thanks to them all the difficult moments seemed easier to me, thanks to them these years have simply been better.
Finally, I thank my supervisor, Prof. Tobias Cramer, who assisted me throughout the course of the thesis despite the difficulties related to the complex situation we are living, and my co-supervisor, Dr. Francesco Decataldo, for his great availability, competence and for the passion he transmitted to me.

Ringraziamenti

Con questa tesi si conclude una parte importante del mio percorso Universitario, sicuramente faticoso, ma anche ricco di grandi soddisfazioni. Vorrei quindi ringraziare tutti coloro che mi sono stati vicini durante questo lungo viaggio.
Il primo ringraziamento va alla mia famiglia, ai miei genitori Cristina ed Andrea, ai miei nonni Imelde, Carlo, Chiara e Pietro, ai miei zii, a mio cugino (fratello) Federico, alla mia ragazza Elisa. Questo lavoro non è solo *dedicato* a loro, ma è *merito* loro. Non è passato un solo giorno nel quale non mi sia sentito sostenuto, incoraggiato ed amato. Mi hanno dato tutto, e reso quello che sono. Hanno sopportato il mio nervosismo, i miei silenzi di troppo, lo sguardo a volte assente, lo stress. Spero ne sia valsa la pena.
Il secondo ringraziamento va a tutti i miei amici, con i quali ho condiviso momenti lieti, vacanze, avventure, pranzi, cene. In questo caso preferisco non fare nomi, soltanto per paura di dimenticare qualcuno. Grazie a loro i momenti difficili mi sono sembrati più facili, grazie a loro questi anni sono stati semplicemente migliori.
Ringrazio infine il mio relatore, il Prof. Tobias Cramer, che mi ha accompagnato attentamente per tutto il percorso di tesi nonostante le difficoltà legate alla complessa situazione che stiamo vivendo, ed il mio correlatore, il Dott. Francesco Decataldo, per la grande disponibilità, competenza e per la passione che mi ha trasmesso.